PDMS-OXIDE PARTICLES BASED COMPOSITE STRUCTURES FOR CONTINUOUS PHOTOCATALYTIC REACTOR AND MASS TRANSFER APPLICATIONS

Thesis submitted in partial fulfilment

for the Award of Degree

Doctor of Philosophy

by

ANIL VERMA

RAJIV GANDHI INSTITUTE OF PETROLEUM TECHNOLOGY

JAIS-229304

PMS19-001 *2026*

CERTIFICATE

It is certified that the work contained in the thesis titled ***"PDMS-OXIDE PARTICLES BASED COMPOSITE STRUCTURES FOR CONTINUOUS PHOTOCATALYTIC REACTOR AND MASS TRANSFER APPLICATIONS"*** by **"*ANIL VERMA"*** has been carried out under my supervision and that this work has not been submitted elsewhere for a degree.

It is further certified that the student has fulfilled all the requirements of Comprehensive, Candidacy, and SOTA.

Prof. Amit Ranjan

(Supervisor)

DECLARATION BY THE CANDIDATE

I, ***ANIL VERMA***, certify that the work embodied in this thesis is my own bona fide work and carried out by me under the supervision of ***Prof. AMIT RANJAN*** from ***AUGUST 2019*** to ***JUNE 2026,*** at the Rajiv Gandhi Institute of Petroleum Technology, Jais. The matter embodied in this thesis has not been submitted for the award of any other degree. I declare that I have faithfully acknowledged and given credits to the research workers wherever their works have been cited in my work in this thesis. I further declare that I have not wilfully copied any other's work, paragraphs, text, data, results, etc., reported in journals, books, magazines, reports, dissertations, theses, etc., or available on websites and have not included them in this thesis and have not cited as my own work.

Date:

Place: RGIPT, Jais, Amethi **(*ANIL VERMA*)**

CERTIFICATE BY THE SUPERVISOR

It is certified that the above statement made by the student is correct to the best of my knowledge.

Prof. Amit Ranjan

(Supervisor) **Signature & Seal of Head of Department**

CERTIFICATE

CERTIFIED that the work contained in the thesis titled **"PDMS-oxide particles based composite structures for continuous photocatalytic reactor and mass transfer applications"** by **Mr. Anil Verma** has been carried out under my supervision. It is also certified that he fulfilled the mandatory requirement of TWO quality publications arose out of his thesis work.

It is further certified that the two publications (copies enclosed) of the aforesaid **Mr. Anil Verma** have been published in the Journals indexed by –

(a) SCI
(b) SCI Extended
(c) SCOPUS

Prof. Amit Ranjan

(Supervisor) **(Convener, DPGC)**

SEAL

COPYRIGHT TRANSFER CERTIFICATE

Title of the Thesis: PDMS-oxide particles based composite structures for continuous photocatalytic reactor and mass transfer applications

Name of the Student: Anil Verma

Copyright Transfer

The undersigned hereby assigns to the Rajiv Gandhi Institute of Petroleum Technology Jais all rights under copyright that may exist in and for the above thesis submitted for the award of the "*DOCTOR OF PHILOSOPHY*".

Date:

Place: RGIPT, Jais, Amethi (***ANIL VERMA***)

Note: However, the author may reproduce or authorize others to reproduce material extracted verbatim from the thesis or derivative of the thesis for the author's personal use provided that the source and the Institute's copyright notice are indicated.

Dedicated to my guide and my family…..

ACKNOWLEDGMENT

"It is better to fail in originality than to succeed in imitation."

—Herman Melville

This thesis is the culmination of a long and enriching academic journey, and I take this opportunity to express my sincere gratitude to all those who contributed to its completion.

At the outset, I wish to express my profound gratitude to my research supervisor, **Prof. Amit Ranjan,** Department of Mechanical Engineering, RGIPT, for his continuous support, guidance, and mentorship throughout the course of my doctoral work. His professional insight, encouragement, and constructive criticism played a pivotal role in shaping this research and my academic development.

I am especially grateful to the members of my Research Progress Evaluation Committee (RPEC), **Prof. M. S. Balathanigaimani,** and **Dr. Arshad Aijaz** for their insightful comments, suggestions, and continuous evaluation that helped refine my research objectives and boosted my confidence over the years.

I would like to extend my heartfelt thanks to **Dr. V. S. Sistla**, Head, Department of Chemical and Biochemical Engineering, RGIPT, for his support and encouragement at various stages of my research. I also acknowledge the encouragement and assistance provided by the faculty and staff members of the department.

I also acknowledge the support of **the Institute's Central Instrumentation Facility (CIF)** for assistance in the characterization of materials and analysis of experimental samples, which was critical to the successful execution of this study.

I am thankful to my former lab colleagues in the Materials' Group including **Dr. Shama Perween**, **Dr. Somendra Singh**, **Dr. Yogendra Yadawa**, and currently, **Mr. Sujeet Kumar Pandey** for their assistance, valuable discussions, and camaraderie throughout this journey. Working alongside them has been both productive and enjoyable. I also wish to thank former lab member **Dr. Harsh Sharma** and present lab members, **Mr. Niyamat Ullah Khan**, **Mr. Aash Mohammad** and **Mr. Nirmal Ram**, whose collaborative spirit and friendly nature created a supportive and engaging lab environment.

My deepest appreciation also goes to fellow researchers and friends across departments whose direct or indirect involvement provided much-needed motivation, technical inputs, and emotional strength during challenging times.

I am eternally indebted to my family, especially my parents and close relatives whose unconditional love, sacrifices, and faith in my abilities have been the foundation of my perseverance. Their constant encouragement and emotional support were invaluable in completing this academic endeavor.

Above all, I thank the **Almighty** for blessing me with strength, patience, and resilience throughout this journey.

(ANIL VERMA)

PREFACE

This thesis presents an in-depth exploration into the versatile applications of polydimethylsiloxane (PDMS), a silicon-based elastomer known for its unique combination of optical transparency, chemical inertness, viscoelasticity, and hydrophobicity. Utilizing these properties, the research develops and evaluates various PDMS-based soft structures, such as, membranes and coiled flow inverters (CFIs), across a diverse range of scientific and engineering applications.

The work encompasses both batch and continuous processes, including pervaporation-based separation, thermal energy storage (TES), and visible-light-induced photocatalysis. Special emphasis is placed on how PDMS, in both its pure and particle-impregnated forms, enables or enhances functionality in these domains. The use of Sylgard 184, a commercial PDMS formulation, is central to this investigation, as its transformation from a liquid precursor into an elastomeric solid provides the structural adaptability required for such multifunctional applications.

The thesis is organized into seven chapters, each building upon a core aspect of the research. The first chapter sets the stage by introducing the materials under study—including PDMS, silicon oxycarbide (SiOC) and zinc titanate ($ZnTiO_3$) and outlining the specific objectives and scope. It provides the scientific background and relevance of the core topics, from photocatalysis and TES to membrane-based separations.

The second chapter details the experimental methodology, including materials used, synthesis procedures, and characterization techniques. This foundational chapter ensures reproducibility and establishes the basis for subsequent analyses.

Chapters three through six present the experimental results and application-specific studies. Chapter three introduces a photocatalytic reactor built using a PDMS-lined CFI inside silicon tube with plasma-treated $ZnTiO_3$ particles. Chapter four investigates pervaporation of ethanol-water mixtures using SiOC-impregnated PDMS membranes, while chapter five discusses continuous liquid–liquid extraction of acetic acid using a PDMS-based CFI. Chapter six shifts the focus to thermal energy storage, where PDMS membranes are embedded with stearic acid as a phase change material.

The final chapter, chapter seven, consolidates the findings, draws conclusions, and outlines unresolved issues and future directions. It reflects on how PDMS-based soft structures can continue to advance innovative solutions across materials science and process engineering.

This work is the culmination of interdisciplinary efforts and is intended to contribute to the growing body of knowledge on soft materials, membrane technology, and functional composites, highlighting PDMS as a highly adaptable platform for future scientific and industrial innovation.

Table of Contents

List of Figures

List of Tables

Abbreviations/Acronyms

AA	:	Acetic acid
ALD	:	Atomic layer deposition
BET	:	Brunauer–emmett–teller
CFI	:	Coiled flow inverter
CVD	:	Chemical vapor deposition
DIPA	:	Diisopropylamine
DLS	:	Dynamic light scattering
DRS	:	Diffuse reflectance spectroscopy
DSC	:	Differential scanning calorimetry
EDX or EDS	:	Energy dispersive x-ray Spectroscopy
EMI	:	Electromagnetic interference
SEM	:	Scanning electron microscopy
FT-IR	:	Fourier transform infrared
GC	:	Gas chromatography
LLE	:	Liquid-liquid extraction
MB	:	Methylene blue
MEMS	:	Microelectromechanical systems
MOF	:	Metal-organic framework
PCM	:	Phase change material
PDC	:	Polymer-derived ceramics
PDMS	:	Polydimethylsiloxane
PSC	:	Perovskite solar cell
PVA	:	Polyvinyl alcohol

SA	:	Stearic acid
SEM	:	Scanning electron microscopy
SHS	:	Sensible heat storage
SiOC	:	Silicon oxycarbide
TEM	:	Transmission electron microscopy
TES	:	Thermal energy storage
THF	:	Tetrahydrofuran
UV	:	Ultraviolet
UV-Vis	:	Ultraviolet-visible
VOC	:	Volatile organic compound
XRD	:	X-ray diffraction
ZTO	:	Zinc titanate

Thesis Novelty

The thesis establishes that polydimethylsiloxane (PDMS) can be transformed from a passive elastomer into a multifunctional soft composite platform for photocatalysis, mass transfer and energy storage applications. The novelty of the work is reflected in the following key contributions:

- Development of a first-of-its-kind transparent PDMS-lined coiled flow inverter reactor impregnated with plasma-treated $ZnTiO_3$ particles for continuous visible-light photocatalytic degradation of methylene blue, achieving more than two-fold higher degradation kinetics than a straight tube reactor.

- Introduction of a swelling–deswelling-based particle impregnation method for incorporating functional particles into the subsurface region of PDMS structures while retaining their exposure to the active interface.

- Synthesis of high-surface-area silicon oxycarbide (SiOC) particles from PDMS sponge through a relatively low-temperature polymer-derived ceramic route, followed by their asymmetric infusion into PDMS membranes for enhanced ethanol–water pervaporation through a mixed solid–liquid diffusion mechanism.

- Fabrication of a millifluidic PDMS-CFI using a removable PVA filament for continuous liquid–liquid extraction of acetic acid, achieving an overall volumetric mass transfer coefficient of 0.007145 s^{-1}

- Development of stearic acid embedded PDMS membranes were prepared for thermal energy storage, with optimized latent heat utilization at ~ 19.5 wt% stearic acid.

Thesis Abstract

This thesis presents the design and development of PDMS–oxide particle based soft composite structures for continuous photocatalysis, pervaporation, liquid–liquid extraction, and thermal energy storage. Using Sylgard 184 PDMS as the primary soft matrix, functional fillers including plasma-treated zinc titanate ($ZnTiO_3$), silicone oxycarbide (SiOC), and phase change material-stearic acid (SA) were incorporated to overcome the limitations of pristine PDMS and develop multifunctional systems for photocatalytic, separation, mass transfer, and thermal applications.

In the first segment, a transparent PDMS-lined CFI reactor was fabricated for continuous visible-light photocatalytic degradation of methylene blue (MB) dye. The reactor was prepared by coating the inner surface of a silicone tube with PDMS, swelling the cured lining, and immobilizing plasma-treated rhombohedral $ZnTiO_3$ particles, synthesized through the sol-gel method, within the PDMS layer through a swelling–deswelling approach. Plasma treatment improved the aqueous dispersibility and suspension stability of $ZnTiO_3$ particles, while band-gap analysis showed a reduced optical band gap of 2.77 eV, supporting visible-light photocatalytic activity. The $ZnTiO_3$ particles were immobilized inside the PDMS-lined CFI with an estimated particle area fraction of 0.105, corresponding to an exposed photocatalyst area of approximately 10.34 cm^2. Photocatalytic experiments were conducted using 10 ppm MB solution at six flow rates of 0.72, 0.96, 1.20, 1.44, 1.68, and 1.92 mL/min under a 25 W white LED source. The illuminated $ZnTiO_3$-lined PDMS-CFI exhibited a pseudo-first-order rate constant of $24.66 \pm 6.28 \times 10^{-3}$ min^{-1}, compared with $10.60 \pm 3.28 \times 10^{-3}$ min^{-1} for the illuminated straight tube and $3.69 \pm 2.00 \times 10^{-3}$ min^{-1} for dark CFI operation. The more than two-fold enhancement over the straight tube and nearly five-fold improvement over dark operation confirmed the combined role of photocatalyst immobilization, visible-light activation, optical accessibility, and CFI-induced secondary flow in improving continuous photocatalytic degradation.

Another part of the work involved the fabrication and comparison of neat and SiOC-impregnated PDMS membranes for pervaporation-based ethanol–water separation. SiOC particles were synthesized from PDMS sponge through low-temperature thermal degradation at 550 °C, producing porous amorphous Si–O–C particles with high specific surface area of approximately 192 m^2 g^{-1}. These particles were selectively infused into one surface of swollen PDMS membranes using a diisopropylamine-assisted suspension

method, producing asymmetric composite membranes with localized particle penetration up to approximately 100 μm. SEM–EDX, porometry, and contact-angle analyses confirmed localized SiOC incorporation, broadened pore-size distribution, and increased surface hydrophilicity. Pervaporation experiments were performed for a 1:1 ethanol–water mixture at 298 K under reduced permeate-side pressure. Although the absolute flux remained comparatively low, the SiOC-impregnated membrane showed approximately 150% enhancement in ethanol–water separation factor compared with the native PDMS membrane. This improvement was attributed to localized hydrated SiOC domains that promoted ethanol transport through a mixed solid–liquid diffusion pathway, unlike the mainly solid-state diffusion mechanism dominant in neat PDMS membranes.

In continuation, a millifluidic PDMS-based CFI was developed for continuous liquid–liquid extraction of acetic acid from an acetic acid–toluene and water system. The CFI was fabricated by casting PDMS around a removable helical polyvinyl alcohol filament, followed by template dissolution to form an internally coiled channel. The cured PDMS structure was sectioned and reconnected to generate four sequential 90° inversions, enabling periodic phase reorientation, interfacial renewal, and enhanced liquid–liquid contact. The system was used to extract acetic acid from an organic mixture containing 10% acetic acid in toluene using water as the extracting phase. Extraction studies were performed by varying aqueous and organic phase flow rates, while outlet concentrations were determined through refractive-index calibration. The results showed that aqueous phase flow rate had a stronger influence on mass transfer enhancement than organic phase flow rate. At constant aqueous flow, increasing the organic phase flow rate improved extraction efficiency by about two-fold, whereas increasing aqueous flow produced nearly three-fold improvement. The maximum overall volumetric mass transfer coefficient obtained was 0.007145 s^{-1} under the highest water-flow condition, confirming the effectiveness of PDMS-CFI geometry for compact continuous extraction and mass transfer intensification.

Lastly, stearic acid embedded PDMS membranes were fabricated and thermally characterized for thermal energy storage applications. Composite membranes were prepared using the doctor-blading method by varying SA loading from 5.7 to 23.3 wt% and tetrahydrofuran solvent volume from 2 to 4 mL. FTIR analysis confirmed successful physical incorporation of SA into the PDMS matrix with negligible residual solvent and without significant chemical interaction. DSC analysis showed stable melting temperatures

around 56 °C and crystallization temperatures around 52–53 °C. Latent heat increased from 2.7 to 34.3 J g^{-1} with increasing SA loading; however, latent heat utilization efficiency increased from approximately 24% to a maximum of nearly 80% at about 19.5 wt% SA and then declined slightly at higher loading due to confinement-limited crystallization. Cooling-curve analysis showed that the composite membranes reduced the cooling rate from approximately 2.0 °C/min for pure SA to approximately 0.29 °C/min and increased the thermal time constant from around 1000 s to nearly 6300 s, confirming improved thermal inertia and controlled heat-release behavior due to the insulating PDMS matrix.

Overall, the thesis demonstrates that PDMS can be transformed from a passive elastomer into an active multifunctional soft composite platform by incorporating suitable functional fillers and controlling their spatial distribution. The objective outcomes confirm measurable improvements across all experimental domains: enhanced photocatalytic kinetics in $ZnTiO_3$-lined CFIs, approximately 150% improvement in ethanol–water separation factor using SiOC-impregnated membranes, a maximum volumetric mass transfer coefficient of 0.007145 s^{-1} in acetic acid extraction, and nearly 80% latent heat utilization efficiency at optimized SA loading. The subjective conclusions indicate that PDMS-based soft structures are suitable for integrating photocatalysis, selective transport, interfacial mass transfer, and thermal energy storage within a unified flexible framework. Future work may focus on optimization of photocatalytic operating parameters, long-term catalyst stability, real wastewater validation, improvement of pervaporation flux, membrane durability, particle leaching assessment, scale-up of PDMS-CFI systems, long-term PCM cycling, leakage resistance, and incorporation of thermally conductive fillers for improved thermal response.

Chapter 1: Motivation and Introduction

1.1 Motivation

The evolution of functional materials has significantly advanced material science, environmental remediation, and sustainable technologies. Among these, soft polymeric materials are especially attractive because of their tunable properties, flexibility, chemical stability, and compatibility with microfabrication techniques. Polydimethylsiloxane (PDMS), in particular, has emerged as a material of choice owing to its optical transparency, chemical inertness, and versatility in constructing structures that support mass transfer operations and photoactive reactions under ambient or visible light conditions.

Despite its wide use in membranes, microfluidics, and soft reactor systems, pristine PDMS suffers from limitations, such as, hydrophobicity, low surface activity, and insufficient catalytic functionality. These drawbacks restrict its broader applicability in integrated photocatalytic and pervaporation systems. Incorporating functional fillers, such as, oxide particles, e.g., $ZnTiO_3$, polymer-derived ceramics, like, silicon oxycarbide, and phase change materials, such as, stearic acid offers a pathway to engineer hybrid PDMS-based composites with synergistic properties. Such composites can enhance catalytic efficiency, light harvesting, and stability while improving selectivity and mass transfer characteristics.

This thesis is motivated by the need to bridge the gap between soft material design and process intensification. By fabricating PDMS–oxide particle composites for continuous photocatalytic reactors and mass transfer applications, the study aims to integrate the mechanical advantages of PDMS with the catalytic and functional attributes of inorganic and hybrid fillers. These developments hold strong potential for advancing next-generation multifunctional systems in materials science and engineering, particularly for environmental and energy-related applications.

1.2 Overview of PDMS

1.2.1 Definition, synthesis, and molecular characteristics

PDMS, also known as dimethicone, is a synthetic, silicon-based organic polymer belonging to the broader class of silicones. It is composed of repeating $–[Si(CH_3)_2–O]–$ units, where

each silicon atom is bonded to two methyl groups and connected through oxygen atoms, forming a flexible siloxane backbone. This distinctive backbone provides the polymer with a high degree of conformational mobility and forms the basis for many of its unique physicochemical properties.

The empirical formula of PDMS is $(C_2H_6OSi)_n$ where "*n*" denotes the degree of polymerization. Depending on the value of "n", PDMS can exist as low-viscosity fluids, gels, or rubber-like solids[1]. A schematic representation of the basic chemical structure of PDMS is shown below in Figure 1.1:

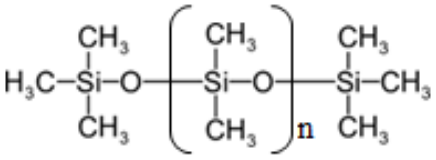

Figure 1.1: Chemical Structure of Polydimethylsiloxane (PDMS)[–Si(CH₃)₂–O–]ₙ

where, Si = silicon atom, O = oxygen atom, CH_3 = methyl group, n = number of repeating units). PDMS is typically synthesized through a two-step process involving the hydrolysis and condensation of dimethyldichlorosilane ($Si(CH_3)_2Cl_2$). In the presence of water, hydrolysis yields silanol groups (–Si–OH), which subsequently undergo condensation to form siloxane (–Si–O–Si–) bonds, resulting in linear or slightly branched polymer chains. The final molecular weight is governed by the extent of polymerization, which can range from several thousand to several million Daltons[2].

The siloxane backbone of PDMS, comprising alternating Si–O linkages, has distinct molecular geometry compared to traditional organic polymers. The Si–O bond is both longer (~1.64 Å) and more flexible than C–C or C–O bonds, and the bond angle (~143°) imparts significant rotational freedom to the polymer chain. This architecture enables high flexibility and thermal stability, making PDMS a versatile material for both research and industrial applications. Attached to each silicon atom are two methyl groups ($–CH_3$), which contribute to the polymer's hydrophobicity, reduce intermolecular interactions, and result in a very low glass transition temperature ($T_g \approx –125°C$). These characteristics allow PDMS to remain soft and elastic over a wide temperature range[3,4].

PDMS chains can be terminated with functional end groups, such as, hydroxyl, vinyl, or hydrogen. These groups enable chemical modifications and facilitate cross-linking, which is essential for producing solid elastomeric materials. At room temperature, PDMS

typically exists as a transparent, viscous liquid, owing to the molecular flexibility of its siloxane backbone. This fluidic nature is essential to its processability, particularly in microscale and soft material fabrication.

To transform PDMS into a usable structural material, it is mixed with a cross-linking agent, usually as part of a commercial two-part kit, such as, Sylgard 184 (Dow Corning). This formulation consists of a vinyl-terminated PDMS base polymer and a curing agent containing a silicon-hydride cross-linker and a platinum-based catalyst. These components are typically mixed in a 10:1 weight ratio, initiating a hydrosilylation reaction. During this process, silicon-hydride (Si–H) groups react with vinyl groups (–CH=CH_2), forming a three-dimensional cross-linked network[5–7], as shown below in Figure 1.2.

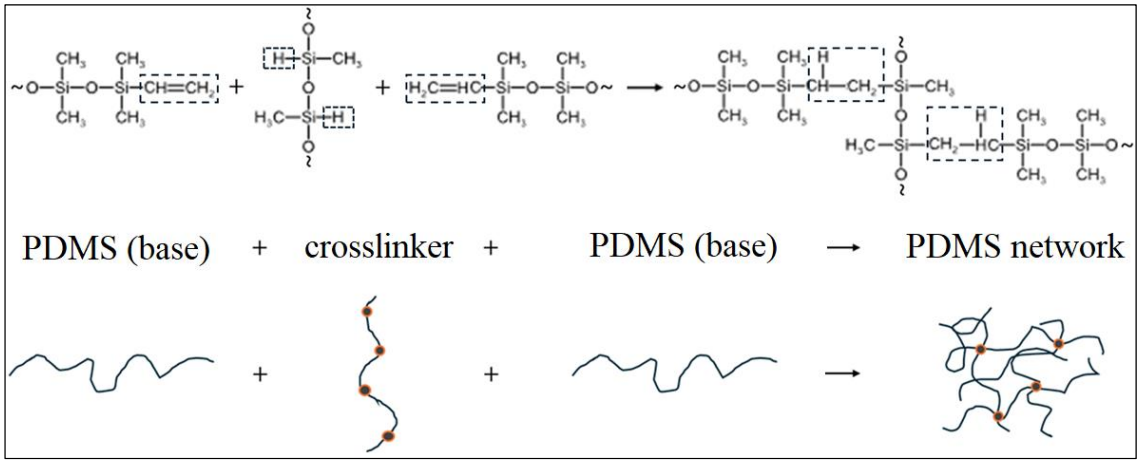

Figure 1.2: Crosslinking reaction between PDMS and cross-linker (curing agent).

The mixture can be cured either at room temperature or with mild heating, resulting in a flexible, rubber-like elastomer. The curing process can be initiated thermally (heating up to 150 °C for 10 minutes) or allowed to proceed slowly at room temperature over a longer duration of 2 days. Specifically, the curing time and the temperature depends on the crosslinking ratios. The higher crosslinking ratios cure faster but are mechanically brittle[8,9]. Upon curing, the PDMS replica can be peeled away, reproducing the original pattern with high fidelity and dimensional accuracy. The cured PDMS retains excellent mechanical compliance, making it ideal for applications requiring soft, stretchable, or deformable materials[10].

1.2.2 Background, significant properties, applications and limitations

PDMS holds significant historical relevance as one of the most influential and widely utilized silicon-based polymers in modern science and industry. Its origins can be traced

back to the early 20th century when chemists first began exploring the unique chemistry of organosilicon compounds. Pioneering work by Friedrich Kipping in the early 1900s laid the foundational understanding of silicon-based polymers, although practical applications were not immediately realized. The turning point came during the 1940s, in the midst of World War II, when industrial interest in synthetic materials that could withstand extreme conditions led to the development and commercialization of silicones, including PDMS. Companies, like Dow Corning played a pivotal role in advancing silicone technology, producing PDMS for use in electrical insulation, lubricants, and sealants due to its exceptional thermal stability, flexibility, and chemical inertness[11].

The widespread adoption of PDMS accelerated in the 1990s with the advent of soft lithography and microfluidics, where PDMS's optical transparency, moldability, and elastomeric nature made it indispensable for lab-on-a-chip systems and biomedical diagnostics[12,13]. These properties have since enabled applications in soft robotics, wearable electronics, and environmental sensors[14–16].

PDMS is inherently hydrophobic due to the presence of nonpolar methyl ($–CH_3$) side groups on its siloxane backbone. This results in a low surface energy (~20–25 mN/m) and a water contact angle ranging from 100° to 120°, making PDMS highly water-repellent. These features are advantageous in microfluidics, where anti-fouling and non-wetting behavior support controlled fluid handling. However, this same hydrophobicity poses challenges in biological systems, where it can hinder cell adhesion, protein adsorption, and aqueous wetting. In microchannels, air bubble entrapment and reduced surface reactivity are also common concerns[17–19].

To mitigate these limitations, surface modification techniques have been extensively developed. Oxygen plasma treatment temporarily introduces hydrophilic –OH groups, drastically reducing the water contact angle and improving bonding, though hydrophobic recovery remains a drawback. More permanent approaches include UV-induced grafting of hydrophilic polymers and silanization using reactive silane agents to enable functionalization for biosensing or protein immobilization[20,21].

PDMS also demonstrates high permeability to organic vapors and gases due to its flexible siloxane chains and large free volume. This enables selective diffusion based on molecular size, solubility, and polymer affinity. PDMS readily absorbs nonpolar solvents and volatile organic compounds (VOCs), like, alcohols and hydrocarbons, while water and other polar

species are less permeable. These properties are useful in pervaporation membranes, chemical sensors, and controlled release systems. However, excessive swelling from solvents, such as, toluene, hexane, or chloroform can cause dimensional instability and mechanical degradation[17,22].

Mechanically, PDMS is a soft elastomer with tunable properties. Base to curing agent ratio, curing time, temperature adjusts its stiffness, yielding a Young's modulus from 0.2 to 3 MPa, tensile strength of 3–8 MPa, and elongation at break of 100–200%. Thermally, PDMS operates reliably from –50 °C to 200 °C and exhibits high oxidative and UV stability. Optically, it is highly transparent (transmittance >90% in the 400–1100 nm range), with a refractive index (~1.41) close to biological tissues, making it suitable for imaging and optical sensors[2,8,9,23,24].

Despite its strengths, PDMS has notable limitations. Its incompatibility with strong acids, bases, and aggressive solvents can lead to Si–O–Si backbone degradation. Furthermore, PDMS tends to absorb small hydrophobic molecules, which can compromise assay sensitivity, cause leaching, and introduce cytotoxicity[17,25,26]. This is particularly problematic in drug delivery and biosensing applications where precision and reproducibility are critical.

To address these issues, surface coatings such as poly(ethylene glycol), parylene, or silica are applied using grafting, chemical vapor deposition (CVD), or atomic layer deposition (ALD). These enhance chemical resistance, reduce absorption, and extend surface hydrophilicity. Additionally, PDMS composites incorporating fillers, like, silica nanoparticles, graphene oxide, or nanoclays improve mechanical strength, solvent resistance, and barrier properties without severely affecting elasticity[2,27]. These innovations are crucial for extending the material's functionality in demanding environments.

1.3 Overview of polymer-derived ceramics

1.3.1 Introduction, synthesis, and classification

Polymer-derived ceramics (PDCs) represent a novel and versatile class of non-oxide ceramics that are synthesized via the cross linking and thermal decomposition (pyrolysis) of preceramic polymers—organosilicon compounds, such as, polycarbosiloxanes,

polysilazanes, or polysilsequioxanes under controlled conditions, typically in an inert or reactive atmosphere. This method, first introduced over five decades ago, has since gained significant attention due to its ability to create ceramics with tailored properties and complex geometries. Unlike conventional ceramics formed by powder sintering at high temperatures, PDCs originate from molecularly designed polymer precursors that provide precise control over the final ceramic composition and structure[28].

The synthesis of PDCs generally involves four major stages:

- **Shaping**: Preceramic polymers can be shaped into complex forms using techniques, such as, molding, extrusion, dip-coating, or 3D printing.
- **Cross-linking**: Thermal or chemical cross-linking creates a networked structure within the polymer, enhancing stability during pyrolysis.
- **Pyrolysis**: The cross-linked polymer is subjected to temperatures ranging from 800°C to 1500°C. This results in decomposition of the organic groups and transformation into an amorphous ceramic phase without melting.
- **Crystallization**: At higher temperatures, partial crystallization can occur, forming nanocrystalline domains embedded within the amorphous matrix.

PDCs are typically classified based on the elemental composition of the preceramic polymer and the resulting ceramic material:

- **Si–C ceramics**: Derived from polysilanes and polycarbosilanes, resulting in silicon carbide-based materials.
- **Si–N ceramics**: Produced from polysilazanes, leading to silicon nitride-type ceramics.
- **Si–C–N ceramics**: Created by modifying organosilicon polymers to include nitrogen, combining the properties of both SiC and Si_3N_4.
- **Si–O ceramics**: Formed from silicone-based precursors, such as, PDMS.
- **Multicomponent and metal-modified ceramics**: Incorporating additional elements, like, boron, aluminium, titanium, hafnium, or zirconium into the network (e.g., Si–B–C–N, Si–Ti–C–N), enabling advanced thermal, electrical, and chemical functionalities.

The flexibility in polymer design and processing conditions allows for significant tunability of properties, making PDCs suitable for a wide variety of application-specific material designs[29].

1.3.2 Properties and applications

Polymer-derived ceramics are distinguished by a unique combination of structural and functional properties. Structurally, they exhibit high thermal stability, withstanding temperatures up to 2000 °C while maintaining their amorphous nature and resisting creep, crystallization, and oxidation. Chemically, they are highly inert, making them suitable for corrosive environments. Functionally, PDCs can exhibit semiconducting behaviour, photoluminescence, piezoresistivity, and even electromagnetic shielding, largely attributed to their nanostructured domains and bond arrangements.

Advances in materials science have revealed that the unique nanoscale features of PDCs—characterized by nanodomains (1-5 nm) comprising Si–C, Si–O, and Si–N bonds—are crucial to their multifunctional behavior. These nanostructures often resemble disordered networks of graphene-like sheets, which significantly enhance their mechanical, thermal, and electrical performance. The versatility of the polymer route allows easy shaping into complex geometries before pyrolysis, enabling the cost effective net-shape processing and integration into various components, including high-strength ceramic fibers, coatings, porous bodies, selective membranes, and microelectromechanical systems (MEMS). Furthermore, by manipulating the polymer chemistry and pyrolysis conditions, hybrid materials with tunable organic-inorganic character can be fabricated, offering lightweight structures with superior thermal and chemical resistance for use in intermediate-temperature applications (300–600 °C)[30].

Applications are broad and span multiple high-performance domains, including:

- **Aerospace components**: PDCs are used in turbine engine parts and other high-temperature components due to their thermal stability and strength.
- **Electromagnetic interference (EMI) shielding**: SiOC composites have been developed for effective EMI shielding, combining high permittivity with structural integrity.

- **Thermoelectric devices**: PDCs are being explored for sustainable thermoelectric applications due to their low thermal conductivity and tunable electrical properties.
- **3D Printed structures**: The ability to 3D print PDCs allows for the creation of complex, high-performance components that are difficult to achieve with traditional ceramic processing methods.
- **Biomedical engineering**: Biocompatible PDCs are applied in tissue regeneration, implant design, drug delivery, and wound dressing.

The interdisciplinary nature of PDC research continues to drive innovations in material design, positioning PDCs as integral components of next-generation technologies.

1.3.3 Polymer derived SiOC

Silicon oxycarbide (SiOC) is a ternary, polymer-derived amorphous ceramic in which silicon atoms form mixed SiO_xC_{4-x} tetrahedral units, bonded to both oxygen and carbon within a continuous network which given in Figure 1.3[31]. During pyrolysis, around 1100 °C the material retains its largely amorphous structure, yet high-resolution analysis reveals nanoscale heterogeneity due to non-stoichiometry and embedded free-carbon domains. These nanodomains include amorphous SiO_2 clusters, turbostratic or graphitic free carbon, amorphous or crystalline SiC, and interfacial regions rich in mixed-bond SiO_4C_{4-x} units. Carbon content can be tuned by selecting different polymer precursors—for instance, varying triethoxysilane versus methyldiethoxysilane modulates the amount of C incorporated. With increasing carbon loading, graphitic nanodomains percolate through a C-rich SiO_4C_{4-x} matrix, while oxygen-rich units form the surrounding scaffold. At low carbon levels (≤ 8 wt %), the material approaches near-stoichiometric SiOC, enabling clearer observation of microstructural evolution. Upon annealing to ~1300 °C, phase separation begins as Si–O and Si–C bonds redistribute. Further heating to 1400–1600 °C triggers carbothermal reduction: free carbon reacts with SiO_2 to form nanoscale β-SiC, diminishing the carbon content[29,31].

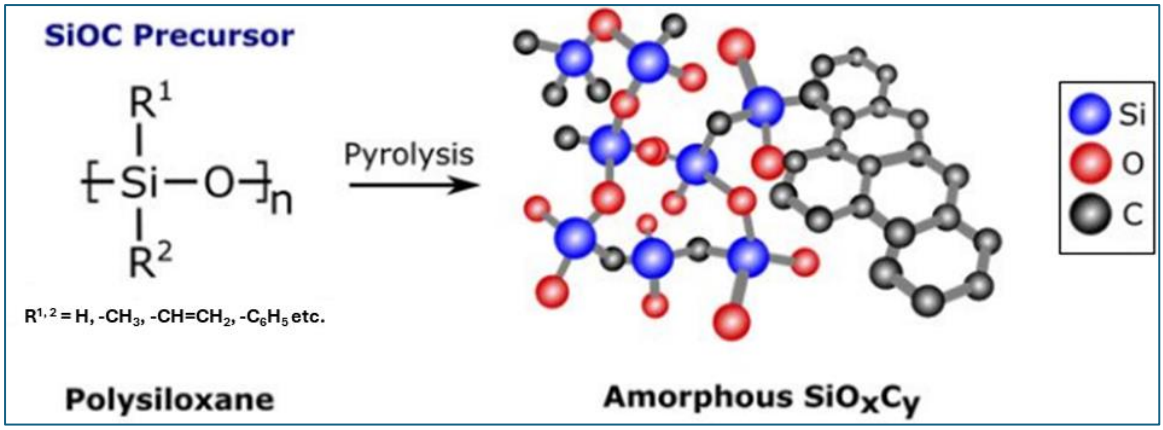

Figure 1.3: common precursors used in synthesis of polymer-derived SiOC and their microstructures.

1.4 Overview of perovskite materials

1.4.1 Introduction, structural variants, synthesis and Classification

Perovskite materials are a highly adaptable class of ABO_3 crystalline oxides, where differently sized A- and B-site cations coordinate with oxygen. First discovered as $CaTiO_3$ by Gustav Rose in 1839 and later named after Russian mineralogist, Lev Perovski, they are widely studied for their structural flexibility and multifunctionality. In the ideal cubic form, A-site cations occupy cube corners, B-site cations sit at the body center, and oxygen atoms lie at face centers. Their capacity to accommodate varied ionic radii and valence states enables precise tuning of structural and functional behaviour, supporting diverse electronic, catalytic, and optical applications[32,33].

The stability of the perovskite framework is commonly described using the Goldschmidt tolerance factor[34]:

$$t = \frac{r_A + r_O}{\sqrt{2}(r_B + r_O)} \tag{1.1}$$

where r_A, r_B and $r_O (= 0.14\ \text{nm})$ are the ionic radii of the A-site, B-site, and oxygen anion, respectively. A value close to 1 suggests ideal cubic symmetry, while significant deviations ($t < 0.9$ or >1) yield distorted phases with lower symmetry structures, like, tetragonal, orthorhombic, or rhombohedral variants due to octahedral tilting and distortions.

The synthesis route plays a crucial role in determining the phase purity, crystallinity, morphology, and performance of perovskite materials. Common methods include:

- **Solid-state reaction:** This conventional route involves mixing stoichiometric amounts of metal oxides or carbonates, followed by high-temperature calcination (typically above 1000 °C). Though simple and cost-effective, this method often requires repeated grinding and calcining to ensure homogeneity and phase formation. It may also result in larger grain sizes and less control over morphology.
- **Sol–gel and pechini**: These wet chemical methods enable better control over particle size and homogeneity. Metal alkoxides or nitrates are hydrolyzed and polymerized to form a precursor gel, which is then calcined to yield the perovskite phase. The Pechini method further involves citric acid and ethylene glycol to form a polymeric network that encapsulates metal ions, resulting in nanosized, homogenous particles upon combustion and calcination.
- **Hydrothermal and solvothermal:** These techniques involve reacting precursors in a sealed autoclave under elevated temperature and pressure conditions. They are useful for obtaining nanocrystalline perovskites with high phase purity at lower temperatures.
- **Combustion and microwave-assisted:** Self-sustained combustion synthesis and microwave irradiation have been employed to reduce synthesis time and energy consumption while achieving fine particle morphology and high crystallinity.

The method selected depends on the targeted application as: nanostructured perovskites are preferred for catalysis and sensors due to higher surface area, while bulk ceramics are used for ferroelectric and piezoelectric devices[34].

Perovskites are classified based on *symmetry* (cubic $SrTiO_3$, tetragonal/orthorhombic $ZnTiO_3$), *chemical composition* (simple ABO_3, double $A_2BB'O_6$, and layered Ruddlesden–Popper phases), or *functionality* (ferroelectric, magnetoresistive, superconducting, photovoltaic, and catalytic systems). Among catalytic perovskites, $ZnTiO_3$, a metastable ilmenite perovskite type titanate has gained significant interest due to its visible-light photocatalytic activity, wide bandgap tunability, and thermally induced phase transformation from cubic to hexagonal or ilmenite structures. Nanoscale $ZnTiO_3$ particles synthesized via sol–gel[35,36] or combustion route exhibit high surface area and strong oxidative capability, making them suitable for dye degradation, UV-assisted photocatalysis, and membrane-based photoreactors.

1.4.2 Properties and applications

One of the most significant features of perovskites is their outstanding optoelectronic properties. These materials typically possess a direct bandgap that is easily tunable between 1.2 to 2.3 eV by modifying their chemical composition. This makes them excellent candidates for light-harvesting applications, like, solar cells. In addition, perovskites have a high absorption coefficient, long carrier diffusion lengths, and high charge-carrier mobility, which collectively contribute to their efficiency in photovoltaic and photodetection applications[37]. Certain perovskites, particularly perovskite oxides, like, $BaTiO_3$, display ferroelectric and piezoelectric behaviour, meaning they can generate an electric field in response to mechanical stress and vice versa. These materials are also known for their high dielectric constants, which make them valuable in capacitor and memory applications. Moreover, some perovskite oxides exhibit magnetic and superconducting properties. For example, lanthanum manganites demonstrate colossal magnetoresistance, while cuprate-based perovskites, such as, $YBa_2Cu_3O_7$ are high-temperature superconductors. Another notable attribute of perovskites, especially the hybrid organic-inorganic types, is their defect tolerance. Unlike many traditional semiconductors, perovskites can maintain high performance despite having a relatively high density of defects. However, a significant challenge remains in terms of stability. Many perovskite materials, particularly those incorporating organic cations, are sensitive to moisture, heat, and UV exposure. This has led to ongoing research into more stable all-inorganic perovskite compositions[34,38].

The unique and tunable properties of perovskite materials have opened the door to a wide range of applications across multiple technological fields. One of the most prominent areas is in solar energy. Perovskite solar cells (PSCs) have emerged as one of the most efficient and cost-effective alternatives to traditional silicon-based photovoltaics. Since their introduction, PSCs have rapidly achieved power conversion efficiencies exceeding 26%, and ongoing research aims to surpass 30% through tandem configurations with silicon or copper-indium-gallium-selenide (CIGS) cells. Their solution-based, low-temperature fabrication processes also make them highly attractive for large-scale and flexible solar modules. In the field of optoelectronics, perovskites have shown significant potential in devices, such as, light-emitting diodes, photodetectors, and X-ray detectors. Their high luminescence efficiency and tunable emission wavelengths make them suitable for displays and lighting applications. Similarly, their high photoconductivity and fast response times

are beneficial in creating highly sensitive photodetectors. Perovskite oxide materials are gaining traction in electrocatalysis, particularly for applications, such as, the oxygen evolution reaction and oxygen reduction reaction in fuel cells and metal-air batteries. These oxides serve as cost-effective alternatives to platinum-based catalysts. Furthermore, their potential in CO_2 reduction and photocatalytic water splitting holds promise for sustainable fuel generation and carbon capture technologies.

Additionally, some perovskites exhibit promising thermoelectric properties, potentially enabling waste heat recovery in industrial systems. Finally, due to their sensitivity to environmental changes, perovskites are being explored for gas sensing and environmental monitoring. They can detect trace amounts of gases, such as, NO_2 and NH_3, as well as changes in humidity and temperature, making them suitable for smart sensing devices[38–40].

1.4.3 Hexagonal phase of zinc titanate as photocatalytic perovskite material

Zinc titanate ($ZnTiO_3$ or ZTO) is a technologically significant ceramic with an ilmenite-type perovskite-related structure under certain conditions. It exists in both cubic and hexagonal polymorphs (Figure 1.4), the latter being more common at lower temperatures[41]. $ZnTiO_3$ is often studied for its dielectric, photocatalytic, and gas-sensing properties. $ZnTiO_3$ is typically synthesized through sol–gel, combustion, or co-precipitation routes, where controlling temperature is crucial to prevent secondary phases, like, Zn_2TiO_4. Its photocatalytic activity under UV and visible light, especially in water splitting and organic pollutant degradation, is attributed to its suitable band gap (~3.2 eV), stability, and surface area. Furthermore, it has gained attention as a component in microwave dielectric ceramics and as a potential electrode material in lithium-ion batteries. Doping with rare-earth ions or coupling with TiO_2 enhances its performance in environmental and energy-related applications[42–45]. XRD characterization confirms the hexagonal (rhombohedral/ilmenite-type) phase of $ZnTiO_3$, exhibiting lattice parameters of $a \approx 5.077$ Å and $c \approx 13.92$ Å, which are typical of the ilmenite-structured $ZnTiO_3$ polymorph[46].

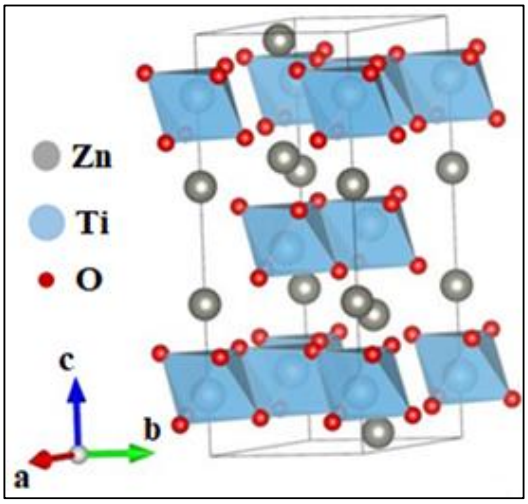

Figure 1.4: Hexagonal (or rhombohedral) crystal structure of $ZnTiO_3$.

1.5 Overview of industrial pollutants

1.5.1 Introduction and types of pollutants

Industrialization, while essential for economic progress, has significantly intensified environmental pollution through the release of harmful substances from activities, such as, textile processing, dyeing, chemical manufacturing, metal mining, and paper production. These industrial pollutants contaminate air, water, and soil, posing long-term threats to ecosystems and human health due to their toxicity, persistence, and complex chemical nature. Aqueous industrial effluents are particularly problematic, often containing stable organic compounds, like, synthetic dyes, that resist conventional treatment methods.

Among these pollutants, methylene blue, a widely used synthetic dye, serves as a model compound for evaluating treatment technologies due to its stability, toxicity, and detectability. Advanced oxidation processes, especially **photocatalysis**, have emerged as promising techniques for addressing such persistent pollutants[47].

Industrial pollutants can be classified into several categories based on their composition and environmental behavior:

- **Organic pollutants:** These include synthetic dyes (e.g., methylene blue), pesticides, phenols, polycyclic aromatic hydrocarbons, and petroleum derivatives. They are typically toxic, non-biodegradable, and capable of bioaccumulation and mutagenesis.
- **Inorganic pollutants:** Mainly comprising heavy metals, such as, lead, mercury,

cadmium, and arsenic, these pollutants originate from activities, like, mining, electroplating, and fertilizer production. They pose chronic health risks due to their non-degradable nature and ability to enter and magnify through the food chain.

- **Gaseous emissions:** Nitrogen oxides (NOx), sulfur dioxide (SO_2), carbon monoxide (CO), carbon dioxide (CO_2), and volatile organic compounds contribute to air pollution, respiratory diseases, and climate change.
- **Suspended and dissolved solids:** Composed of salts, minerals, and particulates, these solids alter water properties, such as, pH, turbidity, and conductivity, impacting aquatic life and water usability.
- **Emerging contaminants:** Pharmaceuticals, endocrine disruptors, microplastics, and engineered nanomaterials represent a new class of pollutants that challenge existing treatment technologies due to their low concentrations, complex structures, and uncertain long-term effects.

Understanding the composition and environmental behaviour of these pollutants is crucial for developing effective and targeted remediation strategies. Because of their resilience and long-term persistence in environmental matrices, there is a growing need for more advanced and sustainable treatment techniques capable of completely degrading or detoxifying these contaminants[48].

1.5.2 Redemption techniques for industrial pollutants

The process of redemption (removal or detoxification) of industrial pollutants in Table 1.1, encompasses a range of physical, chemical, biological, and advanced oxidation approaches. Each method varies in effectiveness, cost, environmental impact, and scalability.

Table 1.1: Conventional methods of pollutants treatment with limitations and mechanism.

Method	Mechanism	Drawbacks
Adsorption	Pollutants bind to porous media (e.g., activated carbon)	Saturation, regeneration required
Coagulation-Flocculation	Particulate aggregation using chemicals	Sludge generation, chemical use
Chemical Precipitation	Converts solutes into insoluble compounds	Limited to metals, secondary waste
Biological Treatment	Microbial degradation of organic matter	Slow, ineffective for toxic or stable dyes
Membrane Filtration	Physical separation of solutes	Expensive, prone to fouling

To overcome the limitations of traditional methods, **photocatalysis** has emerged as a powerful and sustainable technique for degrading industrial pollutants, especially synthetic dyes, like, methylene blue.

1.5.3 Methylene blue as a model pollutant

Methylene blue (MB), with the chemical formula $C_{16}H_{18}ClN_3S$, is a synthetic, water-soluble cationic dye from the thiazine class. It is extensively used in textile, paper, leather, and biomedical industries for its vivid blue colour, high chemical stability, and strong affinity for fabrics and organic matter. Beyond industrial use, it also has clinical applications, such as, treating methemoglobinemia and serving as a biological stain in laboratories. However, when discharged untreated into water bodies, methylene blue poses significant environmental and ecological threats.

Even at low concentrations, methylene blue causes intense coloration of water, impairs light penetration, and disrupts photosynthetic activity in aquatic ecosystems. It exhibits cytotoxic, genotoxic, and neurotoxic effects on aquatic organisms and can bioaccumulate through the food chain. Additionally, its strong adsorption to sediments and resistance to microbial degradation make it persistent in natural environments and challenging to remove via conventional wastewater treatment processes. Prolonged exposure may also have adverse effects on human health, including irritation, nausea, and hemotoxicity.

Due to its environmental stability and well-characterized optical properties—particularly its strong absorbance peak near 664 nm in the visible light region—methylene blue is widely used as a model pollutant in laboratory studies. It serves as a reliable indicator for evaluating the performance of emerging water treatment technologies, especially advanced oxidation processes, like, photocatalysis. Its predictable degradation pathway and ease of spectrophotometric monitoring allow researchers to assess kinetic behaviour, reaction mechanisms, and optimize parameters, such as, pH, catalyst dosage, and light intensity. As such, methylene blue continues to play a crucial role in the development and benchmarking of sustainable pollutant remediation techniques[49].

1.5.4 Photocatalysis as an advanced oxidation process

Photocatalysis is a prominent advanced oxidation process[50] that utilizes semiconductor materials, such as, titanium dioxide (TiO_2), zinc oxide (ZnO), zinc titanate ($ZnTiO_3$), bismuth ferrite ($BiFeO_3$), and graphitic carbon nitride (g-C_3N_4) to degrade pollutants under

light irradiation. When exposed to ultraviolet or visible light, these semiconductors absorb photons and generate electron-hole pairs (e^-/h^+) through the following fundamental reaction:

$$\text{Semiconductor} + h\nu \rightarrow e^- + h^+$$

The photoexcited electrons (e^-) reduce molecular oxygen to form superoxide anions ($O_2\bullet^-$), while the holes (h^+) oxidize water or hydroxide ions to generate hydroxyl radicals (•OH):

$$e^- + O_2 \rightarrow O_2\bullet^-$$

$$h^+ + H_2O/OH^- \rightarrow \bullet OH$$

These reactive oxygen species (ROS) are highly oxidative and non-selective, enabling them to attack and break down complex organic molecules, such as, methylene blue. The degradation pathway typically involves the transformation of MB into smaller intermediates, which are ultimately mineralized into CO_2, H_2O, and inorganic salts:

$$MB + \bullet OH/O_2\bullet^- \rightarrow \text{Intermediates} \rightarrow CO_2 + H_2O + \text{Mineral Salts}$$

Photocatalysis offers several distinct advantages:

- Complete mineralization of organic pollutants without generating harmful secondary waste.
- Utilization of solar energy, making the process sustainable and cost-effective.
- Applicability to a broad spectrum of contaminants, including both organic and inorganic compounds.
- Application to Methylene Blue Degradation

Photocatalysis has been extensively studied for the degradation of methylene blue due to the dye's stability, toxicity, and ease of detection via its characteristic absorption at ~660 nm. A range of photocatalytic materials—including TiO_2, ZnO, $BiVO_4$, and various perovskite-based catalysts—have shown high efficacy under different light sources.

The efficiency of photocatalytic degradation is influenced by several key parameters:

- Type and concentration of photocatalyst
- Initial concentration of methylene blue

- pH of the solution
- Intensity and wavelength of the incident light
- Exposure duration

Under optimized conditions, up to 90–100% degradation of methylene blue can be achieved within a few hours. These findings highlight the potential of photocatalysis as a robust and environmentally friendly strategy for the treatment of dye-laden industrial effluents[51,52].

1.6 Overview of thermal energy storage and phase change materials

1.6.1 Introduction to thermal energy storage and classification

The need of energy storage is essential to fulfill the unpredictable and fluctuating demand in future. To overcome the energy crises and meet this challenge various energy storage materials were studied by researchers across the globe for many decades, still a lot of potential is to be explored from the intermittency of primary sources of renewable energy.

As an energy storage approach, the present work is focused on thermal energy storage and its retrieval. Thermal Energy Storage (TES) is a technology in which thermal energy (either heat or cold) is stored through a storage medium and used later when needed.

Various TES technologies and applications exist. The selection of a TES system for a particular application depends on many factors, including storage duration, economics, supply and utilization temperature requirements, storage capacity, heat losses and available space, thereby making it suitable for applications in building air-conditioning, textile, heat exchanger and packed bed designs, thermal management of electronics, solar power plants and space systems.

TES systems are categorized into three main groups: Thermochemical heat storage, Sensible heat storage and Latent heat storage system.

Thermochemical heat storage (TCHS)[53–55] is based on storing chemical energy after dissociation reaction and then recovering the same in a chemically reversed reaction. In the simplest case, a reactant A is transformed and are stored separately in the products B and C in an endothermic reaction during the charging step. Discharge then accounts for the reversible process, in which B and C are recombined, releasing thermal energy, described by equation (1.2).

$$A + \Delta H_r \leftrightharpoons B + C \tag{1.2}$$

The stored heat (Q) is proportional to the molar reaction enthalpy (ΔH_r), the number of moles of one of the products(n_B) and the conversion achieved (X) according to the relation (1.3)

$$Q_{thermochemical} = X n_B \Delta H_r \tag{1.3}$$

Sensible heat storage (SHS) is the most mature and widely used TES option due to its simple principle and low costs, however, it also has the lowest heat storage density among the three types of TES. In SHS, heat is stored by raising the temperature of a liquid or solid and released by decreasing the temperature when necessary. Common SHS materials include water, thermal oils, molten salts, concretes and rocks[56]. The amount of heat stored depends on the specific heat of the medium, the temperature change, and the amount of storage material[57].

$$Q_S = \int_{t_i}^{t_f} mc_p dT = mc_p(t_f - t_i) \tag{1.4}$$

where Q_S is the quantity of heat stored, in Joules; m is the mass of heat storage medium, in kg; c_p is the specific heat, in J/(kg·K); $t_i$and t_f are the initial and final temperature, in °C respectively.

1.6.2 Phase change materials (PCMs) for latent heat storage and its classification

LHS materials are known as phase change materials (PCMs). As the name suggests, a material that changes phase (solid, liquid and gas) owing to the releasing or absorbing of thermal energy during melting or solidification and capable of storing latent heat at a certain temperature is called as Phase Change Material or Latent Heat Storage Material.

Latent heat storage may be classified based on the phase change process as solid-solid, solid-liquid, solid-gas, and liquid-gas (Figure 1.5). Solid-gas and liquid-gas transformations are generally not employed for energy storage despite their high latent heats, because gases occupy large volumes. In solid-solid transitions, heat stored as the material is transformed from one crystalline form to another. These transitions generally have small latent heats making such materials less desirable. LHS by solid-liquid phase transition is a particularly attractive technique as it provides a high energy storage density. Moreover, it has the capacity to store energy as latent heat of fusion at a constant temperature corresponding to the phase transition temperature of the PCM[58].

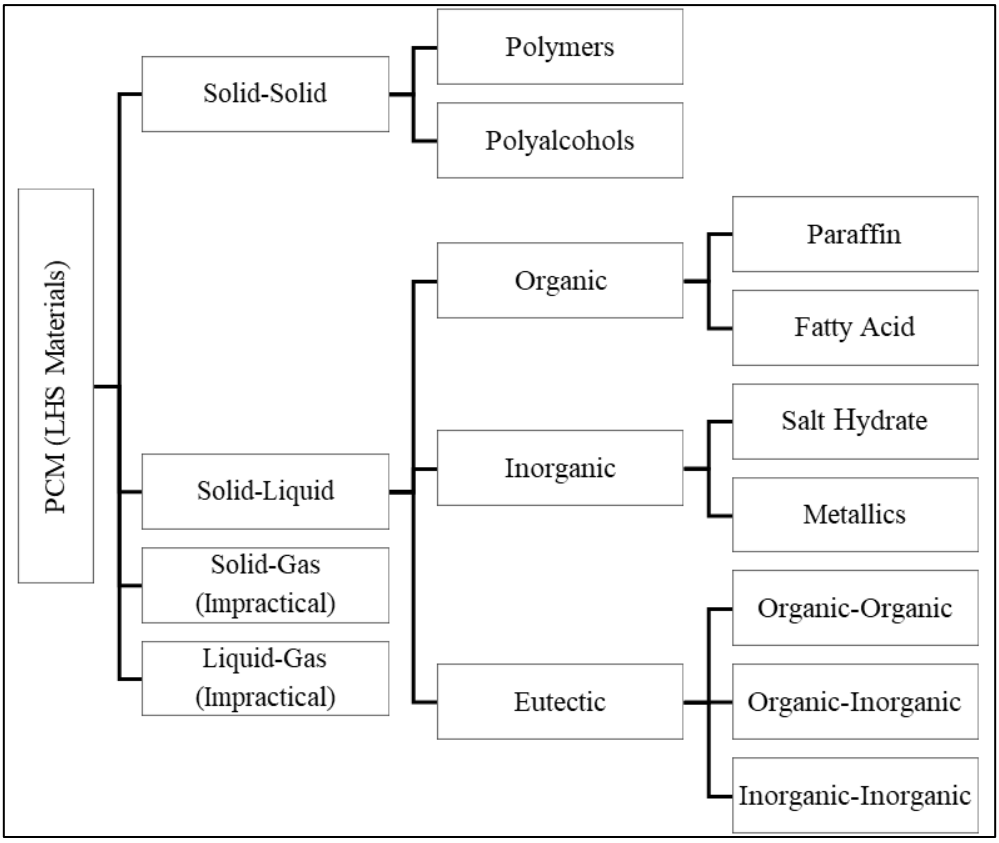

Figure 1.5: Classification of Phase Change Materials.

PCMs can also be categorized according to their phase transition temperatures: low-temperature PCMs (melting point < 220°C), intermediate-temperature PCMs (220°C ≤ melting point ≤ 420°C), and high-temperature PCMs (melting point > 420°C)[59].

1.6.3 Properties, applications and working principle of PCMs

The desirable properties of PCM to be used for LHS are as follows[60]:

(i) High value of the heat of fusion and specific heat per unit volume and weight.
(ii) Melting point which matches the application.
(iii) Low vapor pressure (< 1 bar) at the operational temperature.
(iv) Chemical stability and non-corrosiveness.
(v) Should not be hazardous, highly inflammable or poisonous.
(vi) Should have a reproducible crystallization without degradation.
(vii) Should have a small supercooling degree and high rate of crystal growth.
(viii) Should have a small volume variation during solidification.
(ix) High thermal conductivity.
(x) Should be of abundant supply and at a low cost.

Phase Change Materials (PCMs) are being used for energy storage and thermal abatement in a wide range of applications. These applications cover a wide range of sizes: from small portable electronics to large-scale concentrating solar plants; and a wide range of temperatures: from the −40°C of space-based application to the 500°C and up of solar energy applications[61].

As the source temperature rises, the chemical bonds within the PCM breaks, and the material changes its phase from solid to liquid. During the charging process, the material begins to melt when the phase change temperature is reached. The temperature then stays constant until the melting process is finished. The heat that is stored during the phase change process (melting process) of the material at a quite constant temperature, is called the Latent Heat. It follows an isothermal behaviour during the charging and discharging processes[62].

The main advantage of using LHS over SHS is its ability to store and release heat at an almost constant temperature. Initially, these materials behave like SHS materials, where the temperature rises linearly with system enthalpy. However, once the phase change temperature is reached, heat is absorbed or released at nearly constant temperature as the material changes its physical state from solid to liquid, liquid to gas, or vice versa[57]. The heat storage capacity Qs, in J, of the LHS system with a PCM medium is given by:

$$Q_S = \int_{t_i}^{t_m} mc_{ps}dT + mf\Delta q + \int_{t_m}^{t_f} mc_{pl}dT = m[c_{ps}(t_m - t_i) + f\Delta q + c_{pl}(t_f - t_m)] \quad (1.5)$$

where t_m is the melting temperature, in ◦C; m is the mass of PCM medium, in kg; c_{ps} is the average specific heat of the solid phase between t_i and t_m, in kJ/(kg·K); c_{pl} is the average specific heat of the liquid phase between t_m and t_f, in J/(kg·K); f is the melt fraction; Δq is the latent heat of fusion, in J/kg.

1.7 Overview of separation processes

1.7.1 Introduction, broad classification and significance

Separation processes are foundational operations designed to isolate, purify, enrich, or recover one or more components from a mixture. These processes are critical in both upstream and downstream operations, enabling the conversion of raw material soften

naturally occurring, impure, or complex into valuable products of specified purity and composition[63]. In industrial practice, raw inputs are rarely found in their pure form; thus, the ability to selectively extract desired components or remove undesirable contaminants is central to product quality, process efficiency, economic viability, and environmental sustainability.

From crude oil distillation and natural gas purification to the production of pharmaceuticals, polymers, food ingredients, and drinking water, separation technologies play an indispensable role. Virtually every industrial plant whether it operates in petrochemicals, food and beverages, pharmaceuticals, environmental engineering, or biotechnology relies on one or more separation processes to meet technical specifications, comply with regulatory standards, and optimize resource utilization. In many industries, separations account for a significant portion of operational costs and energy consumption. For example, in bulk chemical manufacturing, separations can consume over 45–55% of the total energy used in a plant, emphasizing their economic and environmental impact[64].

Separation processes are broadly classified based on the primary property or driving force used to differentiate between components of a mixture. These properties may include:

- Particle size – used in filtration and sieving.
- Density – used in centrifugation and sedimentation.
- Volatility or boiling point – used in distillation and evaporation.
- Solubility or chemical affinity – used in extraction and crystallization.
- Diffusivity or molecular mobility – used in membrane separations, like, dialysis and pervaporation.
- Electrostatic or magnetic susceptibility – used in electrophoresis or magnetic separation.

Each of these separation categories operates under unique principles and conditions, requiring specialized equipment and control strategies. Furthermore, the choice of separation method depends heavily on the physical state of the mixture (solid-liquid, liquid-liquid, gas-liquid, etc.), composition, desired separation efficiency, product purity, energy demand, and economic feasibility[65].

Among the wide array of techniques, **mass transfer-based separation processes** have emerged as particularly significant, especially for complex or sensitive systems. These

processes involve the movement of species between two phases, such as, from liquid to liquid (in liquid-liquid extraction), gas to liquid (in gas absorption), or liquid through a membrane (in pervaporation or reverse osmosis) driven primarily by concentration gradients. Unlike thermal methods, which depend on differences in boiling points and often require substantial heat input, mass transfer-based methods typically operate at lower temperatures, making them ideal for heat-sensitive materials, like, biological molecules, solvents, or pharmaceuticals[66].

Additionally, mass transfer-based techniques offer greater selectivity, allowing for the separation of components that have very similar boiling points or physical characteristics but differ in chemical affinity or diffusivity. This makes them especially valuable for azeotropic separations, trace contaminant removal, or recovery of high-value products from dilute streams applications where conventional distillation or mechanical filtration might fail or prove inefficient[67].

In contemporary industrial practice, separation processes are not isolated steps but are often integrated or hybridized with other operations to enhance overall efficiency[68]. For instance, a process may combine liquid-liquid extraction with membrane separation (e.g., pervaporation) to achieve higher selectivity and purity[69]. Such hybrid systems represent a new frontier in separation science, providing innovative solutions to traditional challenges in energy consumption, throughput limitations, and environmental compliance[70].

1.7.2 Pervaporation process

Pervaporation is a selective membrane-based, mass transfer process that separates components from liquid mixtures through a dense, non-porous membrane via the solution–diffusion mechanism comprising sorption onto the membrane, diffusion driven by chemical potential gradients, and desorption as vapor under vacuum or sweep conditions. Its performance depends on interfacial mass transfer, diffusion kinetics, and vapor removal, with behaviour governed by Fick's law and thermodynamic partitioning. Polymeric membranes, such as, hydrophilic PVA for water–alcohol separations and organophilic PDMS for volatile organics, are prevalent, while mixed matrix membranes (MMMs) incorporating MOFs, zeolites, or carbon nanotubes demonstrate enhanced permeability-selectivity trade-offs. Operating at lower temperatures than conventional distillation, pervaporation bypasses azeotropic constraints and requires lower energy input, making it energy-efficient. Hybrid distillation–pervaporation systems further reduce energy demand,

such as, ethanol dehydration systems that achieve substantial energy savings compared to pure distillation. Applications span ethanol dehydration, recovery of volatile organic compounds, wastewater treatment, and purification of heat-sensitive pharmaceuticals. Despite advantages, like, modularity, mild thermal operation, and hybrid compatibility, limitations include lower permeation flux, susceptibility to fouling, and higher costs for advanced membranes[71–73]. These can be mitigated through intensified designs, such as, thin asymmetric membranes, hollow fibers for high surface area, and coiled flow inverters for reduced concentration polarization.

1.7.3 Liquid-liquid extraction (LLE)

Liquid–Liquid Extraction (LLE)—also called solvent extraction or partitioning—is a mass transfer-driven separation in which a solute is selectively transferred from one liquid phase into another immiscible or partially miscible liquid, typically an aqueous phase and an organic solvent. The driving force is the difference in solubility between the two phases, expressed by the partition coefficient. Industrial applications span pharmaceuticals, petrochemicals, hydrometallurgy, biotechnology, and environmental remediation, where it is used for extracting compounds, such as, organic acids, antibiotics, alkaloids, aromatic hydrocarbons, and metal ions. Its ability to operate at low temperatures makes it suitable for thermally sensitive compounds, and its selectivity is valuable in systems with close boiling points or azeotropic behavior. Extraction efficiency is governed by factors, such as, solvent selection, pH, ionic strength, temperature, contact time, and solvent-to-feed ratio. Advanced configurations, such as, coiled flow inverters (CFIs), centrifugal contactors, and micro extractors—enhance mass transfer by increasing interfacial area and reducing residence time. In ternary systems, equilibrium analysis using ternary phase diagrams is essential to optimize solvent ratios and predict phase behavior, as seen in the extraction of acetic acid from water–toluene mixtures or similar multicomponent systems in hydrometallurgy.

Although versatile, LLE has drawbacks including solvent losses, slow phase separation, and environmental concerns related to solvent toxicity and flammability. Dilute systems often require large solvent volumes, affecting process economy. Emerging approaches address these issues through greener solvents, like, ionic liquids (ILs) and deep eutectic solvents (DESs), which offer higher selectivity, low volatility, and reduced environmental impact. Hybrid systems that combine solvent extraction with membrane-based techniques,

such as, pervaporation or nanofiltration are gaining prominence for their improved selectivity, reduced energy use, and scalability. This complementary integration of solvent-based and membrane-based methods allows process designers to harness the strengths of each, bridging conventional extraction principles with modern membrane separation technologies[74,75].

1.8 Objective of thesis work

The main objectives of this thesis are to utilise the PDMS material to design and synthesize its various membranes and continuous reactor, CFI in their neat and composite form (particle loaded) and study the applications of photocatalysis, pervaporation, liquid-liquid separation and thermal energy storage which are listed point-wise below as:

- Continuous enhanced photocatalytic removal of methylene blue from wastewater using a PDMS-coiled flow inverter reactor functionalized with plasma-activated $ZnTiO_3$ nanoparticle suspension.
- Fabrication and performance comparison of pristine and SiOC-impregnated PDMS membranes for the pervaporation separation of ethanol from an equivolume ethanol–water mixture.
- Development of a millifluidic PDMS-CFI for efficient extraction and mass transfer of acetic acid from an acetic acid–toluene (1:9 v/v) and water mixture.

The above-mentioned topics directly relate to the theme of the thesis. In addition, I have also done some work on PCM based polymeric thermal energy storage system.

- Development of phase change material-loaded PDMS membranes for thermal energy storage applications.

1.9 Thesis outline

This thesis presents the design, fabrication, characterization, and application of polydimethylsiloxane (PDMS)–oxide particles based composite structures for continuous photocatalytic reactor and mass transfer applications, including pervaporation and liquid–liquid extraction, along with thermal energy storage. In this work, commercial Sylgard 184 PDMS was employed as the primary soft matrix due to its optical transparency, flexibility, chemical inertness, hydrophobicity, elastomeric behavior, and facile processability into membranes, coatings, and coiled flow inverter (CFI) geometries in both neat and particle-

impregnated forms. Neat PDMS-based CFIs were developed for continuous liquid–liquid extraction (LLE), whereas PDMS-coated CFIs infused with plasma-treated zinc titanate ($ZnTiO_3$) particles were utilized for visible-light-induced photocatalytic degradation in aqueous systems. In parallel, neat PDMS membranes and silicon oxycarbide (SiOC)-impregnated PDMS membranes were fabricated and evaluated for pervaporation-based ethanol–water separation, with emphasis on selective transport enhancement. Additionally, stearic acid-loaded PDMS membranes were developed as flexible phase change material (PCM) composites for thermal energy storage applications.

The incorporation of oxide, ceramic, and functional fillers into the PDMS matrix demonstrates a versatile strategy for developing multifunctional soft composite structures. These systems combine material design, photocatalytic functionality, membrane-based separation, mass transfer enhancement, and thermal energy storage within a unified PDMS-based soft-structure framework.

The **first chapter** begins with the detailed motivation and introduction, emphasizing the need to integrate soft material design with process intensification. It provides an overview of the key materials used in the study, including PDMS, polymer-derived ceramics, with particular emphasis on SiOC, and perovskite-type oxide materials, especially $ZnTiO_3$, as functional fillers, highlighting their synthesis, structure, properties, applications and limitations. The chapter further discusses industrial pollutants, particularly methylene blue as a model dye, introduces photocatalysis as an advanced oxidation process for pollutant degradation, thermal energy storage using phase change materials and mass transfer-based separation processes including pervaporation and liquid–liquid extraction. Finally, the chapter defines the thesis objectives, and presents the overall thesis outline.

The second chapter presents the experimental framework of the study, including the synthesis methods, materials, instruments, and characterization techniques used throughout the thesis. It discusses general nanomaterial synthesis routes with emphasis on the sol–gel method and describes the materials employed for fabricating PDMS-based composite structures. The chapter further outlines the analytical methods used to evaluate the structural, morphological, optical, thermal, and transport properties of the developed systems.

Chapter three describes the development of a transparent PDMS-lined coiled flow inverter impregnated with plasma-treated $ZnTiO_3$ particles for continuous visible-light

photocatalytic degradation of methylene blue dye. In addition to reactor fabrication and performance analysis, the chapter defines the relevant research gaps, discusses the challenges encountered during photocatalyst immobilization and reactor operation, compares the system with related photocatalytic studies, and briefly notes the unresolved aspects in the summary section. The reactor was prepared by coating the inner surface of a silicone tube with PDMS, followed by curing, swelling the coating with Tetrahydrofuran (THF), and incorporating plasma-treated $ZnTiO_3$ particles into the PDMS layer through particle suspension. Plasma treatment improved the dispersibility and suspension stability of $ZnTiO_3$ particles, while the optical transparency of PDMS enabled light penetration and photocatalytic activation. Photocatalytic experiments were conducted using 10 ppm methylene blue solution at six different flow rates under a 25 W white LED source. The performance of the CFI reactor was compared with that of a straight tube of equal length. The illuminated CFI showed a pseudo-first-order rate constant of $24.66 \pm 6.28 \times 10^{-3}$ min^{-1}, which was more than two times higher than that of the illuminated straight tube and about five times higher than dark operation. This chapter establishes the feasibility of using $ZnTiO_3$-impregnated PDMS-lined CFIs for compact, continuous-flow photocatalytic wastewater treatment.

The **fourth chapter** is dedicated to the fabrication and comparison of neat and SiOC-impregnated PDMS membranes for pervaporation separation of ethanol from an ethanol–water mixture. The chapter further places the membrane study in context by presenting its research gaps, experimental challenges and corresponding resolutions, comparison with relevant PDMS-based pervaporation literature, and brief unresolved aspects in the summary section. SiOC particles were synthesized through low-temperature thermal degradation of PDMS sponge and showed high surface area (~192 m^2 g^{-1}) and porous amorphous Si–O–C characteristics. These particles were selectively infused into one surface of a swollen PDMS membrane using a diisopropylamine-based suspension, producing an asymmetric membrane structure. The SiOC incorporation modified the membrane morphology, increased surface hydrophilicity, broadened pore-size distribution, and altered the transport pathway. Pervaporation studies at 298 K demonstrated that SiOC-impregnated membranes improved ethanol–water separation performance, showing approximately 150% enhancement in separation factor compared with native PDMS membranes. The improvement is explained through a mixed solid–liquid diffusion mechanism created by localized hydrated SiOC domains.

Chapter five reports the fabrication and application of a millifluidic PDMS-based coiled flow inverter for continuous liquid–liquid extraction of acetic acid from a biphasic acetic acid–toluene and water system. To support the experimental findings, the chapter identifies the specific research gaps, summarizes the major practical challenges and adopted resolutions, benchmarks the present extraction system against relevant extraction and mass transfer reports, and briefly includes unresolved aspects in the summary section. The CFI was fabricated by casting PDMS around a removable helical PVA filament, producing a coiled millichannel after filament dissolution. The cured PDMS rod was sectioned and reconnected to form four sequential 90° inversions, enabling periodic reorientation of the flowing phases. Extraction experiments were conducted by varying aqueous and organic phase flow rates. The study revealed that the aqueous phase flow rate had a stronger influence on extraction performance than the organic phase flow rate. The maximum overall volumetric mass transfer coefficient obtained was 0.007145 s^{-1} under the highest aqueous flow condition. This chapter demonstrates the potential of PDMS-based CFIs as compact, scalable, and efficient devices for continuous liquid–liquid extraction.

Chapter six shifts focus to the fabrication and characterization of stearic acid embedded PDMS membranes for thermal energy storage. Alongside the experimental investigation, the chapter outlines the research gaps, records the challenges and resolution measures, compares the present membranes with related PCM-based systems, and briefly presents unresolved aspects in the summary section. Composite membranes were fabricated using the doctor-blading method by varying stearic acid loading from 5.7 to 23.3 wt% and THF volumes, 2 and 4 mL. FTIR confirmed the successful physical incorporation of stearic acid within the PDMS matrix with negligible residual solvent. DSC analysis showed stable melting temperatures around 56 °C and crystallization temperatures around 52–53 °C. Latent heat increased from approximately 2.7 to 34.3 J g^{-1} with increasing stearic acid content. However, latent heat utilization efficiency reached a maximum of nearly 80% at approximately 19.5 wt% stearic acid and declined slightly at higher loading due to confinement-limited crystallization. Cooling analysis showed that the PDMS matrix significantly reduced the cooling rate and increased the thermal time constant, confirming improved thermal inertia and controlled heat-release behavior. This chapter establishes the suitability of flexible PDMS–PCM membranes for thermal energy storage applications.

Finally, **chapter seven** provides the conclusions, specified as subjective and objective conclusions and future scope of the thesis. It summarizes the major outcomes from all experimental chapters.

Chapter 2: Synthesis Methods, Materials and Characterization Techniques

2.1 Nanomaterials synthesis techniques

Nanomaterials can be synthesized using a wide range of physical, chemical, and biological techniques, broadly categorized into Top-Down and Bottom-Up approaches[76]. In Top-Down approaches, larger bulk materials are physically or chemically broken down into nanoscale structures. These methods include mechanical milling, such as, ball milling, lithography (including photolithography and electron beam lithography), laser ablation, and various etching techniques, like, reactive ion etching. These techniques are well-suited for patterning and structuring materials but can lead to structural defects and limited control over uniformity.

In contrast, Bottom-Up approaches involve assembling nanostructures from atoms, molecules, or smaller particles. These include chemical vapor deposition (CVD), sol-gel processing, hydrothermal and solvothermal synthesis, co-precipitation, self-assembly, microemulsion techniques, and biological synthesis. Bottom-Up methods often provide better control over composition, size, and crystallinity, making them ideal for producing uniform nanoparticles with specific properties. Among these, the Sol-Gel method is particularly popular for synthesizing metal oxide nanoparticles and thin films due to its simplicity, low processing temperature, and versatility.

Other Specialized Methods include electrochemical synthesis in which Nanomaterials are generated through electrochemical reactions, typically on an electrode surface. This is widely used for producing nanowires, nanotubes, and layered materials. In Flame Spray Pyrolysis a precursor solution is sprayed into a flame, resulting in rapid formation of nanoparticles. It is fast, scalable, and suitable for oxide nanoparticles, but control over particle size can be complex. Atomic Layer Deposition (ALD) is a precise thin-film deposition technique where nanolayers are formed one atomic layer at a time. It is highly controlled and used for coatings in electronics and catalysis.

The choice of synthesis method depends on factors, such as:

- Desired nanomaterial (metal, oxide, carbon-based, etc.)
- Shape and size control

- Purity and crystallinity
- Cost and scalability
- Environmental impact

For instance, CVD is excellent for carbon nanomaterials, while sol-gel is commonly used for silica or titania nanoparticles. Green synthesis is gaining traction in biomedical and environmental applications for its non-toxic nature[77,78].

2.1.1 Sol-gel synthesis: introduction and principle

The sol–gel method is a versatile wet-chemical route for synthesizing advanced inorganic materials, especially metal oxides, such as, silica (SiO_2), titania (TiO_2), and zinc titanate ($ZnTiO_3$). The process is based on the transformation of a colloidal suspension or solution ("sol") into a continuous solid network ("gel"). Typically, it begins with the hydrolysis and condensation of metal alkoxides or metal chlorides in aqueous or alcoholic media, leading to a three-dimensional network containing both a solid phase and a solvent phase[79,80]. The following are the key steps in sol-gel synthesis method:

Preparation of precursors

The sol-gel route typically uses metal alkoxides [$M(OR)_x$] or metal salts as starting precursors. These are chosen based on the desired final material and its properties.

Hydrolysis

Hydrolysis involves the reaction of the metal alkoxide with water:

$$M(OR)_x + H_2O \rightarrow M(OH)(OR)_{x-1} + ROH$$

This step introduces hydroxyl groups into the structure and initiates sol formation.

Condensation

Following hydrolysis, condensation reactions occur, linking hydrolyzed species together:

- Alcohol condensation:

$$M–OH + M–OR \rightarrow M–O–M + ROH$$

- Water condensation:

$$M–OH + M–OH \rightarrow M–O–M + H_2O$$

These reactions lead to the formation of a three-dimensional network (gel).

Gelation

As the condensation progresses, the sol becomes more viscous and eventually forms a gel. The gel contains a significant amount of solvent trapped in its porous network.

Aging

The gel is aged to strengthen the network through continued condensation and syneresis (expulsion of solvent).

Drying

Drying removes the remaining solvent from the gel. The method of drying influences the final material morphology: Ambient drying produces xerogels, Supercritical drying yields aerogels, with highly porous structures and freeze drying results in cryogels.

Calcination

To obtain the final ceramic or crystalline material, the dried gel is calcined at elevated temperatures (usually 300–900°C). This step removes organic residues and promotes crystallization.

A schematic representation of the key steps is shown below.

Metal Alkoxides/Salt → Hydrolysis → Condensation → Gelation → Aging → Drying → Calcination → Final Material

2.1.2 Advantages, limitations, and applications of sol-gel synthesis

The sol-gel approach offers precise control over chemical composition and structural features at the molecular level, enabling tailored material properties for a broad range of applications. Its versatility allows the formation of various morphologies, including powders, thin films, fibers, monoliths, and porous structures. A key advantage is the ability to customize porosity, surface area, and nanostructure—critical parameters for catalysis, sensor design, and membrane technology. The process typically involves simple equipment, is cost-effective at small scales, and supports the incorporation of dopants or organic/inorganic modifiers to produce multifunctional or hybrid materials. Additionally, when water-based systems are used instead of organic solvents, the sol-gel method can be environmentally friendly.

However, the technique has limitations. It involves multiple steps; hydrolysis, condensation, gelation, aging, drying, and calcination that require careful control and can

be time-consuming. Drying stages may induce shrinkage or cracking due to capillary forces, especially in monoliths and films, compromising structural integrity. The process is sensitive to parameters, like, pH, temperature, solvent type, and precursor concentration, making reproducibility challenging. Moreover, many metal alkoxide precursors and solvents are volatile or hazardous, demanding safe handling and disposal. Incomplete hydrolysis or condensation can leave residual organics, necessitating high-temperature calcination to achieve purity. Scaling up from laboratory to industrial production also poses difficulties due to process complexity and costs.

Despite these challenges, sol-gel synthesis is widely applied across diverse fields. It enables fabrication of high-surface-area metal oxides for catalysis, photocatalysis, environmental remediation, and hydrogen generation. In optics and electronics, it is used for anti-reflective coatings, dielectric layers, and electrochromic films. Biomedical applications include bioactive glasses for bone regeneration and porous matrices for controlled drug release. The tunable porosity and surface chemistry of sol-gel materials make them ideal for sensitive chemical and gas sensors. Additionally, sol-gel-derived membranes serve in separation processes, like, pervaporation and ultrafiltration due to their selectivity and thermal stability. Other uses span energy storage materials, protective coatings, corrosion resistance, surface modification, and biomolecule immobilization in biosensors. Collectively, these applications highlight the sol-gel method's pivotal role in advancing materials science and engineering[79,81].

All the synthesis techniques discussed above have been tabulated for its merits, demerits and application domains and presented below in *Table 2.1*.

Table 2.1: Summary table for nanomaterial synthesis techniques including merits, demerits and application domains.

No	Synthesis Technique	Type	Merits	Demerits	Application Domains
1	Mechanical Milling / Ball Milling	Top-Down	Simple, scalable	Defects, contamination, poor uniformity	Metal/ceramic nanopowders, alloying
2	Lithography (Photolithography, E-beam)		High precision, excellent patterning	Expensive, complex, limited to flat surfaces	Microelectronics, MEMS/NEMS

3	Laser Ablation		High-purity nanoparticles, solvent-free	Low yield, high energy consumption	Metallic nanoparticles, nano-inks
4	Etching (Reactive Ion Etching, Wet Etching)		Controlled micro/nanopatterning	Surface damage, harsh chemicals	Semiconductor fabrication, surface texturing
5	Chemical Vapor Deposition (CVD)	Bottom-Up	High purity, good crystallinity	High temperature, expensive equipment	CNTs, graphene, thin films
6	Sol–Gel Method		Low temperature, good compositional control	Cracking/shrinkage during drying	Metal oxide nanoparticles, coatings
7	Hydrothermal / Solvothermal		Good size/morphology control	Requires high-pressure autoclaves	Photocatalysts, nanowires
8	Co-precipitation		Simple, low-cost, scalable	Limited size control	Magnetic nanoparticles, oxides
9	Self-Assembly		Highly ordered nanostructures	Sensitive to conditions	Photonic crystals, supramolecular systems
10	Microemulsion Method		Uniform nanoparticles, good size control	Surfactant contamination	Biomedical nanocarriers, metal nanoparticles
11	Biological / Green Synthesis		Eco-friendly, non-toxic	Slow, limited control	Biomedical and environmental remediation
12	Electrochemical Synthesis	Specialized Techniques	Good control over nanowires/nanotubes formation	Limited to conductive substrates	Sensors, electrocatalysis
13	Flame Spray Pyrolysis (FSP)		Fast, continuous, scalable	Difficult size control	Catalysts, oxide nanopowders
14	Atomic Layer Deposition (ALD)		Atomic-level precision, conformal coatings	Slow, costly	Electronics, catalytic layers

2.2 Characterization instruments used in this work

Descriptions of the characterization instruments with their make, origin, model number used across the four experimental chapters, through 3 to 6, are presented in this section.

Crystallinity/amorphousness of the silicon oxy-carbide particles was characterized using a Panalytical/Empyrean X-ray diffractometer with Cu Kα (λ = 1.5406 Å) radiation. High-resolution transmission electron microscope (HR-TEM) images of the particles were captured using the JEOL instrument (model Neoarm/JEM-ARM200F, AMI 300). The specific surface area of silicon oxy-carbide particles has been estimated by BET analyzer (model, MicrotracBEL, Max II) with nitrogen used as the adsorptive/desorptive gas. Morphological analysis was carried out using a JEOL JSM-7900F scanning electron microscope (SEM), which was also equipped with an energy-dispersive X-ray (EDX) detector. This instrument was employed for both cross-sectional imaging of PDMS-based membranes and compositional analysis of SiOC and $ZnTiO_3$ particles, using an accelerating voltage of 5–15 kV and a working distance of 15 mm. Porometry measurements were conducted using a Tech-Poro-AL-500 capillary flow porometer (Tech Inc.).

Surface-wetting characteristics of the membranes were examined using an Apex Instruments Acam-NSC contact angle meter with an ellipse-fitting algorithm. The analysis of a fraction of the permeate obtained from the pervaporation of the ethanol-water mixture was quantified by using a Nucon 5765 gas chromatograph fitted with a flame ionization detector (FID) and nitrogen as the carrier gas, operated at a flow rate of 24 mL min^{-1}, a detector sensitivity of 1000×, and a detector temperature of 150 °C.

For $ZnTiO_3$ particle characterization, structural confirmation was performed using the same Panalytical Empyrean XRD instrument, while optical band gap estimation was carried out using a Cary 5000 UV-Vis-NIR spectrophotometer (Agilent Technologies) in diffuse reflectance (DRS) mode. The Cary 5000 instrument was also used for UV-Vis absorption measurements of dye solutions under dark and illuminated conditions. Rheological measurements (viscosity) were performed using an Anton Paar MCR302e rheometer, and Zeta potential measurements of $ZnTiO_3$ suspensions were obtained using a Malvern Zetasizer Nano-ZS dynamic light scattering (DLS) system. Microscopic imaging was performed using a Magnus MSZ-Bi stereo zoom microscope (Olympus Opto).

The refractive index of liquid samples (acetic acid-toluene-water system) was measured using an Atago RX-7000i refractometer.

Transient cooling analysis of pure stearic acid (SA) and SA–PDMS composite membranes was monitored using a temperature data logger (RVL Scientific and Engineering Ltd.) equipped with eight PT-100 channels, recording temperature at 5-second intervals with ±0.1 °C accuracy. Fourier-transform infrared (FTIR) spectra were acquired using a PerkinElmer Spectrum Two spectrometer in ATR mode, covering 450–4000 cm^{-1}. Differential scanning calorimetry (DSC) was performed using a PerkinElmer DSC 4000 instrument, with maximum deviations of ±2% for enthalpy and ±1.5 °C for temperature measurements. DSC sample masses were determined using a semi-analytical balance with ±0.00001 g precision.

2.3 Materials

This section lists the materials used throughout the experimental work, including polymers, precursors, solvents, dye, extraction chemicals, and the phase change material. These materials were employed for PDMS-based structure fabrication, nanoparticle synthesis, membrane preparation, photocatalysis, liquid–liquid extraction, and thermal energy storage studies.

PDMS base elastomer along with cross-linking agent, marketed as Sylgard™ 184 (The Dow Chemical) was supplied by Kevin Electrochem, India. Analytical grade ethanol (absolute, 99.9%) and diisopropylamine (99%) were purchased from Molychem, India.

Silicon oxy-carbide particles to be used in impregnation of the membrane had been prepared by the process of thermal degradation of PDMS sponge, fabricated in our laboratory itself.

Tetra-butyl orthotitanate [$Ti(OC_4H_9)_4$] from SRL, zinc acetate dihydrate [$Zn(CH_3COO)_2.2H_2O$] from Rankem and acetic acid glacial [CH_3COOH] from Molychem were purchased and used without any further purifications to prepare the zinc titanate particles by sol-gel route.

Powder of methylene blue dye [$C_{16}H_{18}ClN_3S$], supplied by Rankem was used to prepare the stock dye solution. Generic food grade silicone tube of dimensions 4 mm ID x 6 mm OD was purchased from Ami Polymer Pvt Ltd. PVC pipes and elbow connectors of 20 mm internal diameter were used to support the CFI assembly to be made from the silicone tube for photocatalysis application.

Toluene and acetic acid, both of analytical grade were obtained from Molychem (India). Distilled water was used as an aqueous medium throughout the experiments. A PVA filament of diameter 2.85 mm, supplied with ultimaker 3D printer was used for creating hollow spiral channel in the PDMS-CFI to be used for separation of acetic acid.

Phase change material, stearic acid (SA) with 95% purity, was purchased from HiMedia Laboratories Pvt. Ltd. and were used without further purification. Tetrahydrofuran (THF, 99.5%) was purchased from SD Fine Chem. Ltd. and used as a solvent to swell the PDMS films.

Chapter 3: Continuous and Enhanced Photocatalytic Degradation of Methylene Blue from Wastewater via a Plasma Treated $ZnTiO_3$-Loaded PDMS-Lined Coiled Flow Inverter

3.1 Abstract*

A coiled flow inverter (CFI) is a helical tubular flow device with periodic flow inversion that generates Dean vortices, enhancing radial mixing and mass transfer during continuous-flow operation. This study presents the fabrication and evaluation of a transparent PDMS-lined CFI reactor impregnated with plasma-treated $ZnTiO_3$ nanoparticles for continuous visible-light photocatalytic degradation of methylene blue (MB). The CFI was prepared by coating a silicone tube with PDMS, swelling the lining, and incorporating $ZnTiO_3$ particles whose aqueous dispersibility was improved through plasma treatment, as confirmed by rheology and DLS/zeta potential measurements. XRD confirmed $ZnTiO_3$ as the major crystalline phase, while SEM–EDX revealed nanoscale particles with plasma-induced surface modification and oxygen-deficient regions. Band-gap analysis showed a reduced optical band gap of 2.77 eV, indicating enhanced visible-light responsiveness. The optical microscopy and SEM–EDX mapping confirmed PDMS lining formation and $ZnTiO_3$ distribution along the inner channel surface.

Photocatalytic experiments were performed using 10 ppm MB solution at 6 different flow rates ranging 0.72–1.92 mL/min under a uniform 25 W white-LED source. Outlet MB concentration was measured by UV–Vis spectroscopy after 30 min steady-state circulation. Identical experiments in a straight tube of equal length enabled performance comparison. Dark adsorption was low (~4.5%), confirming negligible non-photocatalytic removal. Pseudo–first-order rate constants (*$k \pm$ 95% CI half-width)* were $3.69 \pm 2.00 \times 10^{-3}$ min^{-1} for the dark CFI, $10.60 \pm 3.28 \times 10^{-3}$ min^{-1} for the illuminated straight tube, and $24.66 \pm 6.28 \times 10^{-3}$ min^{-1} for the illuminated CFI, demonstrating, more than two-fold enhancement over the straight-tube and five-fold improvement relative to dark operation.

Keywords: Continuous-flow photocatalysis, $ZnTiO_3$-PDMS composite, Coiled flow inverter, Visible light degradation, Methylene blue, Plasma treatment, Water purification.

* This work is published in 'Materials Science and Engineering: B 324 (2026) 119031' https://doi.org/10.1016/j.mseb.2025.119031.

3.2 Coiled Flow Inverter: Concepts, mechanisms, and theoretical background

Curved tubular reactors are widely used for transport intensification because they generate centrifugal-force–driven secondary flows that significantly enhance heat and mass transfer, narrow residence time distribution, and rapid mixing under laminar regimes, a typical geometry of CFI is given in Figure 3.1[82].

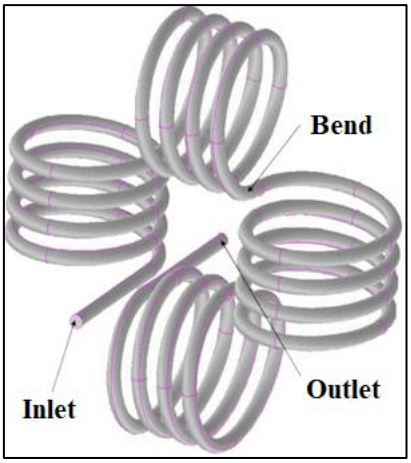

Figure 3.1: CFI geometry

In conventional helical coils, curvature causes the formation of *Dean vortices*, a pair of counter-rotating secondary flows whose strength is governed by the Dean number, expressed as:

$$D_e = R_e \sqrt{\frac{d}{D}} \tag{3.1}$$

where, R_e is Reynolds number (dimensionless), d= inner diameter of the tube (m) and D= coil diameter or radius of curvature of the tube (m).

A higher Dean number corresponds to stronger secondary vortices and enhanced radial convection. However, in conventional coiled tubes, once the flow becomes fully developed, these vortices stabilize and the mixing enhancement plateaus along the reactor length. The CFI overcomes this limitation by introducing *periodic curvature inversion*, where alternating clockwise and anticlockwise coils are connected through sharp 90° or 180° transitions. Each inversion forces a sudden reversal in centrifugal-force direction, destroying the existing Dean vortices and causing the immediate formation of new vortices with opposite rotational symmetry, as shown in figure Figure 3.2[83]. This repetitive

collapse and regeneration prevents complete hydrodynamic stabilization, keeping the flow in a continuously disturbed state resembling mild chaotic advection.

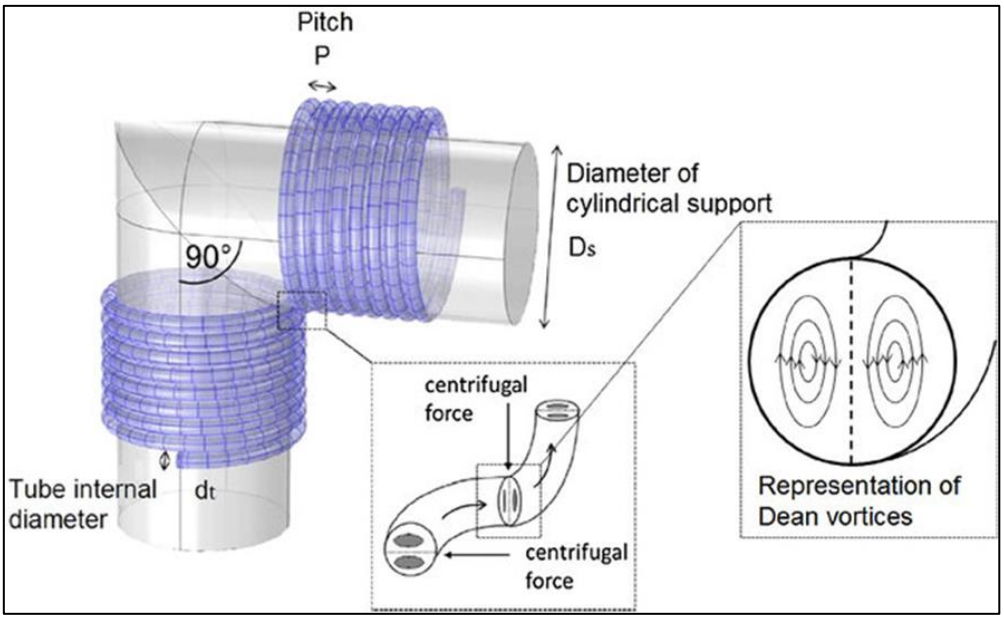

Figure 3.2: Representing various parameters with a 90-degree bend in a CFI.

At every inversion point, the flow experiences stretching, folding, and reorientation of lamellae, which intensifies radial–axial transport and significantly thins the concentration boundary layer. This leads to enhanced cross-sectional mixing, reduced axial dispersion, and a markedly narrower residence time distribution (RTD), resulting in near plug-flow-like behavior even at low Reynolds numbers. Such characteristics are particularly advantageous in photocatalytic processes, where efficient radial mixing exposes fresh reactant fluid to catalyst-coated surfaces and improves photon penetration. For mass-transfer–limited operations, the intensified shear and continuous vortex renewal promote higher interfacial transport rates and improved reaction kinetics without requiring mechanical agitation.

Despite the curvature transitions, the pressure drop across a CFI remains comparable to that in conventional coils, with only minor localized losses due to flow separation at inversion junctions. The gains in mixing efficiency far outweigh these small energy costs. Additionally, because each coil–inverter pair acts as a modular hydrodynamic unit, CFIs can be easily scaled by increasing the number of inversions. Their inherent ability to suppress dead zones, maintain uniform velocity fields, and provide consistent catalyst–fluid interaction makes them a versatile and robust platform for continuous processing in chemical, photocatalytic, and biochemical systems.

Some of the fabricated designs of the PDMS coiled rectors are given in Figure 3.3.

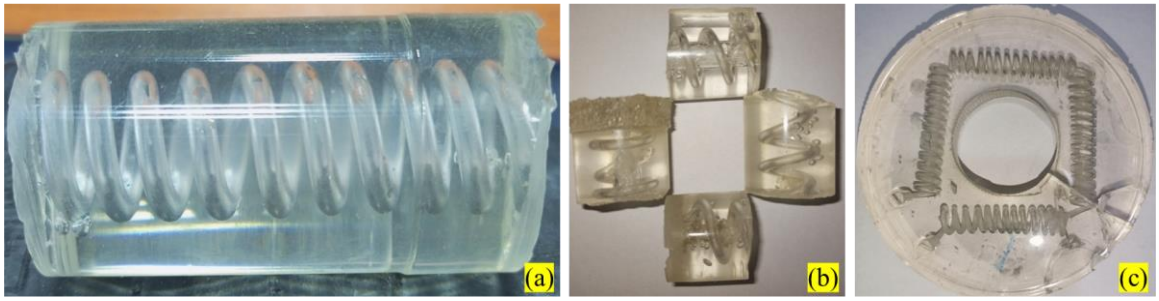

Figure 3.3: Transparent to slightly translucent fabricated PDMS channel reactors (a) The basic helical channel (b) CFI joining 4 monolithic helical channels (c) A monolithic CFI.

The fabricated neat PDMS-based helical and CFI reactors are transparent to slightly translucent, allowing visual observation of the internal coiled channel geometry through the reactor body. The apparent haziness in the figure is mainly due to photographic quality, lighting/reflection, wall thickness variation, and minor surface irregularities from manual fabrication.

3.3 Introduction

Industrial dyes currently in widespread use are typically non-biodegradable and highly toxic, with the textile sector being a major global water consumer[84] and a significant source of organic and chemical contaminants in wastewater including methylene blue (MB), a low molecular weight cationic aromatic dye[85,86]. Although these compounds play a vital role in various human activities, their presence in the environment poses significant ecological risks. These aromatic dyes' inherent breakdown substances have a tendency to accumulate in living organisms, resulting in harmful health consequences for humans[87]. Wastewater discharged from industries, such as, textiles, pesticides, pharmaceuticals, food processing, and leather manufacturing often contains high concentrations of dyes, contributing to the contamination of water bodies and leading to adverse environmental consequences, including the suppression of photosynthesis and the contamination of aquatic organisms[88]. The resulting turbidity from these dyes obstructs sunlight penetration, which in turn impairs the photosynthetic processes essential for sustaining aquatic life. Consequently, the removal of dyes from industrial effluents prior to their release into natural water sources is of critical importance. Numerous treatment technologies have been explored for this purpose, including membrane filtration, coagulation-flocculation, ozonation, ion exchange, photocatalysis, biological and chemical

oxidation, and adsorption. Adsorption, coagulation, membrane filtration, and sedimentation are common methods for remediating organic pollutants, like, MB and its breakdown products[89–92]. Although these methods have demonstrated efficiency, they all have a drawback in that they shift the target pollutant from one medium to another without necessarily eliminating it. Visible light induced photocatalysis is particularly regarded as a highly efficient and environmentally friendly approach due to its ability to completely degrade organic pollutants, its potential for solar-driven operation, minimal generation of secondary waste, and its applicability under mild conditions. Additionally, photocatalysis offers long-term cost-effectiveness and reusability of catalysts, making it a promising technology for sustainable wastewater treatment and driven by light-activated materials, has emerged as a powerful technique for environmental remediation, energy conversion, and chemical synthesis[93].

The process intensification (PI) approach, which relies on ingenuity in developing solutions that aim to enhance the efficiency of a process by improving yield, speed, spatial requirement, or energy consumption, can be successfully applied to photocatalysis. In reaction engineering, one of the PI approaches focuses on achieving enhanced mixing, mass transfer, and reaction efficiency while reducing reactor volume and energy consumption. The CFI is an effective PI tool that promotes rapid tracer mixing and narrow residence time distributions by periodically inverting fluid flow within helical coils. Such flow topology drastically enhances radial mixing and minimizes axial dispersion, making CFIs highly suitable for continuous processing with improved conversion efficiency and lower energy requirements[94,95]. A CFI occupies space of much less linear dimension with its flow field having a much higher residence time than its straight tube counterpart[96–98].

In the context of photocatalytic degradation of organic pollutants, CFIs have been deployed to continuous-flow reactors where catalyst particles (e.g., TiO_2, ZnO) are suspended on channel walls and stimulate activation reactions at higher flow rates. These configurations have demonstrated significantly improved degradation kinetics often several fold faster than batch systems due to the combination of hydrodynamic enhancement and efficient light irradiation[99]. It has been reported nearly 99% degradation of paracetamol in 36 min using a CFI with Co–Ni tungstate on g-C_3N_4 under visible-light irradiation, achieving a reaction rate 2.7 times faster than a conventional batch reactor[100]. Besides enhanced pollutant degradation, CFI and coiled reactors have been applied to diverse photocatalytic

processes, including hydrogen evolution, organic synthesis etc., while employed with some other suitable photocatalysts[101–104].

Among the various photocatalysts, $ZnTiO_3$ nanoparticles exhibit significant advantage due to their bandgap aligning with the visible light so that solar radiation energy can be harnessed for environmental pollutant degradation[105]. These oxides are also chemically stable, exhibit multiple phases offering structural and electronic tunability, and inexpensive and easy to prepare. These particles have been successfully utilized for photocatalytic dye degradation reactions[106–108]. However, since these oxides are difficult to disperse in water, their aqueous dispersion often needs to be vigorously stirred while in use for photocatalysis. Poor dispersibility that necessitates stirring limits their use to a batch mode only and makes them not suitable for use in a continuous reactor. Integrating these photo-active particles with tubular continuous reactors is a viable approach for their efficient utilization.

This study reports the first-ever fabrication of a CFI reactor with $ZnTiO_3$ particles directly embedded into the inner PDMS-lined wall of a silicone tube. Although ZTO is a stable, visible-light-responsive oxide with a suitable bandgap, it has not previously been integrated directly within reactor geometries for continuous photocatalysis. Our novel process-intensified design enables uniform light penetration, stable catalyst immobilization, and minimal particle loss. Applied to the visible-light-driven degradation of MB in water, the ZTO-impregnated CFI demonstrates efficient radical generation, superior mass transfer, and enhanced degradation efficiency validating its potential for scalable wastewater treatment applications.

The zinc titanate particles are infused inside the CFI surface by first coating the surface with PDMS film, swelling the PDMS film with THF, and subsequently exposing the swollen film to a stable aqueous dispersion of the particles. The particles, otherwise not dispersible in water, are made compatible with water by exposing them to nitrogen plasma prior to making a dispersion. The particles in dispersion are infused inside the swollen PDMS film due to osmotic forces and affinity of THF for water, and remain immobilized after the films are de-swelled. Along the similar idea of exposing the swollen surface of PDMS to aqueous solution of a metal oxide has been used for coating of metal oxide inside the PDMS microchannel[109].

Integrating $ZnTiO_3$ into PDMS millifluidics creates an efficient platform that merges precise flow control with enhanced photocatalytic performance for light-driven reactions. Setting behavior of PDMS helps in immobilizing the photocatalytic particles, its transparency allows the visible light to sensitize these particles. Use of CFI affords a continuous mitigation process of dyed wastewater which can be easily scaled up. PDMS lined CFI provides a robust and versatile platform with intricate flow patterns, enabling efficient mixing, and enhanced mass transfer, and precise control over reaction conditions[110,111]. By impregnating $ZnTiO_3$ particles into the inner channel of silicone tube CFI, a high surface area-to-volume ratio is achieved, maximizing the exposure of the photocatalyst to incident light and facilitating efficient utilization of generated reactive species, while the PDMS material ensures flexibility and compatibility with various solvents[112–117].

These reactive species, including hydroxyl radicals and superoxide ions, react with MB dye molecules, leading to their degradation into non-toxic byproducts, such as, water and carbon dioxide[49,118,119]. The use of CFI enhances the photocatalytic efficiency by providing a large surface area for catalyst deposition and promoting uniform flow distribution, thereby maximizing the exposure of MB dye to the photocatalyst[120–122].

3.4 Research gaps

Photocatalytic degradation is widely investigated for dye-contaminated wastewater treatment, and immobilized photocatalytic films are also recognized for evaluating photocatalytic activity, including methylene blue degradation tests. However, translating photocatalysis into compact continuous-flow reactors still requires improved integration of catalyst immobilization, light accessibility, and flow-induced mass transfer enhancement.

The important research gaps are:

- Conventional photocatalytic systems are largely batch/slurry-based, which limits continuous processing and creates catalyst recovery challenges.
- PDMS-based continuous photoreactors for methylene blue degradation remain insufficiently explored.
- Immobilized photocatalysts in compact millifluidic systems for continuous wastewater treatment are still limited.

- Nanoparticle dispersion and aggregation issues can reduce photocatalytic efficiency and catalyst accessibility.
- Compact reactor designs integrating light penetration, catalyst immobilization, and hydrodynamic mixing within a single platform are limited.

This chapter addresses these gaps by developing a transparent PDMS-lined CFI reactor with immobilized plasma-treated $ZnTiO_3$ particles and evaluating its continuous visible-light photocatalytic performance for methylene blue degradation.

3.5 Experimental section

3.5.1 Synthesis of $ZnTiO_3$ particles and preparation of its plasma treated suspension/dispersion

Bulk $ZnTiO_3$ particles were synthesized via the sol–gel method, involving precursor mixing, gelation, drying, and high-temperature calcination[105,123,124]. A schematic representation of the synthesis process of $ZnTiO_3$ particles is shown in Figure 3.4. Zinc acetate dihydrate (2.25 g) was dissolved in acetic acid (6.66 mL) under mild stirring at room temperature for 30 min. Subsequently, tetra-butyl orthotitanate (3.40 mL) was added with continuous mixing, yielding a viscous, homogeneous white solution.

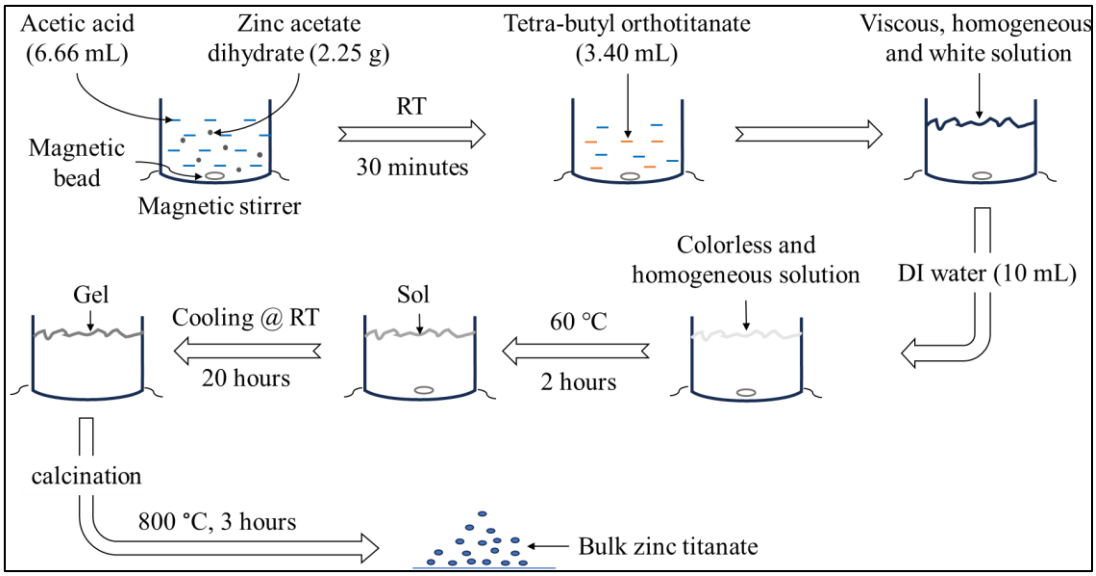

Figure 3.4: A schematic flow chart of zinc titanate synthesis by sol-gel method.

Addition of deionized water (10 mL) produced a colorless, uniform mixture, which was then heated to 60 °C and stirred for 2 h. The resultant sol was aged at room temperature for

20 h to form a gel, which was calcined in an air muffle furnace at 800 °C for 3 h. The calcined material was ground with a mortar and pestle to obtain fine, white $ZnTiO_3$ powder.

A uniform and better homogeneous suspension of ZTO in DI-water was obtained by pre-treating the ZTO powders to a nitrogen plasma inside a custom designed plasma treatment set-up that enabled exposing the plasma-treated particles to water without bringing them into contact with atmosphere. 100 mg of $ZnTiO_3$ particles was given plasma treatment using nitrogen gas, maintained at vacuum $6.1x10^{-1}$ Torr for 20 minutes inside the plasma treatment set up fabricated by Excel Instruments, Mumbai, India. After the treatment, 100 mL of DI water was introduced inside the plasma chamber without exposing the sample to atmospheric oxygen, preparing a 100 mL of plasma treated $ZnTiO_3$ particles suspension solution with concentration of 1 mg/mL. A schematic diagram of the plasma treatment setup is shown in Figure 3.5.

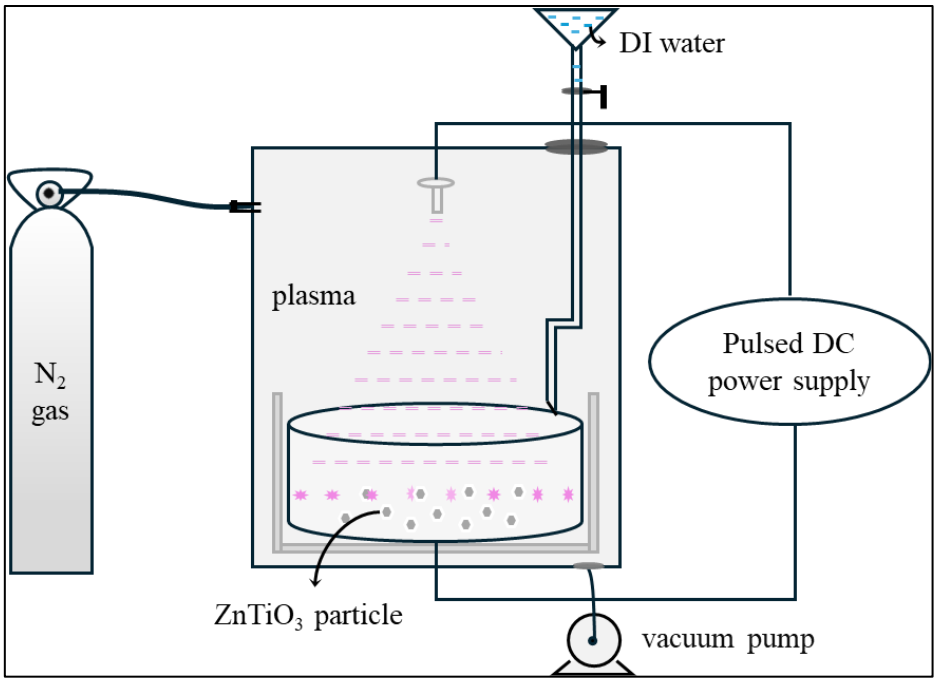

Figure 3.5: A simple diagram representing the preparation process of stable and uniform $ZnTiO_3$ particle dispersion using nitrogen plasma setup.

3.5.2 Fabrication of coiled flow inverter reactor

A schematic representation of the method of CFI fabrication along with the actual image of CFI is shown in Figure 3.6 (a) and (b) respectively. Initially, a square base with PVC pipe of 20 mm external diameter and length of 62 mm was constructed. The four sides were connected using right angled elbow connectors in such a way that 42 mm pipe is visible between the two connectors. A silicone tube of 118 cm long with 4 mm and 6 mm as inner

and outer diameter respectively was wound over this square base. A CFI with total of 12 turns was formed with a pitch of 10 mm, and 90° bend at cross-section of each elbow connector.

To line the tube with PDMS film, a well-mixed mixture of PDMS polymer (Sylgard 184) and cross-linker (10 wt% of base elastomer) was injected inside the tube of CFI and sealed for 3 hours at room temperature in order to effect proper bonding between the silicone tube and the PDMS mixture. Thereafter nitrogen gas was blown into the tube at 0.2 bar of gauge pressure continuously for 3 hours from one side of the CFI expelling the bulk mixture from the tube and leaving a thin PDMS film behind on the wall of the CFI. Subsequently, PDMS film on the CFI wall was cured in a microwave oven operating at 180 W for 15 minutes.

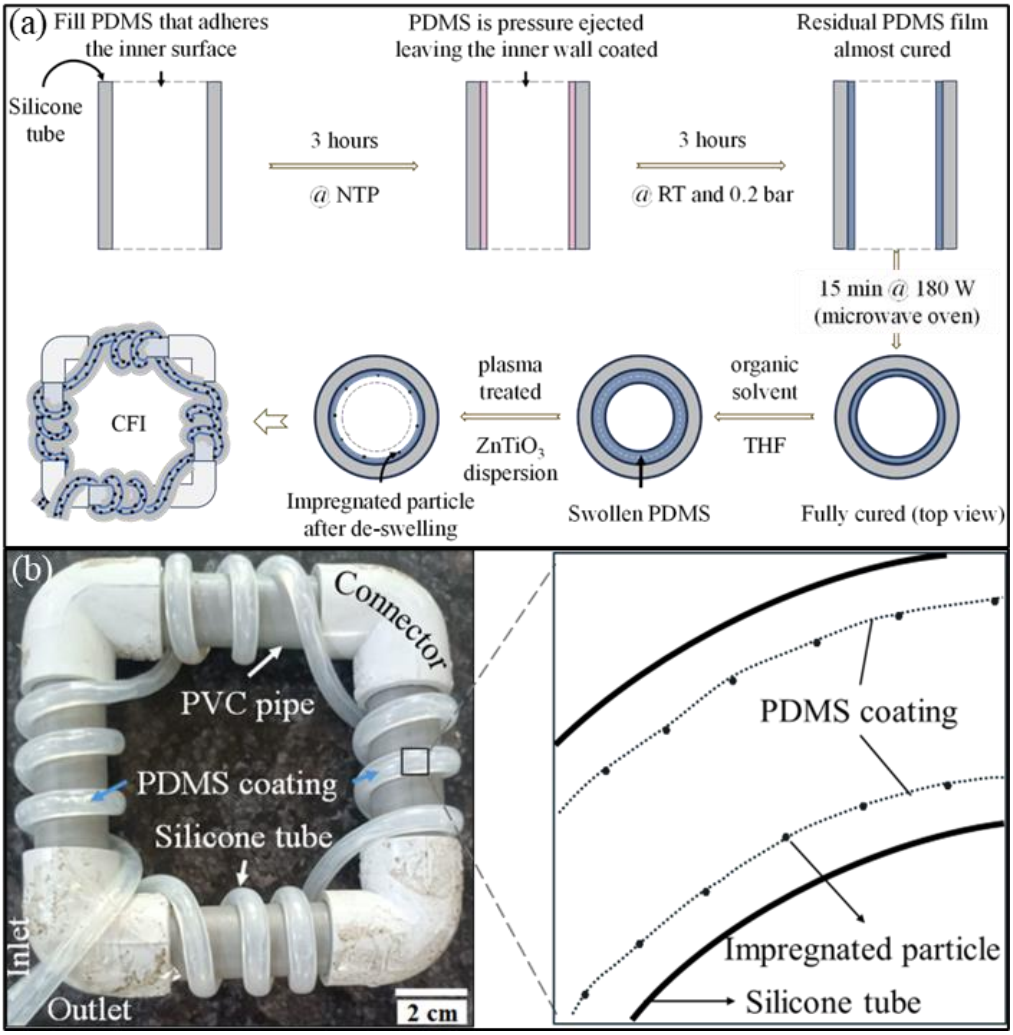

Figure 3.6: (a) Schematic of the process employed for lining the tube with zinc titanate particles. (b) Actual image of CFI with a cartoon depicting the tube lining.

By measurement it was found that with the remaining 8.2 ml of the PDMS coating in the inner tube surface reduced internal diameter of CFI from 4 mm to ~ 2.66 mm, which

resulted in around 0.67 mm thick line coating of PDMS material to the silicone tube surface of CFI. However, non-uniformity of the thickness of the lining along the tube length cannot be ruled out in this procedure.

Non-uniform PDMS thickness observed along the reactor channel and presented later (in section 3.6.2.1), primarily originates from gravitational drainage and surface tension gradients during static curing. Such variation can slightly influence local flow resistance and light transmission, potentially causing minor deviations in residence time or photocatalytic exposure. However, within the operating flow rates and light intensities employed in this study, these effects were negligible, as evidenced by the consistent degradation performance and reproducibility observed across repeated trials. Moreover, PDMS's inherent elasticity and optical transparency contribute to stable performance over extended operation despite minor geometric variations. For large-scale or long-duration applications, enhanced uniformity can be achieved through rotational curing or controlled viscosity-assisted casting techniques, which minimize film thickness deviation and improve scalability of the fabrication process[125]. To achieve particle infusion inside the PDMS lining, first the film was swelled by filling the CFI channel with tetrahydrofuran (THF) solvent and sealing for 2 hours. This caused widening of the pores of the PDMS coating throughout the silicon tube channel. Subsequently, after removing THF from the channel, the prepared plasma-treated $ZnTiO_3$ suspension was manually injected from the inlet side using a syringe while maintaining an approximately constant flow rate. The channel was filled within about 20 s and sealed for 2 h to allow interaction between the suspension and the THF-swollen PDMS lining. Upon contact with the aqueous suspension, the swollen PDMS gradually started deswelling, during which the dispersed $ZnTiO_3$ particles became trapped mainly within the surface/subsurface region of the PDMS lining, resulting in particle impregnation. A slight decrease in particle loading from inlet to outlet may occur due to progressive deswelling; however, the short filling time and nearly constant injection rate minimized this variation. Therefore, the particle incorporation is considered reasonably uniform along the active inner surface, although minor nanoscale heterogeneity may still exist.

3.5.3 Photocatalysis Set-up and sampling procedure

Continuous photocatalysis experiment was performed with the set up shown in Figure 3.7. Initially a 2 L stock solution of 10 ppm concentration of MB dye is prepared. This MB dye

contaminated solution is passed through the particle impregnated CFI with and without white light irradiation at flow rates of 0.72, 0.96, 1.20, 1.44, 1.68 and 1.92 mL min^{-1}. The flow rate was controlled by a peristaltic pump attached to the inlet of CFI.

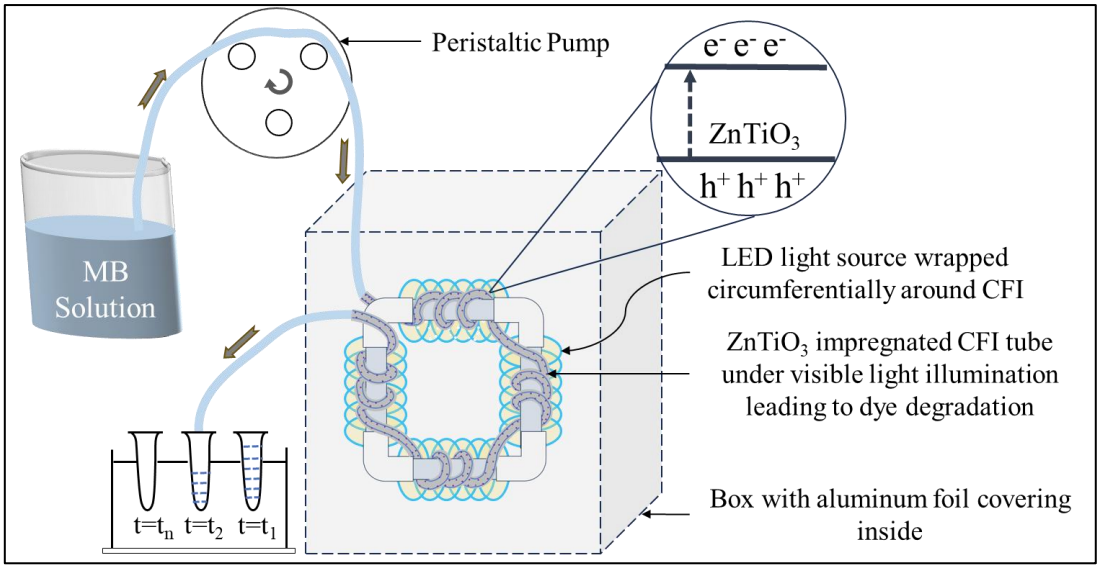

Figure 3.7: Schematic of the photocatalysis monitoring setup used for continuous dye degradation.

A 25 W white LED strip with medium density of 60 LEDs per meter, operated using a 12 V DC supply, was wrapped circumferentially over the CFI to illuminate the reactor from all directions during photocatalytic dye degradation under white-light irradiation. To maintain uniform illumination around the CFI and minimize the influence of external light sources, the reactor assembly was placed inside an aluminium-covered box.

Before sampling, the MB solution was passed for 30 minutes at all flow rates to achieve a steady state condition at that flow rate. Thereafter multiple samples were collected at small intervals and their concentrations were averaged to obtain the steady state concentration at the outlet of the reactor.

Same procedure was repeated under the identical conditions with the coiled tube now used as a straight tube reactor with the same length (instead of a CFI) in presence of light so that the effectiveness of CFI could be confirmed by comparing the dye concentrations at the outlet. The samples were analyzed using UV-Visible characterization.

3.6 Results and discussion

3.6.1 Characterization and analysis of $ZnTiO_3$ particles used to impregnate CFI

3.6.1.1 Structural characterization

The assigned diffraction peaks in bulk zinc titanate (BZT) particles at diffraction angles (2θ) values of 24.15, 27.69, 30.07, 32.01, 33.02, 35.39, 36.48, 40.7, 42.92, 49.19, 53.64, 56.66, 62.03, and 63.64° correspond to the planes (012), (110), (220), (100), (104), (110), (222), (113), (021), (024), (116), (110), (214) and (300) respectively, with rhombohedral $ZnTiO_3$ as the majority phase and some residual impurities, such as, Zn_2TiO_4, rutile TiO_2 and ZnO, are shown in Figure 3.8. The plasma treatment of these particles did not lead to any alteration in the XRD pattern.

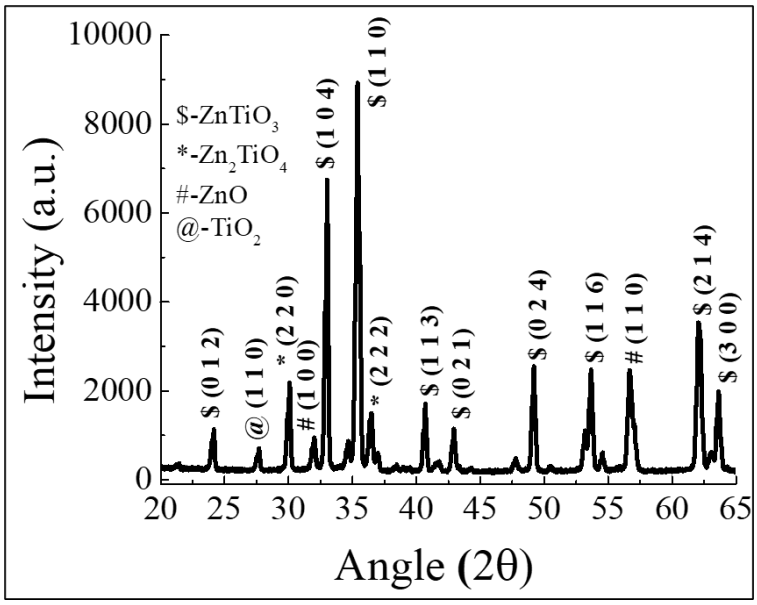

Figure 3.8: XRD pattern of bulk zinc titanate prepared by sol-gel route.

The indexed peaks in JCPDS card number 00–025-0671 referring to rhombohedral $ZnTiO_3$ crystal system, match the majority of the allotted peaks with an average angle shift of 0.29°. 1 peak at 27.69° can be indexed to (110) plane of the impurity phase of rutile TiO_2, as confirmed from the JCPDS card number 01–086-0147. The remaining of the 4 peaks of which, 2 peaks at diffraction angles of 30.07 and 36.48° indexed at (220) and (222) planes respectively may be attributed to cubic phase of Zn_2TiO_4 impurity (JCPDS card 01-073-0578) and the other 2 peaks at diffraction angles of 32.01 and 56.66° indexed at (100) and (110) planes respectively might be raised due to the hexagonal phase of ZnO impurity (JCPDS card 01-080-0075). The lattice parameters, crystallite size, micro-strain, and dislocation density for the rhombohedral $ZnTiO_3$ from above XRD image, have been

summarized in Table 3.1. The crystallite size (D) was estimated using the Scherrer equation $D_{hkl} = k\lambda/(\beta\cos\theta)$, where $k = 0.94$, $\lambda = 1.5406$Å, and β is the FWHM. The micro-strain (ε) and dislocation density (δ) were calculated as $\varepsilon = \beta/4\tan\theta$ and $\delta = 1/D^2$.

Table 3.1: Structural properties obtained from XRD image

Rhombohedral $ZnTiO_3$: $a = b = 0.45$ nm, $c = 1.3$ nm				
2θ (°)	β (°)	D (nm)	δ ($\times 10^{-3}$ nm^{-2})	ε ($\times 10^{-3}$)
24.15	0.2856	29.7003	1.133	5.827
33.02	0.2903	29.8060	1.125	4.274
35.39	0.382	22.7459	1.932	5.236
40.7	0.2714	32.5980	0.941	3.193
42.92	0.2679	33.2740	0.903	2.974
49.19	0.2996	30.4561	1.078	2.856
53.64	0.3704	25.1006	1.587	3.196
62.03	0.4042	23.9499	1.743	2.933
63.64	0.3363	29.0338	1.186	2.365

Average $D = 28.5$ nm; $\varepsilon = 3.9 \times 10^{-3}$; $\delta = 1.3 \times 10^{-3}$ nm^{-2}.

The average crystallite size (~29 nm) and low micro-strain indicate well-crystallized particles with minimal lattice defects. These values are comparable to chemically derived oxide nanoparticles reported in the literature, where sol-gel or wet-chemical methods typically yield crystallite sizes in the 25–35 nm range with strain values of 3–5 × 10^{-3}. The lower dislocation density suggests fewer structural defects and enhanced crystallinity, consistent with high-quality oxide nanomaterials synthesized via controlled chemical routes [126–132]. The obtained structural parameters ($a = b = 0.45$ nm; $c = 1.30$ nm) confirm the formation of rhombohedral $ZnTiO_3$, aligning well with previous report [133].

3.6.1.2 Rheology and surface charge characterization of $ZnTiO_3$ particles dispersion

The effect of plasma treatment on the particle suspension can be seen from the viscosity vs time curves as shown in Figure 3.9 (a). It is clearly noticed from the Figure that plasma treated zinc titanate suspension resulted in a higher viscosity as compared to that without plasma treatment whose viscosity is nearly equal to that of DI water. This behaviour can

be explained by the attachment of hydrophilic OH radicals to $ZnTiO_3$ particles by the plasma treatment and further increasing the suspension stability in DI water. As water interacts with the plasma-treated particles, the hydrophilic groups facilitate the formation of a hydration layer around each particle, which enhances stability and prevents aggregation. Additionally, the surface charges introduced during plasma treatment can lead to electrostatic repulsion between particles, further promoting a uniform and stable suspension.

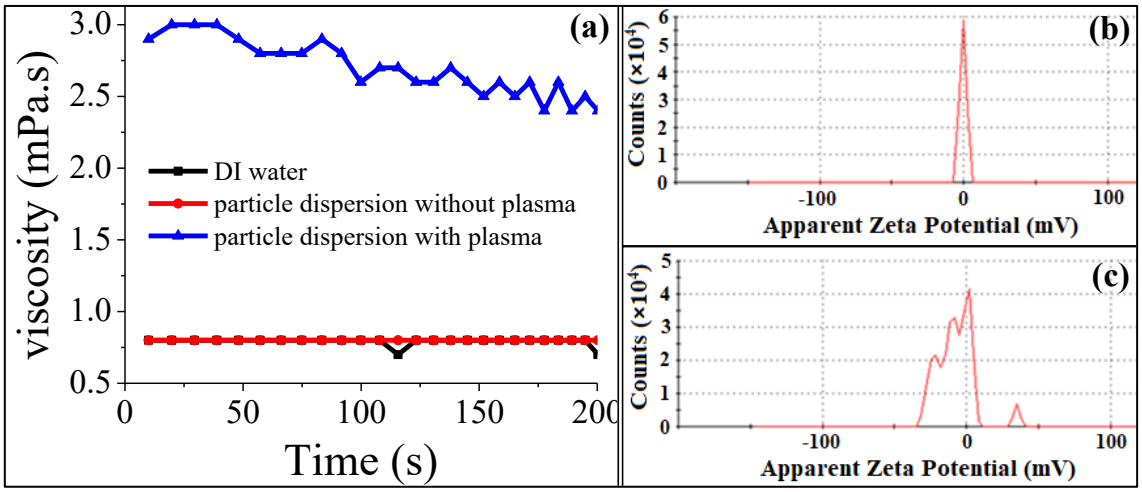

Figure 3.9 (a) Viscosity comparison of suspensions prepared using untreated and plasma treated particles; (b) and (c) Zeta potential measurements respectively of untreated and plasma-treated particles.

The surface charge that stabilizes the suspension can be measured by zeta potential measurements, and the data is presented in Figure 3.9 (b) and (c), comparing the concentration of particle suspension without plasma and with plasma treatment. In graph (b) (without plasma treatment), the zeta potential distribution is narrow and centered close to 0, indicating that the particles have minimal surface charge. This lack of significant surface charge suggests weak electrostatic repulsion between particles, making the suspension prone to aggregation and instability. Such a suspension is likely to settle over time due to insufficient repulsive forces to counteract van der Waals attractions.

In contrast, graph (c) (with plasma treatment) shows a broader and more asymmetric zeta potential distribution, with a shift towards more negative or positive values, depending on the surface modifications introduced by the plasma treatment. This change indicates that the plasma process has altered the surface properties of the particles, likely by introducing functional groups or charges that enhance particle interaction with the medium. The increased magnitude of the zeta potential, either positive or negative, implies stronger

electrostatic repulsion between particles, contributing to improved colloidal stability and a more uniform suspension.

This comparison shows the favourable effect of plasma treatment in enhancing the stability of particles suspension.

3.6.1.3 Band gap measurement

Analyzing the synthesized $ZnTiO_3$ particles for band gap is an important aspect in order to ensure the suitability of the particles for photocatalysis process. The plasma treated particles have been characterized by DRS from which Tauc plot is obtained and shown in Figure 3.10 (a). It is clear from the Figure that there is a sharp increase in absorption beyond 2.77 eV, indicating a transition from the valence band to the conduction band. This optical band gap of 2.77 eV corresponds to photon absorption of wavelengths around 448 nm, suggesting the plasma treated $ZnTiO_3$ particles suitable for photocatalytic activity into the visible light spectrum.

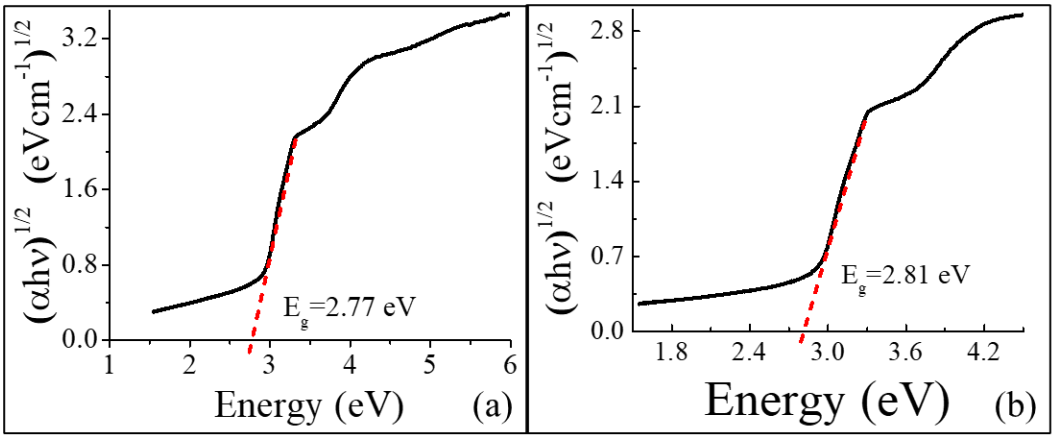

Figure 3.10: Tauc plot for band gap estimation of the $ZnTiO_3$ particles (a) after plasma treatment and (b) before plasma treatment.

It is to be noted that untreated particles exhibited a bandgap of 2.81 eV as seen from Figure 3.10 (b). The slight reduction in the bandgap, which aids in photosensitization under visible light illumination, can be attributed to oxygen vacancies induced by the plasma treatment.

3.6.1.4 EDX and SEM characterization

Figure 3.11 (a), (b), (c) and (d) consists of two panels: In the left panel, (c) shows an area EDX elemental mapping of $ZnTiO_3$ particles corresponding to the SEM image, (a). The right panel compares the SEM images between particles without plasma (b) and with plasma treatment (d) at 200 nm scalebar. The EDX analysis highlights the distribution and relative concentrations of oxygen (O), zinc (Zn), and titanium (Ti) within the selected area.

In the EDX mapping, green represents oxygen (O), purple represents zinc (Zn), and red corresponds to titanium (Ti). The selected area shows a composition of 55% zinc, 31% titanium and 14% oxygen. The observed elemental percentages indicate a significant oxygen deficiency suggesting presence of oxygen defects.

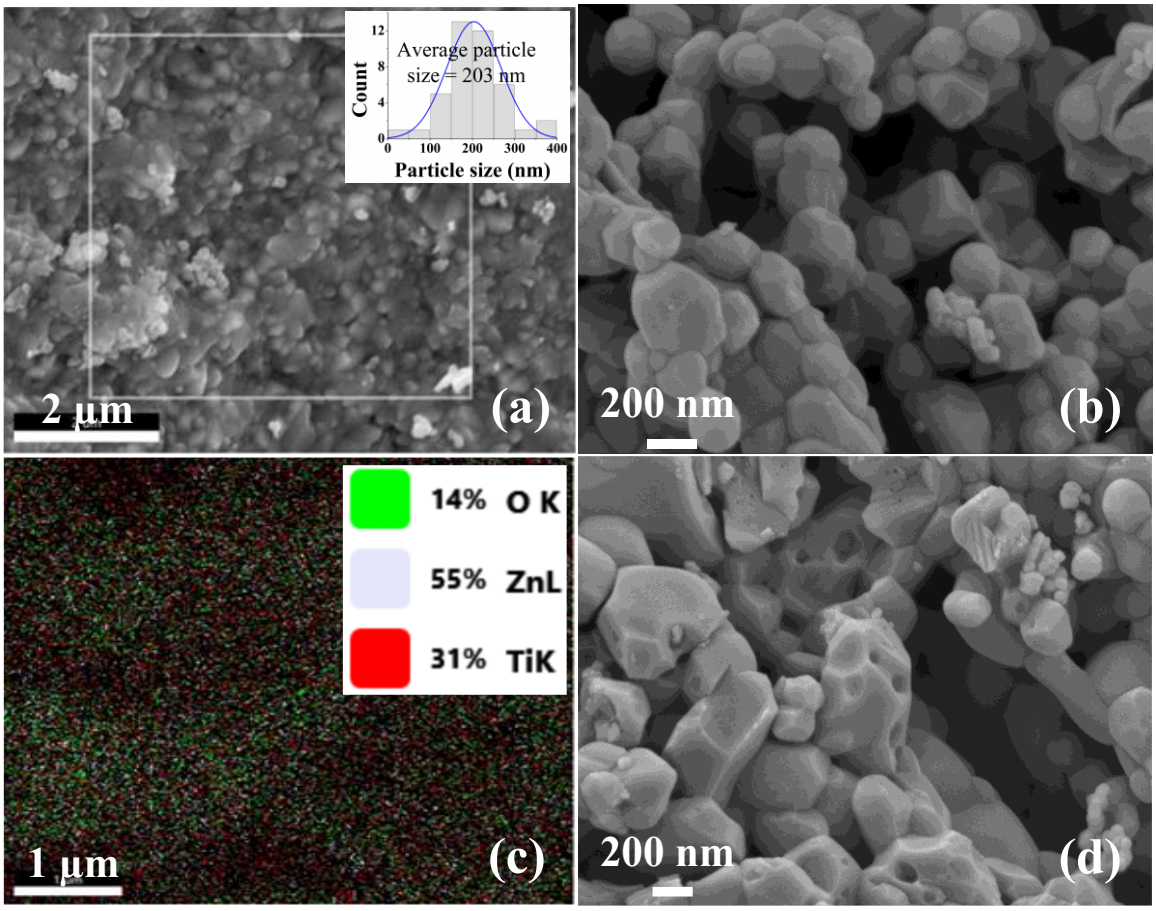

Figure 3.11: (a) and (b) SEM images of the untreated particles at two different magnifications. (c) EDX elemental mapping of the particles. (d) SEM image of the plasma-treated particles.

The inset in image (a) is a histogram showing particle size distribution, with an average particle size of 203 nm. SEM images (b) and (d) correspond respectively to the untreated and treated $ZnTiO_3$ particles. It is evident from these images that the treated particles show increased surface roughness and, in some areas, the presence of micro voids or pits. These features suggest that plasma treatment introduced surface etching or activated defect sites, which can enhance the reactivity of the material and improve its dispersion due to increased surface area.

3.6.2 Particle impregnation of CFI

3.6.2.1 Imaging of cross-section of tube and CFI

PDMS coating and particle impregnation inside the tube are seen through the optical images under a microscope as shown in Figure 3.12 (b) and (c) over the native tube (a). The PDMS coating is not uniform. However, the particles have been impregnated thoroughly in the circular path. Accordingly, the thickness of the PDMS varies around 1.1 mm to 0.1 mm throughout the inner periphery of the tube. The experiments to control the uniformity of the PDMS coating are under way. Here, it is demonstrated that even without a uniform PDMS coating, the CFI can be infused with the particles inside which can enhance the photocatalytic reaction kinetics.

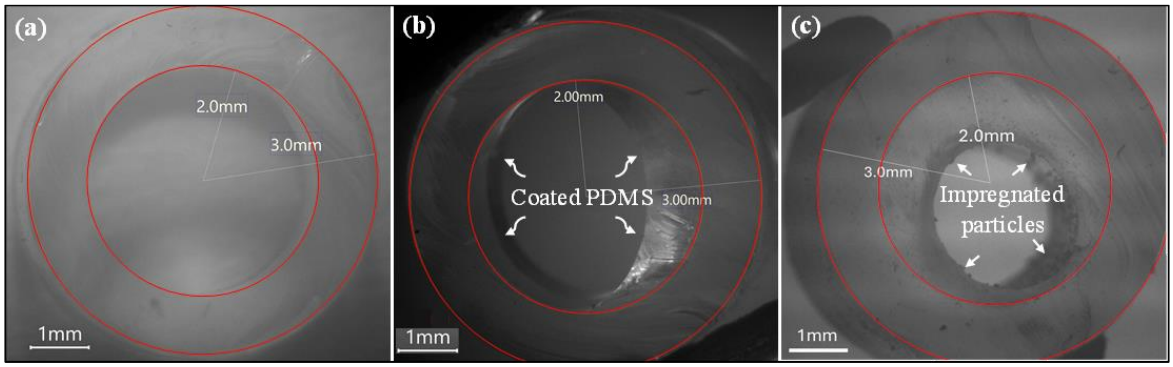

Figure 3.12: Optical microscopic images of (a) native, (b) PDMS coated and (c) particle impregnated tube.

Since the microscopic analysis was performed on selected sections, very small local uncoated regions or coating-thickness variations cannot be completely ruled out. However, the visible particle impregnation along the inner channel and the successful photocatalytic performance suggest that major uncoated regions were unlikely.

3.6.2.2 SEM and EDX imaging of inner surface of CFI

The SEM and EDX mapping images reveal the elemental distribution of zinc and titanium across the cross-section of the CFI channel impregnated with zinc titanate particles in Figure 3.13. The SEM image (a) shows the physical morphology of the cross-section, while the accompanying elemental maps highlight the spatial presence of various elements, including Zn, Ti, and others, like, oxygen (O), carbon (C), and silicon (Si) from the substrate.

The TiK (orange) and ZnK (cyan) maps clearly show the localized distribution of titanium and zinc, respectively, suggesting that zinc titanate particles are dispersed across the surface

and impregnated within the channel. The co-localization of Ti and Zn indicates the presence of $ZnTiO_3$ in the impregnated CFI. The uniformity of these maps suggests good distribution of zinc titanate particles within the matrix, which is crucial for maintaining catalytic or functional properties of photocatalyst. Homogeneity in the areal coverage of particles along the channel walls can be taken to imply the quality of uniformity, with minimal aggregation or gaps, ensuring effective utilization of active sites and preventing channeling. High-resolution SEM images were captured at multiple locations along the inner walls ($n \geq 5$), which showed consistent particle coverage across different regions. This observation confirms that the particle distribution is sufficiently uniform to maintain consistent performance and minimize efficiency losses due to preferential flow paths. The oxygen (O) distribution further supports the presence of the titanate phase. This mapping confirms the successful incorporation of $ZnTiO_3$ into the CFI channel.

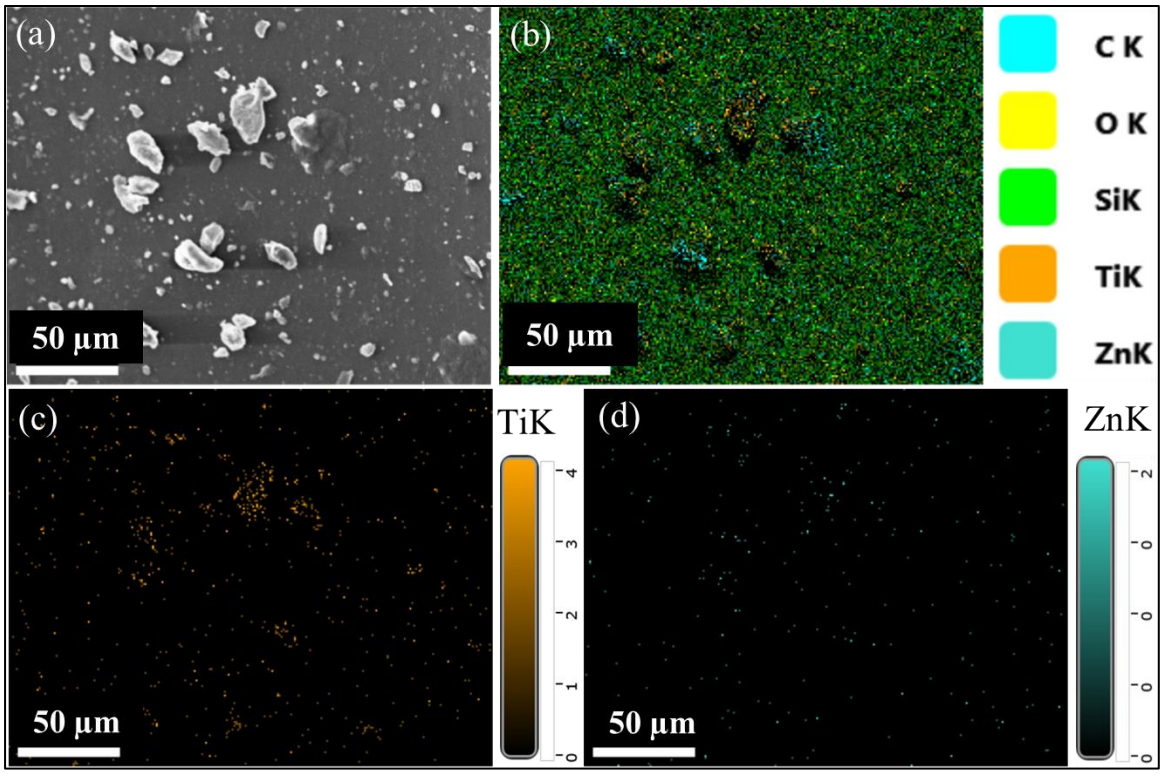

Figure 3.13: SEM and EDX mapping for zinc titanate particles distribution at the cross-section of CFI.

In order to estimate the area fraction of particles inside CFI, the area ($235.02 \times 165.84\ \mu m^2$) of the image (a) has been analyzed on imageJ software. The identified 136 spots of $ZnTiO_3$ particles having total area 4077 μm^2 out of the given area 38,975.7 μm^2 brings an area fraction of 0.105 impregnation inside PDMS matrix. This distribution of the particles is considered along the whole inner curved surface area 98.55 cm^2 of the tube, leading to the

estimated surface area of particles exposed to the MB solution as 10.34 cm^2. As discussed in the next section, the estimated exposed surface area is utilized for normalizing the rate constant on area basis to obtain a suitable quantifier of the efficacy of the catalytic activity and comparing it to other works.

3.6.3 Photocatalysis

In kinetic studies of wastewater treatment, dye degradation is commonly described using linear or non-linear relations that express the decrease in dye concentration with reaction time. For many photocatalytic systems, the degradation behavior is approximated by the pseudo-first-order rate law, $Ln(C_o/C) = kt$, where C_o is the initial dye concentration, C is the dye concentration after reaction time t, and k is the pseudo-first-order rate constant.

In contrast to a batch reactor, the current study involves a continuous-flow photocatalytic reactor, where the relevant reaction time is represented by the residence time of the dye solution inside the reactor. The residence time is given by: $\tau = V/Q$, where V is the fixed reactor volume (6.6 mL) and Q is the volumetric flow rate. During each experimental run, the flow rate was maintained constant until steady-state operation was achieved. At each flow rate, four outlet samples were collected after reaching steady state and averaged to obtain a single steady-state outlet concentration, C_{ss}. Therefore, the concentration used in the kinetic expression corresponds to C_{ss}, rather than a time-dependent concentration.

Accordingly, the pseudo-first-order relation for the continuous-flow reactor can be expressed as:

$$Ln\left(\frac{C_o}{C_{ss}}\right) = k\left(\frac{V}{Q}\right) \tag{3.2}$$

where C_0 is the inlet dye concentration, C_{ss} is the steady-state outlet dye concentration, V is the reactor volume, Q is the imposed flow rate, and k is the pseudo-first-order rate constant. Here, V/Q changes only when the flow rate is varied between different experimental runs and not during a single steady-state run.

In the photocatalysis experiments, the degradation activity of the $ZnTiO_3$-impregnated CFI and straight tube was analyzed under visible-light and dark conditions at six different flow rates. The corresponding $Ln(C_0/C_{ss})$ values were plotted against $1/Q$ in Figure 3.14, and the data were fitted using the pseudo-first-order kinetic model with ±95% confidence intervals.

Linear regression of $Ln(C_0/C_{ss})$ versus $1/Q$ was performed through the origin software, and the standard error of the slope was calculated from the residuals. The 95% CIs were obtained using the Student's t-distribution ($t_{0.975,6} = 2.447$), corresponding to a two-tailed confidence level with $df = 6$ [134]. The corresponding confidence limits for the rate constant were obtained by dividing the slope limits by the reactor volume (6.6 mL). Error bars in Fig. 3.14 represent the variability among four steady-state outlet samples collected at each flow rate and the reported confidence limits reflect the uncertainty in the fitted parameters.

The linear regression model used is $y = mx$, with the slope calculated as:

$$m = \frac{\sum x_i y_i}{\sum x_i^2}$$

The standard error of the slope is given by:

$$SE(m) = \sqrt{\frac{\sum (y_i - mx_i)^2}{(n-1)\sum x_i^2}}$$

The margin of error is found as:

$$\Delta m = t_{0.975,\, n-1} \cdot SE(m)$$

The 95% confidence interval is calculated as:

$$95\%\, CI = m \pm \Delta m$$

The rate constant and its confidence limits are obtained as:

$$k = \frac{m}{6.6}, CI(k) = \frac{CI(m)}{6.6}$$

Using the experimental data and assuming a zero-intercept fit as shown in Fig. 3.14, the approximated parameters are given in table 3.2.

Table 3.2: Calculated error parameters for slope and rate constant calculation.

Condition	m	SE (m)	Δm	k (×10⁻³ min⁻¹)	Δk (×10⁻³ min⁻¹)
Dark (CFI)	0.02433	0.00541	0.01323	3.69	2.00
Light (St Tube)	0.06995	0.00883	0.02162	10.60	3.28
Light (CFI)	0.16277	0.01693	0.04142	24.66	6.28

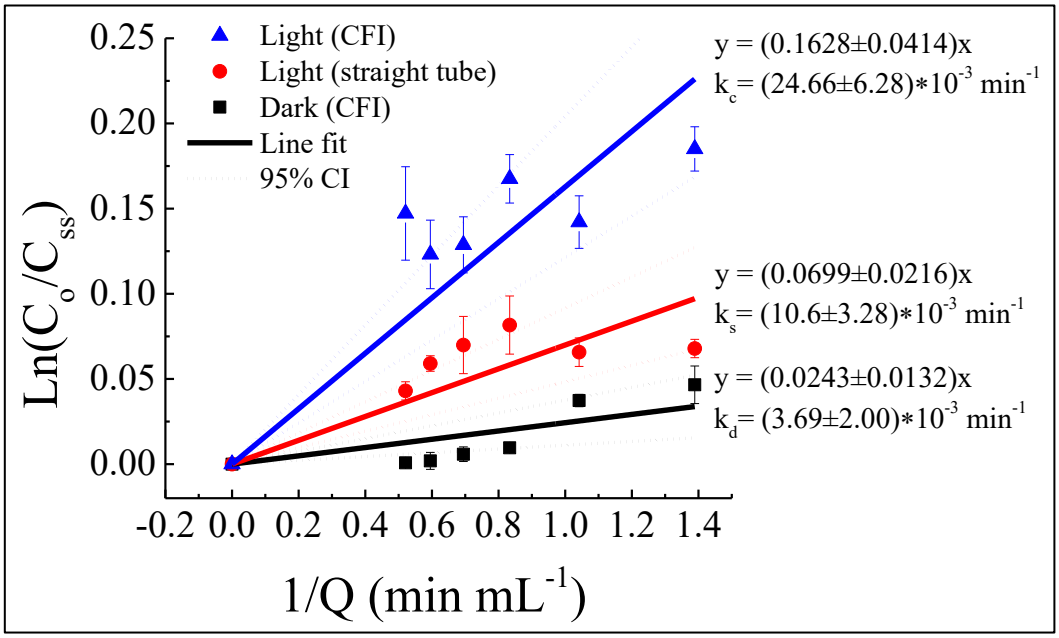

Figure 3.14: Pseudo-first-order kinetic plots of methylene blue degradation showing variation of $Ln(C_0/C_{ss})$ with inverse flow rate $(1/Q)$ for $ZnTiO_3$-impregnated CFI and straight-tube reactors under visible-light and dark conditions. Solid lines represent best linear fits and dotted lines denote 95% confidence interval bands.

The extent of MB dye adsorption onto the $ZnTiO_3$ photocatalyst under dark CFI operation in the CFI was evaluated using the expression $[(1 - C_{ss,dark}/C_0) \times 100]$, where C_{ss} is the steady-state outlet dye concentration under dark conditions. The calculated adsorption percentage was approximately 4.5%, indicating minimal dye uptake in the absence of illumination.

Since residence time and flow rate are inversely related, *1/Q* is proportional to the residence time, τ. The degradation process will improve from a longer residence time, allowing the dye molecules to interact more thoroughly with the $ZnTiO_3$ particles. The curves are typically linear, with positive slopes, because the degradation increases as the residence time increases.

It can be seen from the Figure that slope of light data (denoted by triangle and circle) is higher than that of dark data (denoted by square) confirms the suitability of photocatalysis process, moreover the slope of CFI data is steeper than that of straight tube data confirming a higher degradation rate or effectiveness of CFI over straight tube in the process. Thus, it can be inferred, as (1/flow rate) increases (which corresponds to decreasing flow rate), the extent of dye degradation increases and is more productive in CFI rather than in straight tube.

The percentage enhancement in photocatalytic activity observed from the respective rate constants with 95% CI, is presented in Table 3.3.

Table 3.3: Comparison of photocatalytic dye degradation in light and dark conditions with the rate constants (95% CI) followed by the first order kinetic model.

Parameter	Dark CFI (k_d)	Light straight tube (k_s)	Light CFI (k_c)
Rate constant, k ($\times 10^{-3}$ min^{-1})	3.69	10.60	24.66
95% CI for k ($\times 10^{-3}$ min^{-1})	1.69 – 5.69	7.32 – 13.88	18.38 – 30.94
Enhancement with respect to (k_d)	-	187.3%	568.3%
Enhancement with respect to (k_s)	-	-	132.6%

Since it is the surface area where the catalytic reaction occurs, it is necessary to normalize the rate constant per unit exposed surface area to quantify the efficacy of the catalytic reaction. In this context, the photocatalytic activity of $ZnTiO_3$ particles (crystallite size 29 nm and band gap 3.8 eV) in a batch reactor, as reported in an earlier work[118], is compared. In this work, with 10 mg particles in 40 mL of 10 ppm methylene blue dye solution yielded the value of rate constant (k) to be 0.0472 min^{-1}. Knowing the average crystallite size and density of the oxide particles,[135,136] the rate constant per unit exposed area can be calculated and compared to our work. The batch mode operation in Ref [118] yields a rate constant as 7.36×10^{-6} min^{-1} cm^{-2}, while in our arrangement, with the continuous flow processing and immobilized particles, the rate constant per unit surface area are found to be 1.02×10^{-3} min^{-1} cm^{-2} in straight tube configuration and 2.38×10^{-3} min^{-1} cm^{-2} in CFI configuration, which are much higher than the values obtained from Ref [118] for batch processing.

3.7 Challenges encountered and resolutions implemented

During the development and evaluation of the $ZnTiO_3$-impregnated PDMS-lined CFI reactor, several practical and operational challenges were encountered. The major challenges and the corresponding resolution attempts are summarized below.

- **Challenge:** Agglomeration and poor dispersion stability of $ZnTiO_3$ nanoparticles resulted in non-uniform immobilization inside the PDMS-lined tube.
  Resolution: Plasma treatment, sonication, and pre-filtration of the $ZnTiO_3$ suspension were employed to improve particle dispersion and coating quality.
- **Challenge:** Sensitivity of plasma treatment conditions, where insufficient treatment produced weak particle adhesion while excessive treatment affected PDMS integrity.
  Resolution: Plasma exposure parameters were optimized to achieve effective surface activation without compromising reactor transparency and structural stability.
- **Challenge:** Non-uniform swelling and deswelling of PDMS caused uneven particle incorporation along the reactor wall.
  Resolution: A controlled and reproducible solvent swelling protocol was developed to ensure consistent nanoparticle infusion throughout the CFI.
- **Challenge:** Irregular catalyst patches caused localized light scattering and reduced photon penetration.
  Resolution: Controlled and uniform suspension injection was adopted to improve coating uniformity along the reactor length.
- **Challenge:** Flow instabilities at higher flow rates due to complex Dean vortex interactions in the CFI geometry.
  Resolution: Calibrated syringe pumps and flow stabilization methods were utilized to maintain steady-state continuous-flow operation.
- **Challenge:** Possible particle detachment under continuous-flow conditions.
  Resolution: Repeated rinsing and stabilization cycles were carried out prior to photocatalytic experiments to ensure stable catalyst adhesion.

The unresolved aspects identified in this chapter indicate the need for further investigation and have been briefly noted in the Summary section, with further discussion included in Chapter 7 under the future research scope.

3.8 Literature comparison with the present work

To place the present work in context, a comparison with relevant literature reports from the same field is presented in Table 3.4.

Table 3.4: Comparison of reported photocatalytic methylene blue degradation systems across batch and continuous reactors.

Reactor Type	Catalyst System	Mode	MB Performance/rate constant, k	Ref.
Batch	TiO_2 nanoparticles	Batch	90% degradation in 1 h; complete in 2 h	[137]
Batch slurry	ZnO nanoparticles	Batch/sunlight	98.5% degradation in 60 min	[138]
Continuous	RGO/GO/Bi–TiO_2 nanotubes	Continuous/UV	~89% removal in 150 min; 3.4× higher visible-light rate.	[139]
Batch	g-C_3N_4	Batch/simulated solar	100% degradation in 60 min	[140]
Batch	$ZnTiO_3$/TiO_2 immobilized in geopolymer	Batch/UV irradiation	93% photodegradation; k = 0.018 min^{-1}	[141]
Stepped continuous flow	Ag^+-doped TiO_2	Continuous	>99% decolorization at 1 L/h after 120 min	[142]
Batch slurry	$ZnTiO_3$-700 °C	Batch/low intensity UVB	57.4% removal in 180 min; k = 0.0048 min^{-1}	[35]
Batch slurry	g-C_3N_4/h′$ZnTiO_3$-a′TiO_2 direct Z-scheme composite	Visible light	99.8% degradation for 50 wt% CN/h′ZT-a′T; k = 2.92 h^{-1} = 0.0487 min^{-1}	[143]
Continuous PDMS–CFI	Plasma-activated $ZnTiO_3$ immobilized	Continuous visible light	k = 24.66 × 10^{-3} min^{-1}; 2.3× vs straight tube	This work

3.9 Summary

A novel method of plasma treated photoactive particles ($ZnTiO_3$) impregnation inside a silicon tube folded in the form of CFI, is reported. The method consists of coating the CFI with PDMS film first, swelling the film, and subsequently subjecting the swollen film to the aqueous suspension of the photocatalytic zinc titanate particles. Finally, deswelling the film results into the particles getting immobilized in the film partially exposed to the flow

region. The application of $ZnTiO_3$ impregnated CFI for the degradation of methylene blue dye from wastewater has been studied at different flow rates in dark and light conditions and compared with same tube in straight configuration. The result showed that a very little value of particle area fraction 0.105 having band gap energy of 2.77 eV, are sufficient to perform photocatalysis when used in CFI. The observed rate constants (k ± 95% CI half-width) are $10.60 \pm 3.28 \times 10^{-3}$ min^{-1} in the straight tube configuration, and $24.66 \pm 6.28 \times 10^{-3}$ min^{-1} with the CFI. Thus, CFI not only enhance the kinetics of photocatalysis process more than twice as compared to the straight tube but also facilitates a continuous flow process in a comparatively less and confined space. This novel technique can be useful in miniaturization applications. The experimental technique can be used for continuous processing of wastewater utilizing the immobilized impregnated CFI, thereby safeguarding the environment and human health. Further research efforts are justified to optimize the process parameters and scale up the technology for industrial implementation in wastewater treatment plants. The degradation efficiency of MB dye using $ZnTiO_3$ impregnated CFI can be influenced by various factors, including catalyst loading, solution pH, light intensity, and flow rate[144,145]. Optimization of these parameters is crucial to achieving high degradation rates and minimizing energy consumption. Additionally, the long-term stability, possible leaching, and recyclability of $ZnTiO_3$ particles immobilized within the PDMS-lined CFI need to be evaluated under Dean-vortex-induced shear to ensure sustained photocatalytic performance and practical feasibility. In this work, however, only the feasibility of such a reactor is established, and influence of all these above-mentioned factors on the performance of the reactor will be presented in a separate work. Future work will focus on validating the performance of the developed system under more realistic conditions, including higher dye loadings, elevated TDS, and alkaline pH, to better assess its practical applicability for textile wastewater treatment.

Chapter 4: Fabrication and Comparison of Neat and SiOC-Impregnated PDMS Membranes for Pervaporation of Ethanol from a 1:1 Ethanol–Water (v/v) Mixture

4.1 Abstract[†]

This study demonstrates that ethanol extraction from an ethanol–water mixture is significantly enhanced when a PDMS membrane is selectively impregnated with silicon oxycarbide (SiOC) particles near one surface. High surface-area SiOC particles (192 $m^2 g^{-1}$), a polymer-derived ceramic (PDC) synthesized by heat-treating a PDMS sponge wrapped in aluminium foil at 550 °C, were characterized using XRD, HR-TEM, BET, and SEM–EDX, confirming an amorphous Si–O–C structure with nanoscale morphology and porous characteristics. A 10% cross-linked PDMS membrane was subsequently infused to a depth of ~100 µm by exposing one surface to a SiOC suspension in di-isopropylamine, forming an asymmetric structure. Cross-sectional SEM–EDX, porometry, and contact angle measurements indicate localized particle incorporation, broadened pore-size distribution, and increased surface hydrophilicity relative to the native membrane.

Pervaporation experiments were conducted at 298 K with atmospheric feed pressure and a permeate side maintained at 21 kPa and 3 °C. Membranes (0.6 mm thickness, 0.001257 m^2 area) were operated for 12 h, yielding ~5 mL permeate and an overall flux of ~331 mL $m^{-2} h^{-1}$. Despite low ethanol flux, the SiOC-modified membrane showed improved separation performance, with an average ~150% increase in the ethanol–water separation factor.

This enhancement is attributed to water adsorption by the SiOC phase, creating localized hydrated regions that promote ethanol transport via a mixed solid–liquid diffusion pathway, unlike the solid-phase diffusion in native PDMS. These findings establish selective SiOC infusion as an effective strategy for enhancing pervaporation performance.

Keywords: Polymer-derived ceramics (PDC), Silicon oxycarbide, Composite membrane, PDMS, Pervaporation. Interfacial phenomena, Liquid phase diffusion.

[†] This work is published in 'Chem Eng Commun (2026) 1–15' https://doi.org/10.1080/00986445.2025.2611392.

4.2 Introduction

Polymer-derived ceramics (PDC) is an area that has attracted a surge in research activity over the past 10-15 years[146]. PDC offers a versatile route for manufacturing ceramic-based components. Silicon-based ceramics are particularly convenient to produce using silicon-based polymers. One such important ceramic product is silicon oxycarbide (SiOC)[147,148]. SiOC particles are derived from the pyrolysis of polymeric precursors that contain silicon, oxygen, and carbons[149,150]. This process results in a network structure characterized by Si-O-C bonds, where carbon atoms are incorporated into the silicon dioxide (SiO_2) matrix. One of the distinguishing features of these materials is the presence of carbon in both hetero-bonded form with Si (carbide) and segregated graphitic form with carbon atoms joined by sp^2 bonding. The nano-crystalline graphitic domains are included inside the amorphous Si-O-C matrix. These graphitic carbon domains are believed to improve many properties of the material. The mechanical strength of SiOC is enhanced by the presence of carbon within the SiO_2 matrix, providing a balance between rigidity and toughness that is desirable in many structural applications[151,152]. Chemical resistance is another notable property of silicon oxycarbide particles. They exhibit excellent resistance to oxidation and corrosion, which extends their usability in harsh chemical environments[153,154]. This chemical inertness, combined with their thermal stability, makes SiOC materials ideal for use in industries, such as, catalysis and energy storage[155]. The high specific surface area of SiOC particles, which can reach several hundred square meters per gram, is particularly beneficial in these fields. Since in catalytic applications, the high surface area allows for better dispersion of catalytic active sites, enhancing the overall efficiency of the catalytic process[156,157].

The porous nature of SiOC materials is a significant advantage in adsorption applications, such as, gas separation, water purification, and pollutant removal[154,158–160]. The high surface area and porosity enable these materials to adsorb large amounts of substances, making them highly effective in these roles. Moreover, the biocompatibility and chemical inertness of SiOC have led to explorations of their use in biomedical applications, including drug delivery systems[161]. The versatility of silicon oxycarbide particles continues to drive interest and innovation, promising exciting developments in the future.

Ethanol has been identified as a renewable fuel blend which can potentially reduce the consumption of fossil fuels and subsequently reduce the emission of greenhouse gases.

Several countries have focused on energy security and reduction in environmental pollution through regulatory mechanisms that include an emphasis on blending gasoline with ethanol. Ethanol is obtained primarily from cellulosic biomass through chemical or biochemical processing routes. When manufactured through the biological fermentation route, ethanol is present in the fermentation broth as a mixture with water and other compounds and requires further separation and purification steps. Processes, such as, adsorption, extractive distillation, vacuum membrane distillation, pervaporation, and vapor permeation have been employed to separate ethanol from its aqueous solution[162]. However, in the distillation and extraction processes the selection of separation method is to be optimized depending on the characteristics and type of solution to be separated[72]. The boiling point of ethanol is around 78℃ which is close to the water boiling point, which is why mere distillation will not provide effective purification as a higher boiling point difference is required in the distillation process. Ethanol is not suitable for extraction as it is miscible with almost all solvents, and without a proper immiscible solvent that can cause phase separation, the extraction process cannot be designed. Pervaporation is an energy-efficient and clean technology process in comparison to distillation and extraction[163]. In this process, permselective hydrophilic or hydrophobic polymeric membranes are employed to separate a single liquid mixture phase into its constituting components. Contrary to conventional distillation, the driving force for mass transfer is the difference in the partial pressure of constituents across the membrane matrix. Because of the partial pressure difference, a gradient in the chemical potential of the components present in the liquid mixture is created between the feed and permeate side of the membrane. The chemical potential gradient, which is the actual driving force for separation, the components have different permeabilities across the membrane matrix and are subsequently separated. The application of pervaporation is not only limited to the chemical industry, like, production of bioethanol (fuel ethanol from biomass), dehydration of fine chemicals, recovery, purification of organic solvents (yielding larger than 99%), food solvents and waste-water treatment but also it has been proved to be environment friendly due to emission reduction[164–166].

Polydimethylsiloxane (PDMS) membrane is hydrophobic and is highly permeable to organic solvents. The PDMS membrane does not allow the water to pass but it can attract the volatile organic compound (ethanol) to permeate through it by creating a partial pressure difference, as mentioned above. Therefore, pervaporation by the PDMS

membrane provides higher selectivity to ethanol while consuming less evaporation energy[167–170]. Pervaporation is enhanced with superhydrophobic membranes[171]. Improved production and enrichment of bioethanol from its aqueous mixture has been obtained through pervaporation technique using pure PDMS polymeric membranes[172,173].

PDMS material has been utilized in various physical forms to fabricate membranes for filtering applications[174,175]. One possible modification to the PDMS matrix for engineering its permeability is to infuse it with suitable particles. PDMS infused with filler materials (organic/inorganic), like, zeolite particles, fluorine, graphene and its derivatives, tree bark biochar, carbon black, and silica particles have been shown to enhance separation efficiencies compared to their neat counterparts[176–183]. The overall efficiency of the process depends on the structural and physio-chemical properties of the polymer matrix and filler materials, in addition to the process operating conditions. PDMS matrix offers such a desired platform of flexibility and tunability with silicon oxycarbide particles which in turn support the membrane with stability, non-toxicity and greater strength.

In this work, the preparation of SiOC particles using PDMS by a novel method and the subsequent impregnation of PDMS membranes with these particles, are reported. By virtue of being compatible with the PDMS matrix, these particles readily infuse into the matrix modifying its properties and improving its pervaporation characteristics. A novel technique is also utilized to infuse the particles in the membrane as well, wherein one side of the PDMS membrane is exposed to suspension of silicon oxy-carbide particles in di-iso-propylamine (DIPA). The DIPA swells the membrane and infuses it with the particles. Subsequently, DIPA is allowed to evaporate, and a membrane is dried, leaving a membrane impregnated with the particles. A similar concept has been used in past work to line the microchannels in PDMS with a metal oxide layer[184]. The impregnated membranes are tested for the pervaporation of ethanol-water mixture, and it is found that the pervaporation of ethanol is better in these as compared to the neat membranes. It is to be noted that even though the membrane surface becomes more hydrophilic upon impregnation, ethanol pervaporation is improved in these. A plausible explanation for the observed behavior is offered. This work in current form focuses only on showing that SiOC particles improve ethanol pervaporation. A detailed account, including flux measurements and possible removal of the impregnated SiOC from the membrane will be presented elsewhere.

4.3 Research gaps

Pervaporation (PV) of ethanol–water mixtures using PDMS membranes has been extensively studied because of the organophilic nature and chemical stability of PDMS. Most reported enhancements rely on conventional fillers, such as, silica, zeolites, and metal–organic frameworks (MOFs), generally incorporated through uniform bulk dispersion within the membrane matrix.

In contrast, comparatively limited attention has been given to polymer-derived silicon oxycarbide (SiOC) particles as functional fillers for PDMS membranes, despite the high surface area (~192 $m^2 g^{-1}$) of SiOC synthesized from pyrolyzed PDMS foam, which may significantly influence membrane transport behaviour. Furthermore, most reported studies focus on relatively dilute ethanol feeds (typically 5–20 wt%), while membrane performance under equivolume ethanol–water mixtures remains insufficiently explored.

Accordingly, important research gaps persist regarding:

- The influence of SiOC impregnation on the microstructure, hydrophobicity, free volume, and transport pathways of PDMS membranes, particularly under asymmetric surface impregnation.
- The performance of PDMS–SiOC membranes under high-concentration ethanol–water feeds, where transport behaviour may deviate from conventional solution–diffusion mechanisms.
- The role of localized SiOC domains in modifying ethanol selectivity and permeation behaviour in PDMS membranes.

The present chapter addresses these gaps by systematically comparing neat PDMS and SiOC-impregnated PDMS membranes under a 1:1 ethanol–water feed composition and investigating how SiOC incorporation alters membrane morphology and separation performance.

4.4 Synthesis method of SiOC particles and membranes

4.4.1 SiOC particles

The silicon oxy-carbide particles to be used in impregnation of the membrane had been prepared by the process of thermal degradation of PDMS sponge, fabricated in our

laboratory itself. The sponge was prepared by heating an appropriate solution of Sylgard 184 PDMS solution containing silicone elastomer base and 10 wt% curing agent in tetrahydrofuran (THF), during which THF evaporated and PDMS cross-linking occurred simultaneously, resulting in a sponge-like material. The sponge was covered with aluminium foil and kept inside a muffle furnace at 550°C for 2 hours with a fast heating and cooling rate of 50 °C min^{-1}, yielding brittle and hard particles which were finely crushed using mortar and pestle. A flow diagram representing the synthesis of SiOC particle is shown in Figure 4.1. (It was observed that when the sponge pieces were not covered inside the aluminium foil, the obtained particles did not assist in the separation of ethanol by pervaporation).

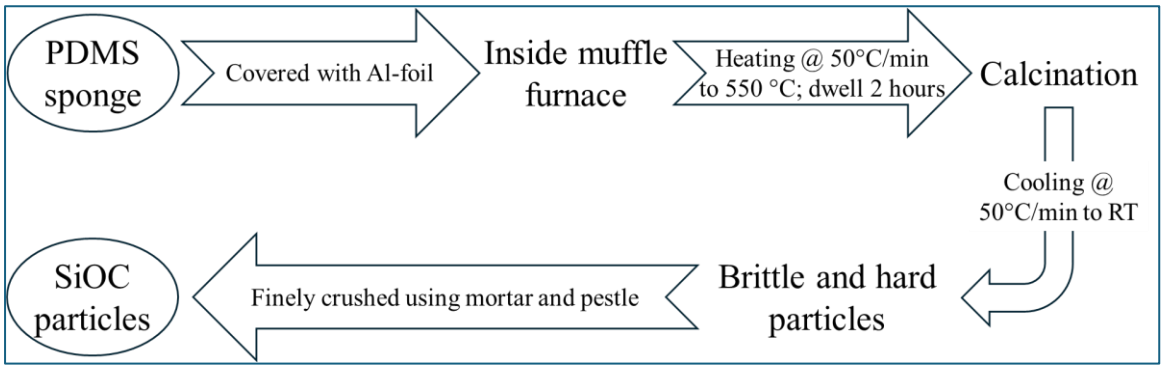

Figure 4.1: Flow diagram of SiOC particle synthesis.

To address the possibility of contamination from the aluminum foil during the thermal conversion of PDMS sponge to SiOC particles at 550 °C, it is important to clarify that the foil serves only as a physical support during pyrolysis and does not participate chemically in the process. Aluminum surfaces spontaneously form a thin, dense, and strongly adherent native aluminum oxide (Al_2O_3) layer upon exposure to air. This passivating oxide layer is chemically stable up to temperature 550 °C used in this study and effectively prevents diffusion, transfer, or leaching of aluminum species into contacting solids during heat treatment[185,186]. Consistently, no Al or Al–O signatures were detected in the XRD and EDX analyses of the SiOC particles or SiOC–PDMS membranes, confirming that aluminum does not contribute to the chemical composition or morphology of the synthesized materials. In contrast to our method, the previous methods have utilized high temperature (≥ 900 °C) treatment to obtain the SiOC particles[147–150].

4.4.2 Membranes

The Sylgard 184 base elastomer and its cross-linker (10 wt%) were mixed, de-gassed and spread up to the desired height (membrane thickness) in a petri dish. For curing and

complete cross-linking, the dish was kept in a perfect horizontally levelled microwave oven and heated at 100 W for 1 hour to get the desired native membrane.

In order to impregnate the membrane with silicon oxy-carbide particles, one side of the membrane was kept in contact with the DIPA suspension, containing 40 mL of DIPA solvent and 40 mg of silicon oxy-carbide particles, till its complete evaporation. DIPA provided the necessary widening of pore size due to swelling of the membrane and thus induced incorporation of the silicon oxy-carbide particles is achieved in the membrane. A schematic representation of the adopted process is shown in Figure 4.2.

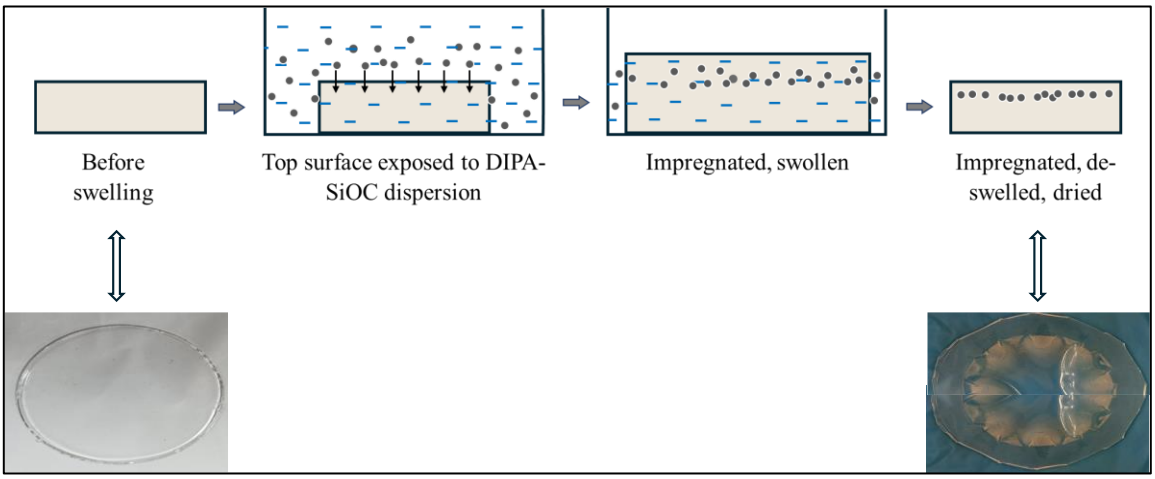

Figure 4.2 Schematic representation of the process leading to membrane impregnation.

The obtained impregnated membrane was followed by drying and washed with de-ionized water several times to ensure the removal of any foreign particles and impurities on the surface of the membrane.

4.5 Pervaporation setup

A schematic representation of the equipment for the pervaporation process is shown in Figure 4.3. The membrane-holding assembly used for pervaporation consisted of two detachable parts made of borosilicate glass and a metal clamp to fasten them. The upper part is a cylindrical funnel which holds the feed from the top, the middle part is an integrated fritted glass base to support the membrane, and the bottom flask is used for collecting the permeate.

The middle part along with a glass frit base protrudes a funnel to the bottom and has an in-built vacuum port to which a vacuum pump is attached. The permeate-collecting bottom flask is cold-trapped with ice-gel packs and thermally isolated inside a foam-insulated box. In pervaporation, the pressure gradient (due to applied differential vacuum) and

temperature gradient (due to cold trap) between the feed and permeate side are the driving forces to create phase transition and permeate the vapor through a membrane[187,188].

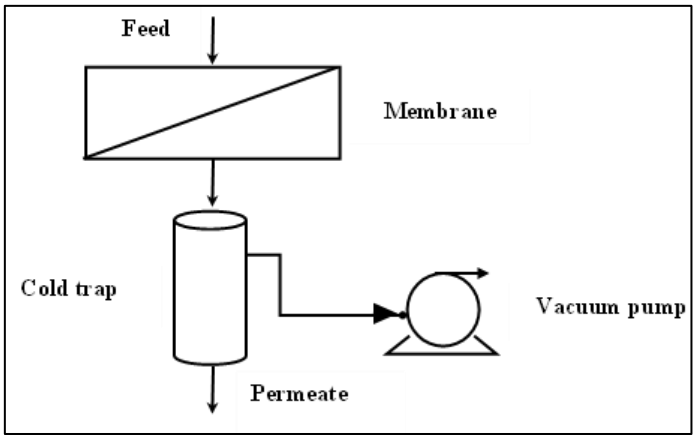

Figure 4.3: Flow diagram for pervaporation experimental setup.

In all the experiments, the feed was kept at atmospheric pressure and room temperature (298 K) whereas the permeate side was maintained at an absolute pressure of 21 kPa by a diaphragm-type vacuum pump and temperature of 3 ℃ by ice-gel pack support. The thickness and enclosed effective area of the membrane were 0.6 mm and 0.001257 m^2 respectively. The mounted membrane to assembly, wrapped using parafilm first then clamped to ensure pressure tight seal. The process of pervaporation was performed for 12 hours for each of the native and impregnated PDMS membranes. The permeate vapor, condensed due to the cold trap, was collected (~5 mL) at the bottom of the assembly. A standard permeation relation, $J = \frac{V}{A\,t}$ was used to compute the overall flux, where V is the collected permeate volume, A is the effective membrane area, and t is the permeation time. The resulting flux is $J \approx 331\ \mathrm{mL\,m^{-2}h^{-1}}$, demonstrating the extremely low absolute permeation rate characteristic of ethanol–water mixtures under the tested conditions. Although small in magnitude, this quantified flux enables a direct and meaningful comparison of transport behavior and separation performance between the native and SiOC-impregnated membrane configurations.

4.6 Results and discussion

4.6.1 Characterization of the SiOC particles

4.6.1.1 XRD analysis

The X-ray diffractograms of SiOC particles have been shown in Figure 4.4 showing a typical broader Bragg peak centered on the 2θ value of 22.25°, which confirms the

amorphous phase of SiO_2 particles[189]. Our TEM image suggests the presence of graphitic domains. However, the graphitic peak expected to be observed at around *2θ* value is 27° is not clearly seen in the XRD pattern of the particles because of the broad span of the peak due to the amorphous phase of SiOC[190]. However, one additional broad diffraction peak appearing to be centered at around 70.70 degrees, can be indexed to the (311) planes of the cubic phase of silicon carbide (SiC) shown in Figure 4.4, as confirmed from the JCPDS card no. 29-1129[191]. Additionally, the two weak and broad peaks at around 36° and 48° can also be attributed to the amorphous SiC phase[192]. Thus, these additional broad peaks suggest the presence of an amorphous phase of cubic SiC.

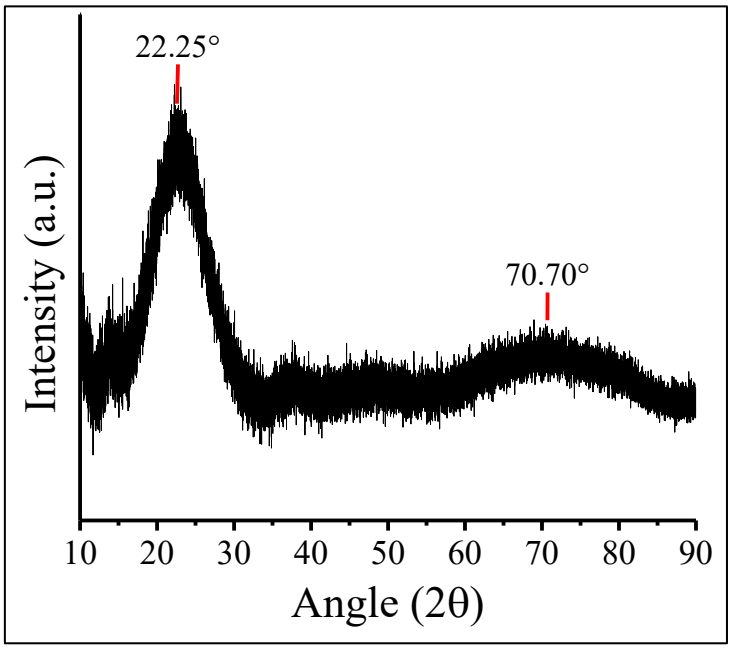

Figure 4.4: XRD pattern for silicon oxy-carbide particles.

4.6.1.2 Specific surface area analysis

The adsorption isotherm is obtained by measuring the volume of gas adsorbed onto the silicon oxy-carbide particles at different relative pressures (P/P_o) at a constant liquid nitrogen temperature (77 K), as shown in Figure 4.5. A surface area of 192 $m^2\ g^{-1}$ indicates that the silicon oxy-carbide particles have a moderately large amount of surface area available for adsorption. Small hysteresis also suggests that the particles are nanoporous as suggested by the pore size distribution shown in Figure 4.5. These nanopores may be arising because of the amorphous nature of the material. Pore size distribution in figure 4 suggests the presence of nanopores with sizes lying in the range of 1-5 nm, and also micropores in the range of 100-300 nm.

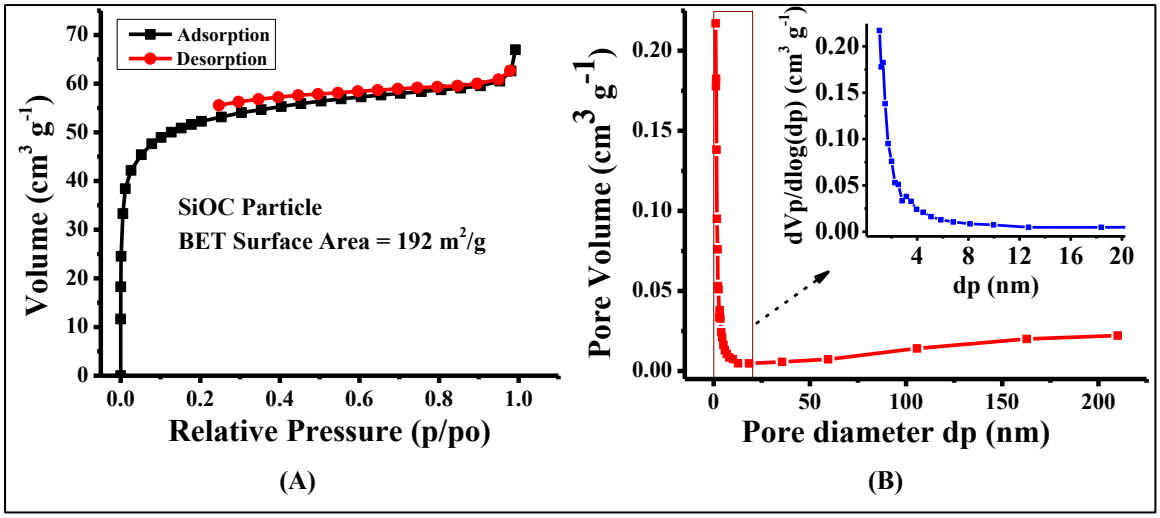

Figure 4.5: Surface area estimation using BET nitrogen adsorption−desorption isotherm plot for silicon oxy-carbide particles.

4.6.1.3 Morphology

The Scanning Electron Microscopic (SEM) image and Energy dispersive X-ray (EDX) composition analysis of silicon oxy-carbide particles have been shown in Figure 4.6 (A) and (B) respectively. It is noticed from the EDX result that silicon and oxygen are the primary contents in particles as in the SiOC particles the carbon atoms substituting the silicon atoms are in minority and therefore will present weak signal.

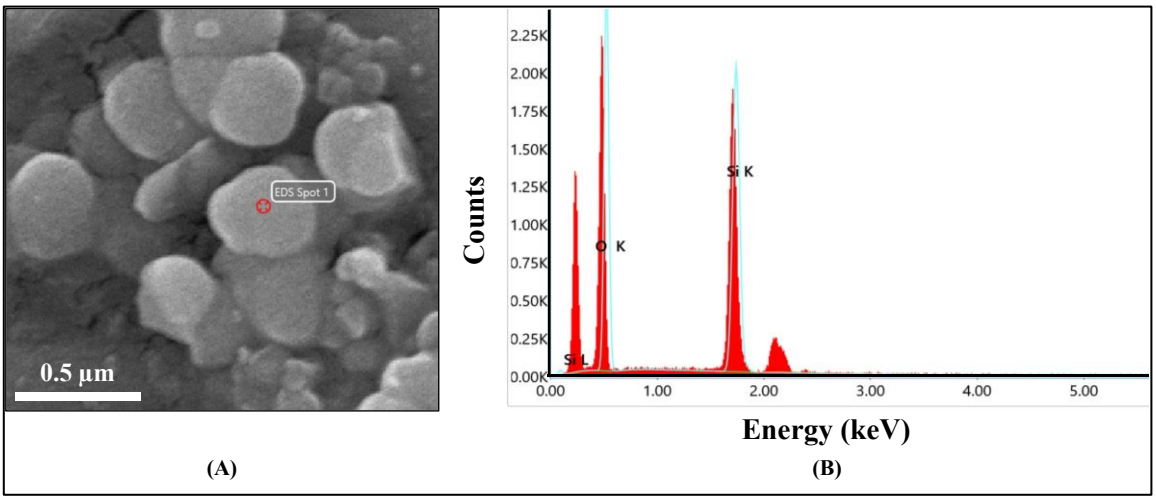

Figure 4.6: (A) SEM image and (B) Spot EDX of SiOC particle showing Si and O composition.

Moreover, the energy value for the carbon K shell electrons is very close to that of silicon, and therefore the carbon peak is not detectable in the EDX graph. The morphology suggests that the particle size ranges from 100-400 distribution which is clear from the SEM images.

4.6.1.4 HR-TEM

Figure 4.7 (A, B) shows the high-resolution TEM image of brittle SiOC particles. Image (B) clearly shows the graphite basal planes which are known to have an interplanar separation of 0.3320 nm[193]. The graphite signature is missed in the XRD pattern, but the TEM image confirms its presence.

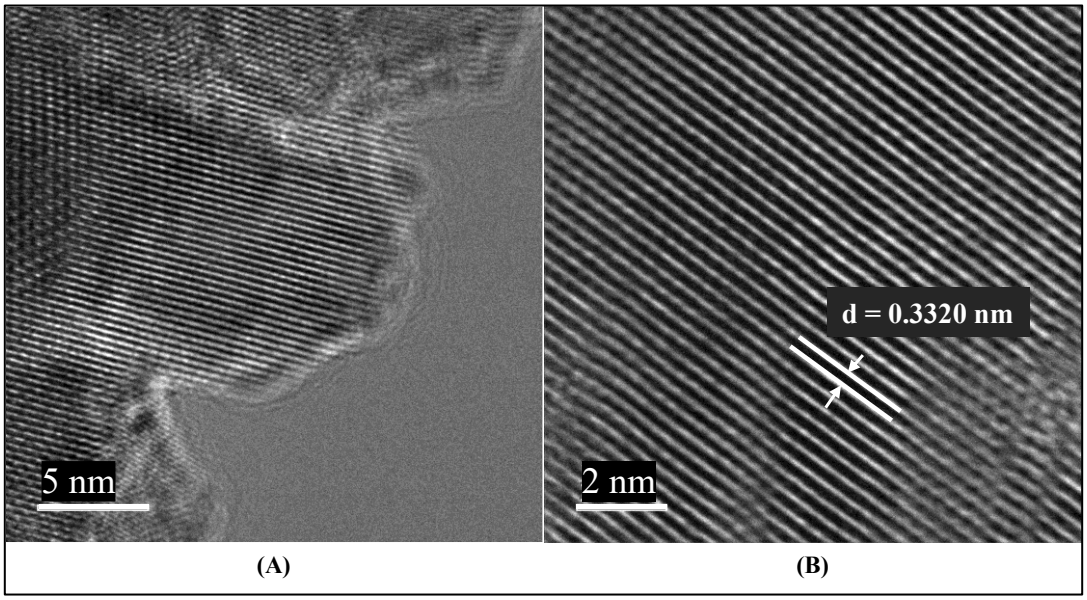

Figure 4.7: (A, B) TEM images of brittle SiOC particles with two different magnifications.

Thus, it is concluded that the SiOC phase obtained by fast heating and cooling of the covered PDMS sponge results in the formation of graphitic carbon[190]. Furthermore, covering the brittle SiOC particles prevents the carbon atoms from escaping and thereby leads to the formation of a graphitic phase in these samples due to adequately available carbon atoms.

4.6.2 Characterization of the membranes

4.6.2.1 Morphology

The cross-section of the impregnated membrane is characterized with SEM/EDX to reveal the depth of impregnation of particles inside it. Figure 4.8 presents the cross-section SEM image and EDX analysis at two different spots. The membrane thickness was 600 µm, and the particles were infused from one side up to a depth of 100 µm as seen in image Figure 4.8 (A). The SiOC particles constitute mostly of Si-O-Si network in which minority silicon atoms are substituted by carbon atoms. Hence the carbon fraction in SiOC is much smaller compared to the PDMS material which is because during the sponge pyrolysis most of the carbon escapes as CO_2.

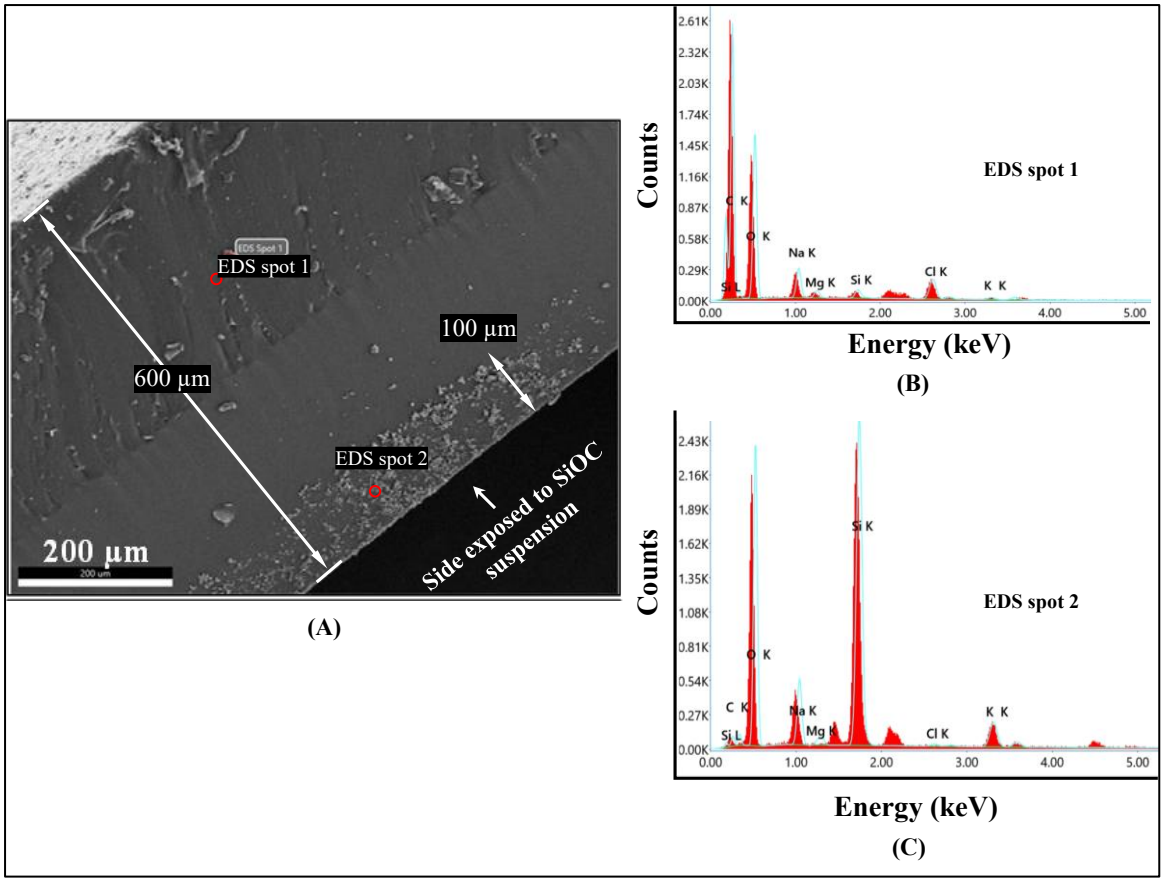

Figure 4.8: (A) SEM image comparing particle impregnation at two spots 1 and 2 inside a membrane exposed to SiOC suspension and (B, C) EDX of SiOC impregnated membrane at two different spots in cross-sectional areas.

This is also evident from the EDS spectra of spots 1 and 2 in this Figure where spot 1 (PDMS region) shows higher carbon signal as compared to spot 2 (SiOC region). The other peaks in EDX analysis viz., Na and Mg are the impurities that remained due to the treatment of the membrane with water.

4.6.2.2 Capillary flow porometry of the membranes

The capillary flow porometry test was performed by doing a wet run followed by a dry run condition on the membranes. The impregnated membrane was placed inside the test cell such that the side exposed to particles faced the gas pressure. The pore size is measured using the Washburn equation[194], given by:

$$D = 4\sigma \cos\theta / p \qquad (4.1)$$

Where D is the pore diameter, σ is the surface tension of the wetting fluid, θ is the contact angle, and p is the differential pressure.

Pore distribution is calculated using the pore distribution function[195,196] as:

$$f = \frac{d[(\frac{f_w}{f_d}) \times 100]}{dD} \tag{4.2}$$

Where f_w is the flow rate through a wet sample, f_d is the flow rate through the dry sample, and D is the pore diameter.

The measured pore size distribution is shown in Figure 4.9 (A) and (B) for native PDMS and SiOC-impregnated membranes respectively.

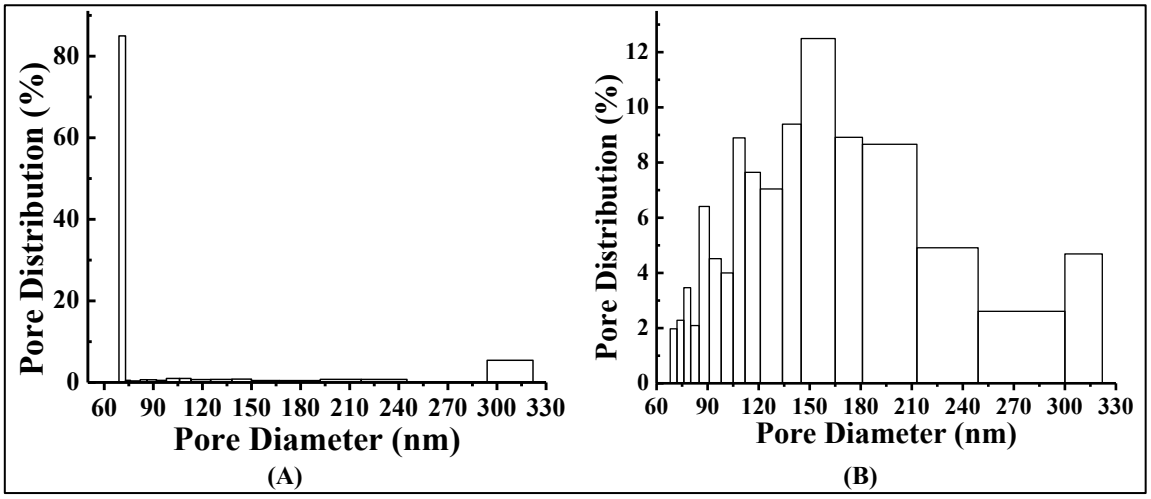

Figure 4.9: Graphs showing percentage pore distribution (A) native, and (B) SiOC impregnated PDMS membranes.

It is evident from this result that particle impregnation dramatically affects the nearly monodisperse pore size distribution in the native membranes, causing pores with a wide range of sizes to open up. Silicon oxy-carbide particles have high surface area-to-volume ratios due to their nanoscale dimensions and porous structure[197]. The wide pore size distribution in impregnated membranes arises chiefly due to the impregnated particles whose surface area analysis also showed a similar pore size distribution as presented in Figure 4.5. Owing to a wide pore size distribution and a large specific surface area of the particles, the membrane's ability to interact with the surrounding molecules is enhanced[198]. Although porometry indicated relatively large equivalent pore openings, these pores do not represent continuous liquid-flow channels across the membrane thickness. The SiOC modification was localized mainly near one surface, while the remaining PDMS matrix retained its dense and hydrophobic character. Therefore, during pervaporation, transport occurred through sorption–diffusion–desorption rather than bulk liquid leakage, and no visible leakage was observed under the applied operating conditions.

4.6.2.3 Surface hydrophobicity

As reported previously, the SiOC region formed on the surface of the SiC through oxidation leads to an increase in hydrophilicity[199]. Contact angle measurement of the face of the membranes in our work that was exposed to the SiOC particles for infusion also showed increased hydrophilicity as compared to the neat membranes. The contact angle changes from 105° in the neat membrane to 85° in the infused membranes, as shown in Figure 4.10. The hydrophobicity in PDMS can be attributed to the methyl groups, whereas in SiOC the carbon content is significantly less compared to Si-O subunits. The presence of more oxygen as compared to methyl groups in the SiOC particles present in the sub-surface region leads to enhancement in water wettability of the surface of the membrane.

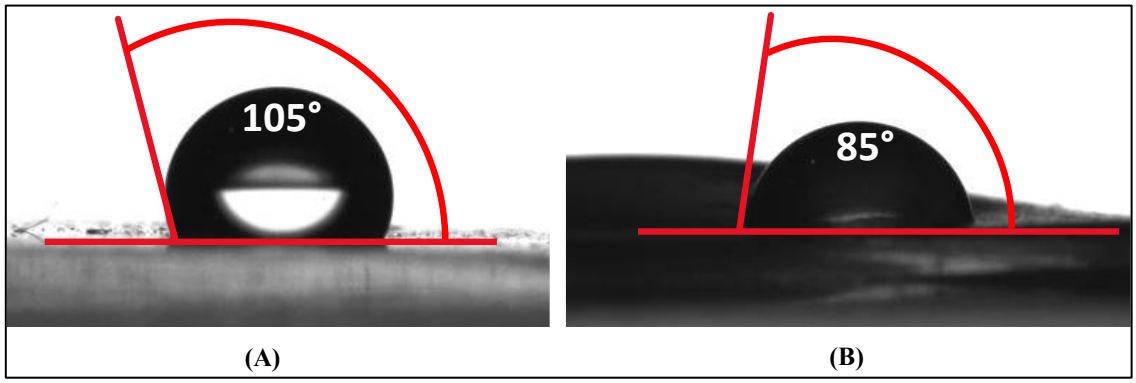

Figure 4.10: The water contact angle for (A) native PDMS membrane and (B) SiOC-impregnated membrane.

The effect of the polarity of the group attached on one side of the membrane has been observed to correlate with the water selectivity in the pervaporation experiments, and water selectivity increases as the contact angle is decreased[200]. The opposite effect is observed that the water selectivity in the impregnated membranes showing hydrophilicity (on the impregnation side) decreases. An explanation of this trend is offered in the following section.

4.6.3 Pervaporation of the ethanol-water mixture

Ethanol-water separation performance of the synthesized native and impregnated membranes was evaluated under the pervaporation conditions using a 50-50 (vol-vol) ethanol-water mixture. The permeate composition is analyzed using gas chromatography for comparison. Figure 4.11 (A-C) shows the comparison between the gas chromatograms of permeate samples from the native and SiOC-impregnated membranes. The peak corresponds to the ethanol response in the sample.

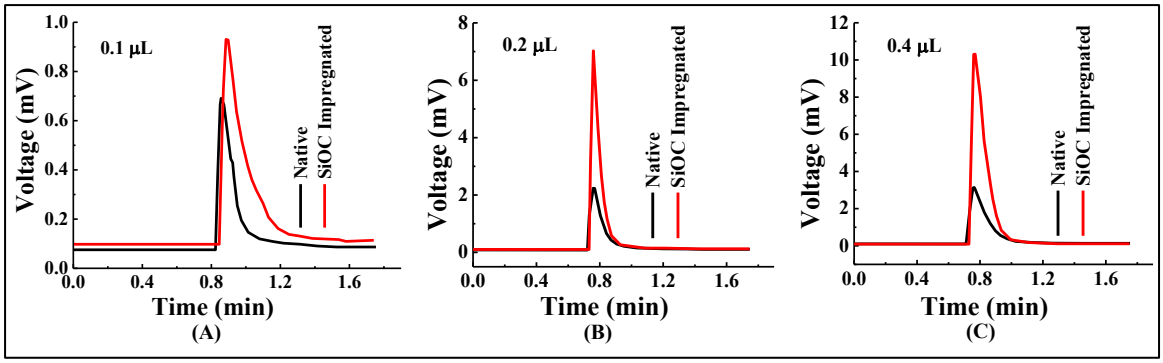

Figure 4.11. Chromatograms showing peaks of ethanol in permeate (A), (B), (C) for comparing native and SiOC-impregnated PDMS membrane.

It can be seen from the figure that in the case of SiOC-impregnated membrane, the area under the curve is significantly greater in comparison to the area under the curve of the native membrane. This indicates that the SiOC-impregnated membrane permeate has more ethanol content as compared to the native membrane. Moreover, it can also be seen that with an increase in the sample volume, the difference in the area under the curve is also increased as tabulated in Table 4.1 confirming the higher concentration of ethanol.

Table 4.1: Gas chromatography results for comparison of pervaporation from the membranes.

Sample amount (µl)	Permeate area (µ volt sec)		Area difference (b-a)
	Native (a)	SiOC impregnated (b)	
0.1	3367	5978	2611
0.2	10290	26939	16649
0.4	19521	60804	41283

Notably, in earlier experiments, a more hydrophilic surface of the membrane has been taken to imply higher water interaction, and therefore higher water permeation through the membranes. However, our results show the opposite behaviour, i.e. the impregnated membranes showing higher hydrophilicity (*but on one face only*) have higher permeability for ethanol.

This behaviour can be explained as follows. Pervaporation involves a combination of diffusion, absorption, transport, and evaporation mechanisms to selectively separate components from liquid mixtures based on their differential permeability through the membrane. The ethanol fraction improves primarily due to several enhancements in the film's structural and chemical properties introduced by impregnating silica oxy-carbide particles. Firstly, the presence of these particles increases the membrane's selectivity for ethanol over water. Silica oxy-carbide particles present near the surface are hydrophilic and

introduce additional polar sites near the membrane surface, which preferentially adsorb water molecules through hydrogen bonding as compared to ethanol molecules since the latter have organic components. This selective interaction enhances the water adsorption and pins the water molecules near the surface thereby forming a water-rich zone near the surface. The ethanol molecules diffusing in the PDMS membrane encounter a water-rich region in the impregnated membranes unlike in the neat membranes. Therefore, the diffusion path of the ethanol molecules, which consists mostly of solid phase in neat membranes, has both solid and liquid (water) regions in the impregnated membranes. Since the diffusion of ethanol through water is much faster compared to that in PDMS. Therefore, the effective diffusive transport in the impregnated membrane is significantly enhanced leading to a larger ethanol fraction in the permeate. Figure 4.12 shows the proposed explanation in pictorial form.

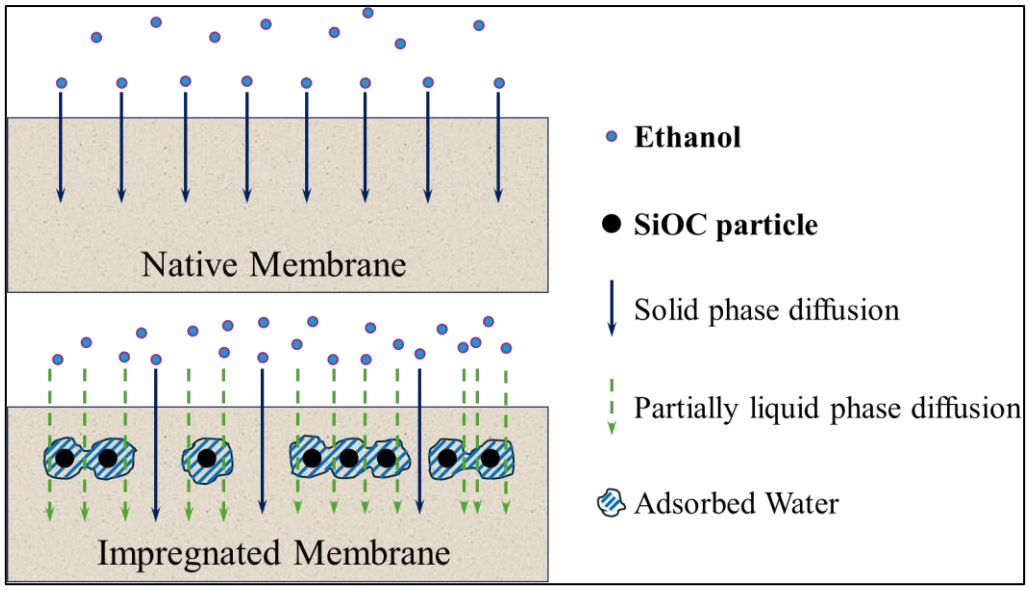

Figure 4.12: A proposed model explaining the relatively enhanced transport of ethanol in impregnated membranes.

The performance enhancement does not arise from simple hydrophilicity changes or increased surface roughness, but from a distinct interfacial transport mechanism created by the SiOC impregnation. Although the impregnated surface becomes more hydrophilic, the membrane exhibits preferential ethanol permeation, which is opposite to conventional expectations for PDMS systems. When SiOC particles are embedded near the feed-side surface, their polar Si–O–C groups attract and immobilize water molecules, forming a thin, structured water-rich interfacial layer. This layer does not significantly contribute to water flux but acts as a high-diffusivity pathway for ethanol, which partitions into and diffuses

more rapidly through this quasi-liquid zone than through bulk PDMS[201–203]. At the same time, the particles disrupt local polymer packing and increase free volume, creating additional microvoids that further reduce diffusion resistance for ethanol[204].

Thus, the improved separation arises from the combined effects of: (i) asymmetric interfacial hydrophilicity that traps water while facilitating ethanol transport, (ii) microstructural rearrangement of the PDMS matrix due to SiOC inclusion, and (iii) formation of a dual-phase diffusion pathway enabling faster ethanol transport relative to water. This mechanistic insight shows that the enhancement is not superficial or trivial; rather, it stems from a rationally designed interfacial architecture that tailors sorption–diffusion behavior without requiring chemical grafting or complex processing, offering a novel route for improving PDMS-based pervaporation membranes.

4.6.4 Membrane performance assessment by separation factor

The separation factor or selectivity factor (α) can be calculated using the relation below:

$$\alpha_{e/w} = \frac{(Y_e \,/\, Y_w)}{(X_e \,/\, X_w)} \tag{4.3}$$

where, $\alpha_{e/w}$ is the separation factor for ethanol over water; Y are mass-fractions in the permeate and X those in the feed.

Total feed of 30 mL containing 50% ethanol and 50% water by volume corresponds to approximately $X_e \approx 44$ wt% ethanol and $X_w \approx 56$ wt% water (ethanol density = 0.79 g mL^{-1}), giving an (X_e/X_w) factor of approximately 0.78571.

The concentration of ethanol, Y_e and water, Y_w in the permeate for the membranes, were estimated using the calibration curve equation, $y = 20568x$ (Figure 4.13) and permeate area (Table 4.1) and are shown in Table 4.2.

In cases where the injected sample volume was doubled (0.2 µL) or quadrupled (0.4 µL), the corresponding GC peak areas were normalized by dividing the measured areas by two or four, respectively. This adjustment brings the values back to the equivalent of a 0.1 µL volume injection as the FID response is linear within the concentration range studied and the detector produces proportionally higher peak areas for proportionally higher injected volumes.

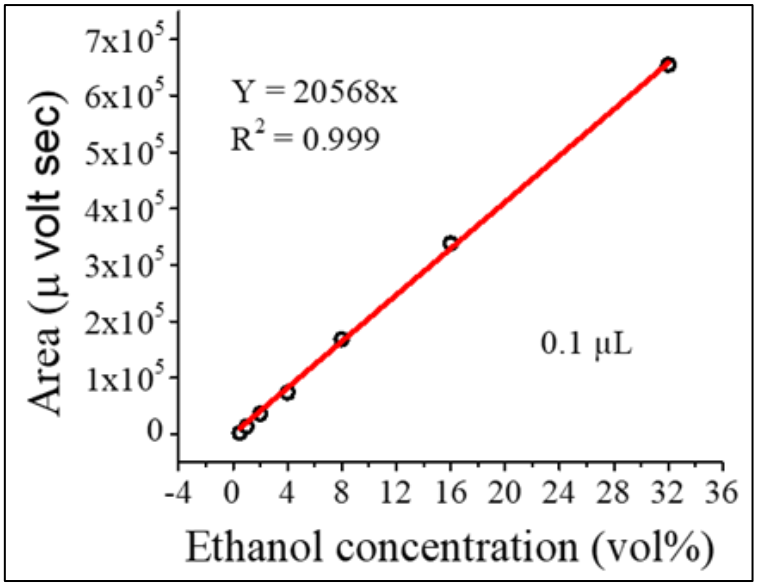

Figure 4.13: Calibration curve, representing linear fit at 0.1 μL sample volume for estimation of permeate mass fraction.

Table 4.2: Mass wt% of the permeate components obtained from GC area of Table 4.1.

Sample vol (μL)	Permeate ethanol, Y_e (mass wt%)		Permeate water, Y_w (mass wt%)	
	Native	SiOC impregnated	Native	SiOC impregnated
0.1	0.001293682	0.002297503	99.99870632	99.9977025
0.2	0.001977191	0.005180649	99.99802281	99.99481935
0.4	0.001875398	0.005847655	99.9981246	99.99415234

The resulting factors (Y_e / Y_w) obtained for native and SiOC impregnated membrane, along with separation factors are tabulated in Table 4.3.

Table 4.3: Comparison between separation factor of the native and SiOC impregnated membranes.

Sample vol (μL)	(Y_e/Y_w)		Separation factor, $\alpha_{e/w}$		%Enhancement in $\alpha_{e/w}$
	Native	SiOC Impregnated	Native	SiOC impregnated	
0.1	1.29×10^{-5}	2.30×10^{-5}	1.65×10^{-5}	2.92×10^{-5}	77.6
0.2	1.98×10^{-5}	5.18×10^{-5}	2.52×10^{-5}	6.59×10^{-5}	162
0.4	1.88×10^{-5}	5.85×10^{-5}	2.39×10^{-5}	7.44×10^{-5}	211.8
%Average enhancement in $\alpha_{e/w}$					150.5

For the native membrane, α ranged between 1.65×10^{-5} and 2.39×10^{-5}, whereas for the SiOC-impregnated membrane, α increased to 2.92×10^{-5} – 7.44×10^{-5} under identical operating conditions. While the overall ethanol permeation through both membranes remains extremely low, the SiOC-impregnated membrane achieves a markedly superior separation performance. Across the tested conditions, its ethanol–water separation factor is enhanced by roughly 150% on average relative to the native membrane.

These results confirm that incorporation of PDMS-derived SiOC particles substantially improves selective ethanol transport by modifying the sorption–diffusion behavior of the membrane.

4.7 Challenges encountered and resolutions implemented

The major challenges encountered during this study and the corresponding resolution attempts are summarized below.

- **Challenge:** Controlled one-sided particle incorporation.
  Resolution: Optimized swelling-assisted infusion enabled ~100 μm localized penetration.
- **Challenge:** Weak particle–polymer interaction.
  Resolution: SiOC surface functionalities improved anchoring within PDMS.
- **Challenge:** Reduced flux commonly associated with higher selectivity.
  Resolution: Modified interfacial transport maintained moderate permeability while improving selectivity.
- **Challenge:** Low permeation rate during pervaporation.
  Resolution: Extended 12 h operation enabled sufficient permeate collection.
- **Challenge:** Maintaining membrane stability under vacuum conditions.
  Resolution: Cross-linked PDMS membranes sustained prolonged reduced-pressure operation.

The remaining unresolved issues identified in this chapter provide directions for further improvement of PDMS-based membrane separation. These issues have been briefly noted in the Summary section and are further presented in the future work section of Chapter 7 within the wider scope of future research.

4.8 Literature comparison with the present work

The performance of the present SiOC-impregnated PDMS membrane is compared with relevant PDMS-based pervaporation studies to highlight its contribution and limitations, as summarized in Table 4.4.

Table 4.4: Literature summary of neat and modified PDMS membranes for ethanol–water separation.

Membrane / Modification	Key Findings	Relevance	Ref
Neat PDMS	Dilute feeds (0.3–3 wt% EtOH); moderate flux; baseline PDMS performance	Not applicable to high-EtOH feeds; low selectivity	[167]
Supported PDMS	Ethanol–water mutual diffusion quantified; MS modeling	Strong penetrant–penetrant interactions reduce performance	[205]
Zeolite–PDMS MMM	Up to 3.0 selectivity (65 wt% zeolite); filler improves separation	Performance highly dependent on dispersion; limited robustness	[206]
Zeolite–PDMS MMM	Selectivity up to 5× higher vs PDMS; stability tested	Degradation in fermentation broth; long-term decline	[207]
PDMS–PSS2 MMM	Nanoparticles enhance hydrophobicity and EtOH selectivity	Still a bulk-filler MMM; dispersion issues remain	[208]
Biochar-PDMS MMM	SF ≈11.9; Flux ≈227 $g \cdot m^{-2} \cdot h^{-1}$ at 10 wt% EtOH	Only dilute feeds; not comparable to 50% EtOH	[209]
Filled PDMS (real broth)	Stability evaluation in fermentation broth; real-feed impact major	Highlights need for robust MMMs under harsh conditions	[210]
One-sided SiOC-PDMS	≈150% separation factor gain; surface-localized SiOC domains;	New mechanism; evaluation under 50% EtOH feed	This Work

4.9 Summary

A relatively low temperature (550 °C) method to prepare SiOC particles with high surface area using commercially available PDMS is reported. Using a novel method, these particles are infused inside the PDMS membranes from one side, forming an asymmetric structure with localized inorganic domains. The infusion leads to increased surface hydrophilicity of

the face exposed for infusion, and a significantly altered pore size distribution in the membrane. As an application, the infused membranes are tested for pervaporation of 50-50 mixtures of ethanol and water. These infused membranes show enhanced permeability of ethanol despite an increased hydrophilicity on one side. The SiOC phase introduces surface silanol (Si–OH) and Si–O–C functionalities, enhancing the polarity and creating *water-affinitive microdomains* at the membrane surface. These sites preferentially interact with water molecules, forming a thin, quasi-liquid layer that locally alters the diffusion environment. Ethanol molecules, being partially miscible with water, experience enhanced diffusion through this mixed solid–liquid interface region compared to the dense PDMS matrix[201–203]. Simultaneously, SiOC incorporation increases free volume and reduces the effective diffusion resistance for ethanol within the bulk polymer[204].

Thus, while hydrophilicity increases due to SiOC incorporation, ethanol permeability is enhanced through a modified interfacial transport mechanism involving facilitated ethanol diffusion across a hydrated boundary region rather than direct permeation through a purely hydrophobic polymeric phase. A model is offered to explain these conflicting observations. Overall, the SiOC-impregnated PDMS membrane demonstrated a substantial improvement over the native membrane, yielding an average ~150% increase in ethanol–water separation factor. This corresponded to a transition from the order of 10^{-5} in the native membrane to higher values approaching 10^{-4} in the modified system, confirming the effectiveness of the surface-localized SiOC domains in tuning selective transport. However, the absolute separation factor and flux remained low. Therefore, improving separation efficiency, enhancing flux, assessing long-term membrane durability, and confirming SiOC retention during extended operation remain important aspects for future investigation.

Chapter 5: Millifluidic PDMS-CFI-Assisted Extraction and Mass Transfer Enhancement of Acetic Acid from a Biphasic Acetic Acid–Toluene (1:9 v/v) and Water System

5.1 Abstract

This study reports the fabrication and evaluation of a polydimethylsiloxane (PDMS)–based Coiled Flow Inverter (CFI) for enhanced mass transfer in continuous liquid–liquid extraction (LLE). The device was fabricated by casting PDMS around a removable helical polyvinyl alcohol (PVA) filament of 2.85 mm diameter and 270.1 mm length, producing a uniform coiled millichannel after template dissolution. The cured rod was sectioned and reconnected to generate four sequential 90° inversions, enabling periodic reorientation of the flowing phases and improved interfacial renewal under laminar flow.

The system was applied to extract acetic acid from an organic mixture containing 10% (v/v) acetic acid in toluene, with water used as the extracting phase. Two hydrodynamic variables—the aqueous-phase flow rate (Q_W) and organic-phase flow rate (Q_T) were varied across three representative combinations: (0.5–1), (0.5–3), and (1–1) mL min^{-1} (Q_W–Q_T). Outlet acetic acid concentration was quantified using refractive-index calibration and the overall volumetric mass-transfer coefficient ($k_{ov}a$) was obtained using an established empirical relation for curved millichannel systems.

Mass-transfer performance is strongly influenced by flow conditions. At constant Q_W = 0.5 mL min^{-1}, increasing Q_T from 1 to 3 mL min^{-1} increased $k_{ov}a$, whereas increasing Q_W from 0.5 to 1 mL min^{-1} at fixed Q_T = 1 mL min^{-1} produced a larger enhancement, nearly threefold, showing the dominant role of the aqueous-phase velocity in interfacial regeneration. The maximum $k_{ov}a$ achieved was 0.007145 s^{-1} under the highest water-flow condition. Overall, the study establishes PDMS-based CFIs as compact and scalable devices capable of significantly intensifying continuous LLE through controlled millichannel fluid dynamics.

Keywords: PDMS millifluidics, Coiled flow inverter, Liquid–liquid extraction, Mass transfer coefficient, Flow rate effects, Acetic acid-toluene-water system.

5.2 Phase behavior for the toluene–acetic acid–water ternary system

The ternary phase diagram is a compact graphical representation used to illustrate the liquid–liquid equilibrium behavior of the toluene–acetic acid–water system. Each vertex of the equilateral triangle corresponds to a pure component, while every point within the diagram represents a unique composition satisfying the condition that the sum of the components equals 100%. The grid shown in the diagram, in Figure 5.1, constructed at uniform composition intervals, helps in reading mixture compositions accurately and identifying the relative proportions of each component. For this system, toluene and water are strongly immiscible, while acetic acid acts as a partially miscible solute capable of interacting with both phases. Because of these intermolecular interactions, the system exhibits a distinct two-phase region, bounded by the binodal curve. Mixtures whose overall composition lies outside this envelope form a single homogeneous phase, whereas mixtures inside the envelope split into two liquid phases at equilibrium an organic (toluene-rich) phase and an aqueous (water-rich) phase.

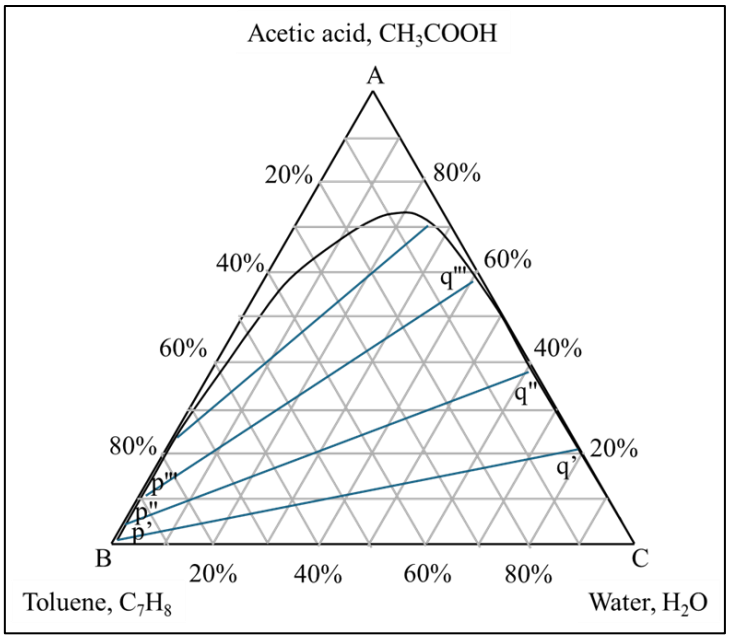

Figure 5.1: Ternary phase diagram for toluene-acetic acid and water.

The binodal curve represents the boundary separating one-phase and two-phase compositions. Its shape arises from the limited mutual solubility of toluene and water, and the ability of acetic acid to distribute unevenly between these two solvents. Within the two-phase region, the compositions of the two equilibrium phases are connected by tie-lines, which are plotted as slanted straight lines across the diagram. Each tie-line links a point on

the binodal curve representing the toluene-rich equilibrium phase with another point representing the water-rich phase. The slope of the tie-lines reflects the fact that the organic phase contains only small amounts of water but can dissolve moderate amounts of acetic acid, while the aqueous phase dissolves only traces of toluene but has a higher affinity for acetic acid.

The length and orientation of the tie-lines also provide important information for extraction calculations. Longer tie-lines indicate a greater difference in composition between the two phases and therefore stronger phase separation and more efficient solute distribution. As compositions move toward the plait point—the critical point at which the two phases become identical the tie-lines shorten and eventually collapse, representing the limit of phase separation.

5.3 Introduction

Liquid-liquid extraction (LLE) is a vital separation technique in which two miscible liquids are separated by employing a solvent that can selectively dissolve one of them. Some gains of this technique as separation of close boiling mixtures, metals purification, implementation at low temperature and high throughput favours LLE to work in various industries, including pharmaceuticals, petrochemicals, hydrometallurgy and environmental engineering etc., at low cost make it a possible alternative to distillation[211–213]. Since there are three or more components in LLE, therefore the equilibrium relationship presented on a triangular diagram is generally more complicated than for other separations.

The miniaturization of processes or reducing the size of unit operations is another substantial approach to acquire process intensification while optimizing the critical parameters including energy efficiency and mass transfer. Moreover, it boosts micro processing and overall productivity[95,214]. To accomplish this many studies have been performed over helical channels and CFIs made by transparent PVC tubing, wound around a square-shaped frame of cylindrical rods.

The coiled flow inverter (CFI) is an innovative reactor design that enhances mass transfer and mixing in various continuous flow processes with narrow residence time distribution, fast mixing, and improved safety compared to batch processes[97,215]. CFI modules demonstrate superior performance compared to straight tubes and helical coils, with increased Sherwood numbers for gas-liquid and liquid-liquid systems[216–218]. CFD

modeling has shown that CFIs can increase volumetric mass transfer coefficients by 1.5 times compared to straight channels[219]. The device's efficiency arises from flow inversion achieved by bending coiled tubes at 90° intervals, resulting in improved radial flow and reduced radial gradients[98,220].

Mixing in microfluidic devices is enhanced with curved design of channels where a secondary flow emerges due to centrifugal forces. Further chaotic advection occurred due to channel arrangement also improves mixing. The extent of these effects is measured by a dimensionless Dean number, higher the Dean number, better the mixing performance[221–223]. It is also to be noted that surface tension is a dominant and major player as compared to gravitational and inertial forces in LLE through millifluidic devices[224].

The evaluation of mass transfer performance in liquid–liquid extraction systems is often carried out through empirical correlations for the overall volumetric mass transfer coefficient $k_{ov}a$[225]. This parameter integrates both the intrinsic transport properties of the fluids and the interfacial area generated under specific flow conditions. Since liquid–liquid extraction involves the transfer of solute molecules from a dispersed to a continuous phase, accurate determination of $k_{ov}a$ is essential for predicting separation efficiency, optimizing operating parameters, and scaling up laboratory-scale studies to industrial applications. Empirical relations are particularly valuable because they account for the complex interplay of hydrodynamics, diffusivity, and phase behavior that cannot be easily captured by purely theoretical models. Several studies have reported such correlations for liquid–liquid flows in micro- and millifluidic devices, highlighting the role of flow regime, channel dimension, and operating parameters on interfacial mass transfer. For instance, [226] examined slug-flow microreactors for predicting $k_{ov}a$ in different solvent systems, while, [227] demonstrated efficient extraction using capillary microreactors. Further [228] analyzed phase inversion phenomena in small channels and linked them to enhanced mass transfer. These studies collectively establish empirical models as indispensable tools for process design and intensification in liquid–liquid extraction systems.

This work investigates the potential of a PDMS-CFI to improve the extraction process, providing an analysis of the mass transfer kinetics involved due to flow rate variation between acetic acid-toluene mixture and water. Toluene and water are immiscible, while acetic acid is miscible with both toluene and water. Acetic acid can dissolve in both solvents due to its polar carboxyl group and nonpolar hydrocarbon tail, which allows it to interact

with both polar (water) and nonpolar (toluene) molecules. A biphasic mixture of acetic acid and toluene (1:9 v/v) was prepared, and acetic acid was extracted into water by passing the system through the CFI.

5.4 Research gaps

Liquid–liquid extraction systems based on batch vessels and straight continuous channels often exhibit restricted interfacial renewal and moderate mass-transfer performance. Although coiled and curved channels can enhance mixing through Dean-vortex-induced secondary flow, their implementation in flexible PDMS-based millifluidic extraction systems remains limited.

Accordingly, the important research gaps are:

- Batch and straight-channel extraction systems provide limited interfacial renewal and moderate mass-transfer enhancement.
- Hydrodynamic intensification using coiled and curved channels has been studied mainly in rigid glass and metal systems, while PDMS-based CFI extraction devices remain insufficiently explored.
- The application of CFIs for continuous acetic-acid extraction and the influence of flow inversion on extraction performance require further investigation.
- Continuous-flow mass-transfer behavior and operational feasibility of PDMS-CFI systems in organic–aqueous environments containing solvents, such as, toluene remain insufficiently studied.

Thus, this chapter addresses these gaps by developing a transparent PDMS-CFI device and evaluating its extraction and mass-transfer performance for continuous acetic-acid extraction.

5.5 Experimental section

5.5.1 Fabrication of coiled flow inverter (CFI)

Initially, Sylgard 184 PDMS solution was prepared by mixing its silicone base elastomer and curing agent (10wt%). Using a PVA filament of diameter 2.85 mm and length 270.1 mm, a spiral-helical coil with mean diameter of 11.8 mm was created and centrally

immersed into the prepared PDMS solution, kept in a cylindrical tube. The whole assembly was degassed and let it cure for two days at room temperature. The resulting cylindrical PDMS casting was removed from the tube and put in boiled water bath. The embedded PVA coil, inside cured PDMS, was dissolved by blowing pressurized boiled water manually, leaving a required hollow spiral channel. Subsequently, the cylindrical PDMS rod was divided into four equal segments, arranged at 90 degrees, and interconnected using silicone tubes to fabricate the desired Coiled Flow Inverter (CFI). A schematic representation of the fabricated CFI is shown in Figure 5.2 and the actual image has been presented earlier in Figure 3.3 (b).

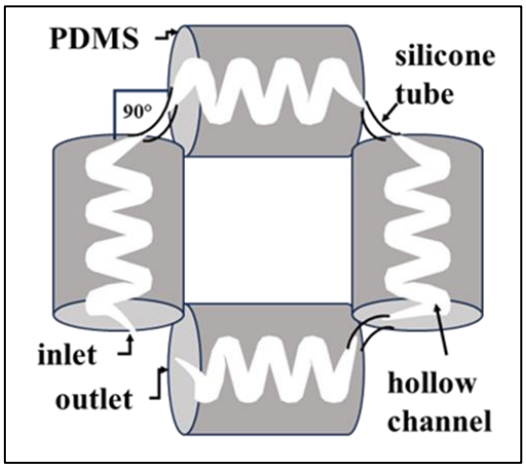

Figure 5.2: Schematic representation, showing internal helical grooving, connected via silicone tubes.

5.5.2 Instrumentation

Two syringe pumps (New Era pump 100) with individually controlled flowrates of aqueous and organic phases are used. The test fluids selected for mass transfer study are toluene with 10% acetic acid by volume as the organic phase and distilled water as the aqueous phase, maintained with flow rates of Q_T and Q_W respectively. A T-section connector at initial mixing of the liquids has been used before inlet to CFI. As the mixing progresses in CFI, the component of acetic acid from toluene-acetic acid mixture is transferred into water and collected from the outlet. The experiment has been performed at different flow rates of Q_T and Q_W ranging from 0.5 mL/min to 3 mL/min. A refractometer, model Rx-7000i (made in Japan) was used to analyze the refractive indices of the aqueous phase collected from the outlet of CFI. A schematic representation of the experimental setup is shown in Figure 5.3.

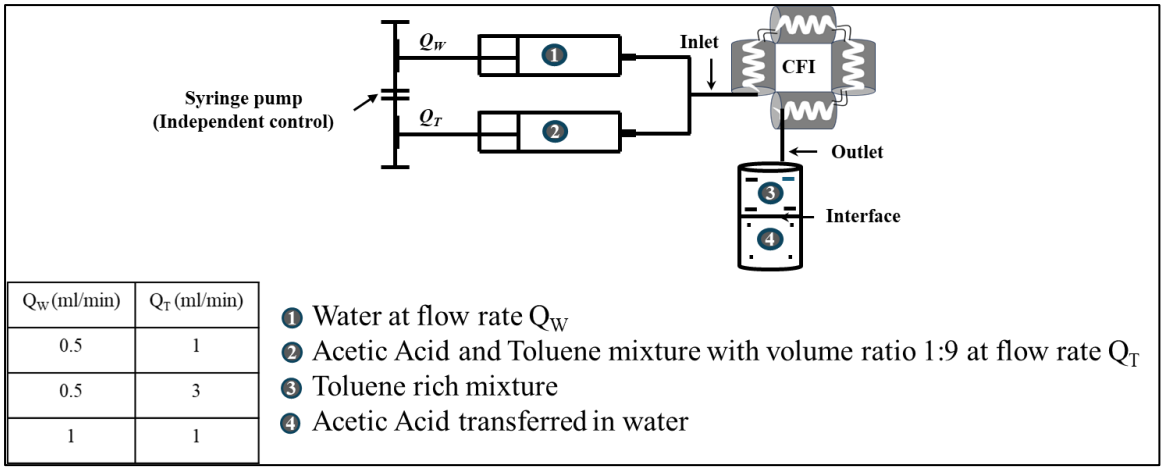

Q_W (ml/min)	Q_T (ml/min)
0.5	1
0.5	3
1	1

1. Water at flow rate Q_W
2. Acetic Acid and Toluene mixture with volume ratio 1:9 at flow rate Q_T
3. Toluene rich mixture
4. Acetic Acid transferred in water

Figure 5.3 Schematic representation of experimental set-up for extraction process of acetic acid at different flow rates.

5.5.3 Governing equation for determination of overall mass transfer coefficient

An empirical relation is used to calculate the overall mass transfer coefficient, $k_{ov}a$ (s^{-1}) which is given by equation (5.1) [225] below:

$$k_{ov}a = -\frac{1}{1+m\frac{Q_W}{Q_T}}\left[ln\frac{mC_{T.in}+m\frac{Q_W}{Q_T}C_{W.in}-\left(1+m\frac{Q_W}{Q_T}\right)C_{W.out}}{mC_{T.in}+m\frac{Q_W}{Q_T}C_{W.in}}\right]\frac{Q_W}{LA} \qquad (5.1)$$

where, $\boldsymbol{a}$ is transfer area per unit volume (m^2/m^3)

$\boldsymbol{C_{T.in}}$, initial concentration of acetic acid in toluene at the inlet, (m^3 of acetic acid/m^3 of pure toluene) = 0.111

$\boldsymbol{C_{W.in}}$, initial concentration of acetic acid in water at the inlet, (m^3 of acetic acid/m^3 of pure water) = 0

$\boldsymbol{L}$, length of the channel = 313.5 mm

$\boldsymbol{A}$, cross-sectional area of the inner channel = 6.376 mm^2

$\boldsymbol{m}$, slope of line of plot between equilibrium concentration of acetic acid in water ($\boldsymbol{C_w^*}$) and concentration of acetic acid in toluene ($\boldsymbol{C_T}$) = 4.05 [225]

$\boldsymbol{C_{W.out}}$, concentration of AA in water at outlet (m^3 of acetic acid/m^3 of pure water).

5.6 Results and discussion

5.6.1 Refractive index measurements

With the known concentration (0, 5, 7, 10, 15 and 20%) of acetic acid in water (20 mL) and their respective refractive indices values, a calibration curve equation is obtained and given by

$$y = 17.114x - 22.774 \quad (5.2)$$

From this equation, the concentration of acetic acid transferred in water from the biphasic mixture of toluene and acetic acid, at outlet of CFI, can be estimated when processed through it at different flow rates of Q_W and Q_T. With each set of flow rates of Q_W and Q_T, 4 refractive indices values of the extract were measured, obtained after processing through CFI. The collection time interval of RI was 10 s. To calculate the concentration of extraction, the average of these four RI values from each set of flow rates was taken and presented in Table 5.1. This way, the concentration of acetic acid at outlet ($C_{W.out}$) from 3 sets of ($Q_W - Q_T$) flow rates, (0.5-1), (0.5-3) and (1-1) mL/min was obtained from equation (5.2) and presented in the same Table 5.1.

Table 5.1: Average RI values of extract and estimated concentration of acetic acid at outlet.

Q_W (mL/min)	Q_T (mL/min)	Measured refractive index (RI) value				RI (Avg.)	$C_{W.out}$
		@ 10 s	@ 20 s	@ 30 s	@ 40 s		
0.5	1	1.33709	1.33713	1.33723	1.33735	1.33720	0.11084
0.5	3	1.34287	1.34291	1.34293	1.34295	1.34292	0.20873
1	1	1.33562	1.33578	1.33587	1.33591	1.33580	0.08688

5.6.2 Calculation of overall mass transfer coefficient

The resulting overall mass transfer coefficient of AA in water was estimated using the empirical relation (5.1), are tabulated in Table 5.2.

Table 5.2 Overall mass transfer coefficient, $k_{ov}a$ obtained at different set of flow rates.

Q_W (mL/min)	Q_T (mL/min)	$k_{ov}a$ (s^{-1})
0.5	1	0.002191
0.5	3	0.004344
1	1	0.007145

5.7 Challenges encountered and resolutions implemented

During the design, fabrication, and operation of the PDMS-based CFI for acetic acid extraction, several experimental challenges were encountered. The key challenges and the measures adopted to address them are listed below.

- **Challenge:** Complete removal of the helical PVA filament without channel damage or residue formation.
  Resolution: A gradual warm-water dissolution protocol was optimized to obtain smooth and defect-free channels.
- **Challenge:** Maintaining stable two-phase flow under varying flow-rate ratios.
  Resolution: High-precision syringe pumps and controlled inlet arrangements were employed to stabilize phase flow.
- **Challenge:** Maintaining channel transparency and dimensional uniformity during fabrication.
  Resolution: PDMS solution complete de-gasing, controlled casting and curing conditions were adopted to ensure smooth channel surfaces.
- **Challenge:** Swelling of PDMS upon exposure to toluene could distort the coiled channel geometry.
  Resolution: Extended curing and thermal post-treatment were used to stiffen the PDMS network and reduce solvent-induced deformation.

The unresolved points arising from this chapter are linked to further development of continuous liquid–liquid extraction systems and have been briefly noted in the Summary section, with further discussion carried forward to Chapter 7 as part of the future work.

5.8 Literature comparison with the present work

To position the present system with respect to existing studies, a comparison with relevant extraction and mass transfer reports is provided in Table 5.3.

Table 5.3: Comparison of millireactor/microreactor geometries and their influence on mass transfer performance in liquid–liquid extraction systems.

Device / Geometry	System	Key Findings	Relevance	Ref
Milli-channel with 90° bend	Acetic acid-toluene / water	Bend enhanced mass transfer	Curvature/flow disturbance improves acetic-acid extraction	[229]
LLE equilibrium cell	Water-acetic acid-toluene	LLE data at 288.2–313.2 K; extraction factor ~100.	Thermodynamic basis for acetic-acid partitioning	[230]
Capillary microchannels (0.5–2 mm)	LLE systems	Reported $k_L a$ up to ~0.29 s^{-1}	Strong dependence of mass transfer on channel geometry	[231]
Microstructured reactors (review)	Gas–liquid / liquid–liquid systems	Flow regime governs mass transfer (slug, annular, dispersed)	Microreactor-based mass transfer intensification	[232]
PFA tube-CFI + phase separator	Organic–aqueous systems	~20% higher extraction vs straight tube	Direct benchmark for CFI-based extraction; different system	[233]
Straight, bent, and helical microchannels	Toluene–acetic acid / water	$k_{ov}a$ range 0.005–0.79 s^{-1}, enhanced in curved channels	Confirms curvature-induced intensification relevant to CFI	[234]
T-junction microchannel	Liquid–liquid system	Individual phase mass-transfer coefficients increase with flow rate	Supports role of flow dynamics in mass transfer enhancement	[235]
PDMS-based CFI	Acetic acid–toluene (1:9 v/v) / water	$k_{ov}a$ = 0.007145 s^{-1}; strong dependence on aqueous flow rate	PDMS-based CFI system for extraction; flexible, transparent, compact reactor	This Work

5.9 Summary

The present study demonstrates the successful fabrication and application of a PDMS-based Coiled Flow Inverter (CFI) for continuous liquid–liquid extraction of acetic acid from an organic mixture of 10% acetic acid in toluene by volume. The CFI was fabricated using a

dissolvable helical PVA filament, producing a coiled channel geometry that was subsequently segmented and reconnected to introduce periodic flow inversions. This configuration repeatedly reorients the interacting phases, promoting interfacial renewal and improving phase contact within a compact flow system. Extraction experiments at various flow conditions revealed that mass transfer performance is strongly influenced by flow dynamics. When the aqueous phase (water) flow rate was maintained at 0.5 mL/min, tripling the organic phase (acetic acid–toluene mixture) flow rate from 1 mL/min to 3 mL/min led to approximately a twofold increase in extraction efficiency. In contrast, doubling the water flow rate from 0.5 mL/min to 1 mL/min at a constant organic flow rate resulted in nearly a threefold improvement. This indicates that the aqueous phase flow rate has a more dominant influence on enhancing mass transfer than the organic phase. The maximum overall volumetric mass transfer coefficient ($k_{ov}a$) observed was 0.007145 s^{-1}, corresponding to the highest water flow condition. These findings validate the effectiveness of the CFI design in improving separation efficiency through enhanced fluid dynamics and confirm its potential as a compact and scalable solution for continuous liquid–liquid extraction processes. However, long-term solvent compatibility, continuous operational stability, phase separation, and scale-up of the PDMS-CFI system remain important aspects for future investigation.

Chapter 6: Fabrication and Characterization of Phase Change Material–Embedded PDMS Membranes for Thermal Energy Storage

6.1 Abstract

This study investigates the fabrication and thermal performance of polydimethylsiloxane (PDMS)–based composite membranes incorporating stearic acid (SA) as a phase change material (PCM) for thermal energy storage (TES). Membranes were fabricated via the doctor-blading technique by systematically varying two key degrees of freedom: SA loading (5.7–23.3 wt%) and tetrahydrofuran (THF) solvent volume (2 and 4 mL), producing films of ~1.35 mm thickness. The influence of these parameters on thermal behavior was assessed using Fourier transform infrared spectroscopy (FTIR), differential scanning calorimetry (DSC), and transient temperature–time cooling analysis under insulated and non-insulated conditions.

FTIR confirmed successful incorporation of SA into the PDMS matrix with negligible residual solvent. DSC analysis showed stable phase transition temperatures (melting ~56 °C; crystallization ~52–53 °C), with latent heat increasing from 2.7 to 34.3 J g^{-1} as SA loading increased. However, latent heat utilization efficiency, calculated from melting enthalpy (ΔH_m), increased from ~24% to a maximum of ~80% at ~19.5 wt%, followed by a slight decline at higher loading, indicating confinement-limited crystallization. Thermal analysis revealed a significant reduction in cooling rate from ~2.0 °C/min (pure SA) to ~0.29 °C/min for composite membranes and an increase in thermal time constant from ~1000 s to ~6300 s, demonstrating enhanced thermal inertia due to the insulating PDMS matrix.

Overall, the study establishes a clear processing–structure–property relationship and identifies ~19.5 wt% SA as the optimal composition for maximizing thermal storage efficiency and controlled heat release.

Keywords: Phase change material, Stearic acid, PDMS-PCM composite membrane, Differential scanning calorimetry, Thermal retention, Molecular confinement

6.2 Introduction:

The increasing global demand for efficient energy utilization has intensified the focus on advanced thermal management systems and energy storage technologies. Among these, thermal energy storage (TES) has emerged as a pivotal strategy to balance the mismatch between energy supply and demand, particularly in applications that involve intermittent energy sources, such as, solar and wind. TES systems function by absorbing, storing, and releasing heat over time, providing heating or cooling when needed, thus enhancing energy efficiency and sustainability across a wide range of sectors including buildings, electronics, textiles, and renewable energy integration [236–238].

A promising class of materials for TES systems is known as phase change materials (PCMs). These materials possess the intrinsic capability to absorb or release substantial amounts of heat during their phase transition, most commonly between solid and liquid states. This latent heat storage process occurs at nearly constant temperature, making PCMs highly suitable for applications where temperature regulation is crucial. PCMs are highly effective in thermal energy storage systems due to their ability to absorb and release latent heat during phase transitions. As illustrated in Figure 6.1, during the daytime, when the ambient temperature is higher than the comfort temperature, the PCM undergoes an endothermic process, absorbing heat and transforming from solid to liquid.

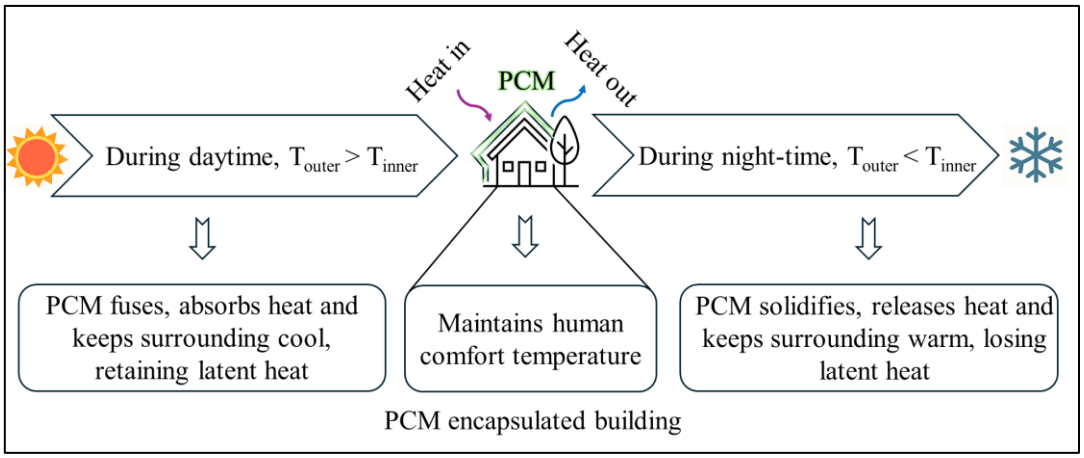

Figure 6.1: Schematic of PCM-based thermal energy storage through heat absorption during the day and release at night.

This process helps in storing excess thermal energy and prevents overheating of the surrounding environment. Conversely, during nighttime, when the temperature drops below the desired range, the PCM solidifies through an exothermic process, releasing the stored heat back into the environment. This reversible solid–liquid phase transition allows

PCMs to act as a thermal buffer, maintaining a stable and comfortable temperature range. Such characteristics make PCMs promising candidates for applications in building insulation, solar energy storage, and thermal management systems.This reversible thermal behaviour enables PCMs to provide both passive and active thermal control, offering improved temperature stability, energy conservation, and system reliability [239,240].

In recent years, extensive research has been devoted to identifying suitable PCMs that exhibit high latent heat, chemical and thermal stability, non-toxicity, low vapor pressure, and compatibility with various matrices and encapsulating materials [239]. Among the various organic PCMs investigated, SA has gained considerable attention due to its unique thermophysical properties [241]. As a saturated long-chain fatty acid, SA exhibits a high latent heat of fusion, a melting point in the desirable range of 57.4–73.5 °C, excellent chemical stability, and reusability over multiple thermal cycles [242–245]. These characteristics make SA a favourable candidate for medium-temperature thermal energy storage applications, such as, in solar heating systems, smart clothing, food packaging, and building materials [246–249]. The feasibility of incorporating stearic acid (SA) into polymeric matrices to develop composite structures with enhanced stability has been well demonstrated in earlier studies. For example, polyvinyl alcohol (PVA) assisted PDMS–SA nanofibrous mats were fabricated through electrospinning technique with improved mechanical behavior for selective filtering applications [175]. Similarly, SA has been supported in PVA films to improve shape stability and thermal cycling performance [250], while polyethylene glycol (PEG) has been blended with SA to form microcapsules with broadened phase transition ranges and enhanced thermal reliability [251]. In addition, biopolymer-based matrices, such as, chitosan, alginate, and cellulose derivatives have been explored for SA encapsulation, yielding sustainable and thermally reliable composites for thermal energy storage applications [252].

However, one of the major challenges in employing PCMs in practical TES systems lies in their tendency to leak in the liquid phase, low thermal conductivity, and difficulty in integration with structural components [253–255]. To address these limitations, recent approaches have focused on embedding or encapsulating PCMs within a supporting matrix, such as, polymers, porous scaffolds, or fibrous structures, to form stable composites [256–258]. Among these, polymer-based PCM composites are of particular interest due to their design flexibility, lightweight nature, ease of fabrication, and processability [259]. In this context, polydimethylsiloxane (PDMS), a silicone-based elastomer, stands out as a highly

promising matrix for PCM encapsulation. PDMS exhibits excellent thermal and oxidative stability, mechanical flexibility, chemical inertness, and transparency, making it suitable for integration with light-driven or thermally responsive systems [2,260]. Moreover, its hydrophobicity, tunable porosity, and compatibility with a wide range of solvents allow for efficient loading and stabilization of PCMs, such as, stearic acid [17,261–263].

In the present work, stearic acid is incorporated into a PDMS matrix to fabricate composite membranes for TES applications. PDMS, as a thermally stable and flexible polymer, serves as the host matrix, while tetrahydrofuran (THF) is employed as the processing solvent to aid in uniform dispersion and membrane formation. The fabrication process was carried out using the doctor-blading technique, with SA concentrations ranging from 5.7 wt% to 23.3 wt% relative to PDMS and varying THF volumes (2 mL and 4 mL) to examine the effect of solvent content on membrane morphology and performance.

6.3 Research gaps

Phase change material (PCM)-based thermal energy storage systems commonly use paraffins, fatty acids, hydrated salts, microcapsules, or rigid composites. Although PCMs provide high latent heat storage, their practical use is often limited by leakage, low flexibility, shape instability, and low thermal conductivity, which can restrict heat charging and discharging rates. Although PDMS offers flexibility, thermal stability, and chemical inertness, its use as a flexible host matrix for directly embedded fatty-acid PCMs, such as, stearic acid remains comparatively less explored. Therefore, important research gaps exist in:

- Developing a simple fabrication route for directly embedding stearic acid into flexible PDMS membranes.
- Understanding the effect of stearic acid loading on latent heat storage, heat retention, and thermal response.
- Evaluating heat-release behavior and thermal regulation potential of PDMS–PCM membranes.

This chapter addresses these gaps by fabricating SA–PDMS membranes using doctor-blading and evaluating their phase transition behavior, latent heat storage, cooling response, and thermal time constant at different PCM loadings.

6.4 Membrane synthesis and nomenclature

Initially 3g of PDMS solution (cross-linked 10 wt%) of Sylgard 184 was prepared in 8 different beakers. In each of the 4 beakers of PDMS solution, 2 ml of THF was mixed, while 4 ml of THF was mixed in the PDMS solution of the rest 4 beakers. Beakers with 2 ml THF were mixed with 0.2, 0.4, 0.6 and 0.8 g stearic acid, while those with 4 ml THF, 0.4, 0.6, 0.8 and 1 g of stearic acid were mixed slowly and stirred simultaneously. In this way, with the stearic acid content ranging from 0.2 to 1 g, the percentage composition of stearic acid varied from 5.7wt% to 23.3wt%. These solutions were distributed over different glass slides using a clean blade by shear casting known as doctor-blading method (Figure 6.2).

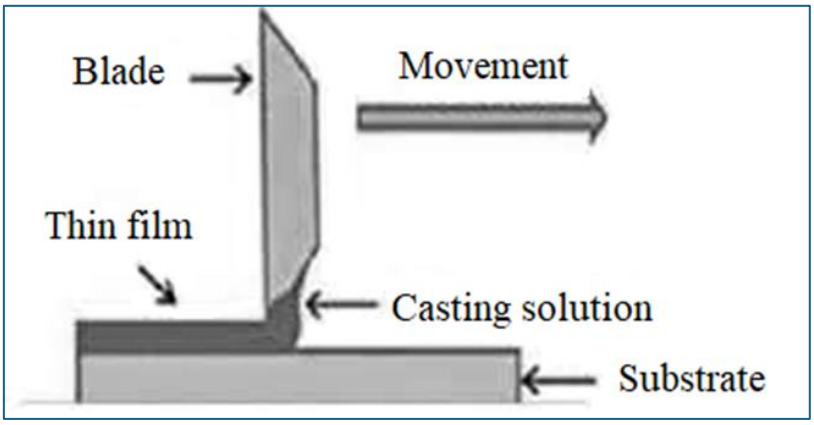

Figure 6.2: Doctor-blading method of membrane fabrication.

These samples were kept in oven at 40 °C for 2 days for drying and membrane formation. The thickness of the membrane achieved is 1.35 mm. A nomenclature of the membranes is adopted, such as, a membrane with 2 ml THF and 5.7wt% stearic acid content was named as M_T2_SA5.7 and similarly others are named.

6.5 Results and discussion

6.5.1 FT-IR characterization

The FTIR results of the stearic acid (SA) impregnated PDMS membranes are shown in Figure 6.3. The results were compared with the FT-IR pattern of their neat form in Figure 6.4. The characteristic absorption bands observed in the spectra correspond to the distinct functional groups of the constituent materials—PDMS, stearic acid, and tetrahydrofuran (THF). The C–H stretching vibrations for PDMS appear prominently at 2963 cm^{-1}, while the C–H stretch due to THF and SA are detected at 2917 cm^{-1} and 2848 cm^{-1}, respectively.

The presence of these bands confirms the coexistence of all three materials during initial membrane formation.

Notably, strong bands corresponding to C=O stretching (1698 cm^{-1}) and C–O bending (1464 cm^{-1}) are attributed to stearic acid, which indicate its successful incorporation in the PDMS matrix. Additionally, the presence of Si–CH_3, Si–O–Si, and other methyl-siloxane vibrations, specifically at 1059 cm^{-1}, 1011 cm^{-1}, and 789 cm^{-1}, respectively, further confirms the structural identity of PDMS in the composite. These characteristic peaks are well-aligned with known PDMS spectral fingerprints, establishing the preservation of its molecular framework post-membrane fabrication.

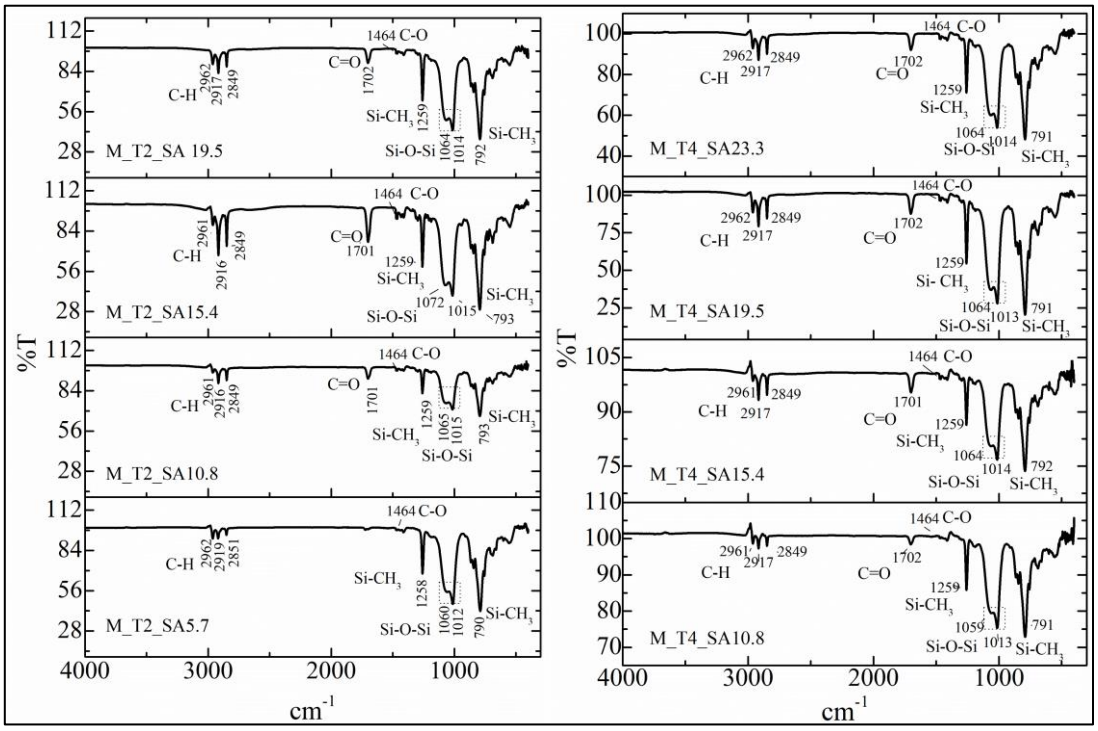

Figure 6.3: FT-IR results of membranes showing functional groups and bonding.

THF, used as a solvent, shows minimal spectral presence in the final membranes, suggesting that it is almost completely evaporated during the drying process. Any peak shifting observed in the FTIR spectra is primarily attributed to interactions between SA and PDMS, such as, hydrogen bonding or chain entanglement, rather than the presence of THF. However, the increasing stearic acid content across the membrane samples does not lead to a consistent trend in peak shifts. Instead, the variations in peak positions are scattered and show either no change or a minor increase of ~1 cm^{-1} in the functional group region (above 1500 cm^{-1}), while in the fingerprint region (below 1500 cm^{-1}), the peak positions remain mostly constant or shift slightly downward.

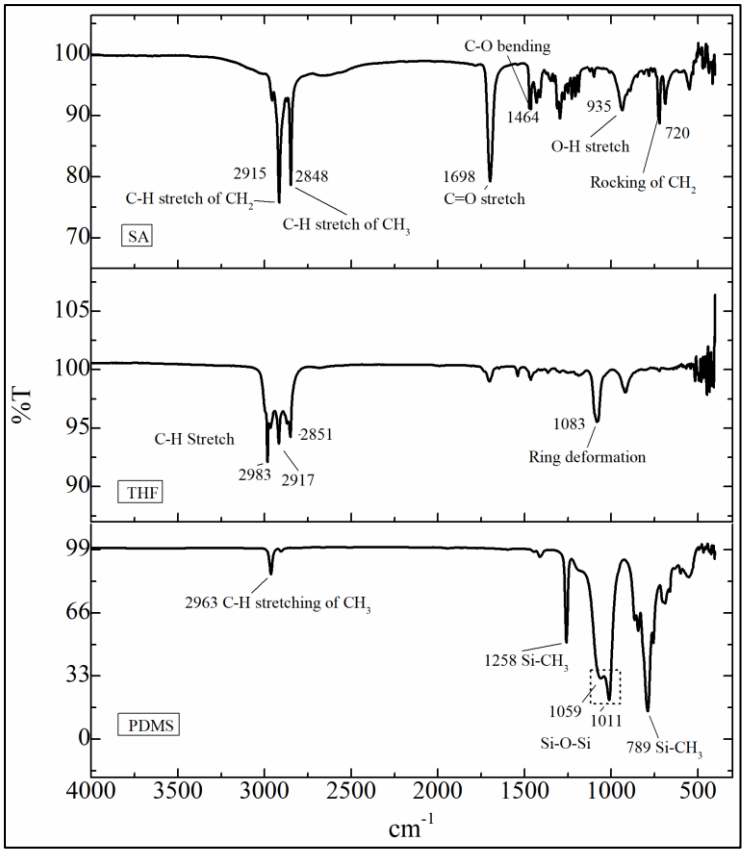

Figure 6.4: Figure: FTIR pattern for neat PDMS, THF and SA powder.

These irregular shifts suggest that molecular interactions vary non-linearly with SA loading and are likely influenced by the physical distribution, crystallinity, or confinement of SA within the PDMS network rather than by systematic chemical bonding changes. Overall, the FTIR results validate the successful incorporation and structural retention of PDMS and SA in the membranes, while also confirming that THF plays a transient role during fabrication and has negligible presence in the final product.

6.5.2 DSC characterization

The DSC results provide insights of the melting and cooling characteristics (at 2 °C min^{-1}) of the composite membranes as shown in Figure 6.5. The onset and peak melting temperatures remained relatively stable across all samples, with only slight variations observed. This stability indicates that the fundamental thermal properties of stearic acid are preserved within the polymeric matrix and that the incorporation process does not significantly affect the PCM's intrinsic phase transition behavior. Notably, in the T2 membranes, a slight decrease in onset temperature at higher SA concentrations suggests limited PCM crystallinity or constrained phase transition behavior due to reduced solvent content during fabrication, which may hinder effective dispersion.

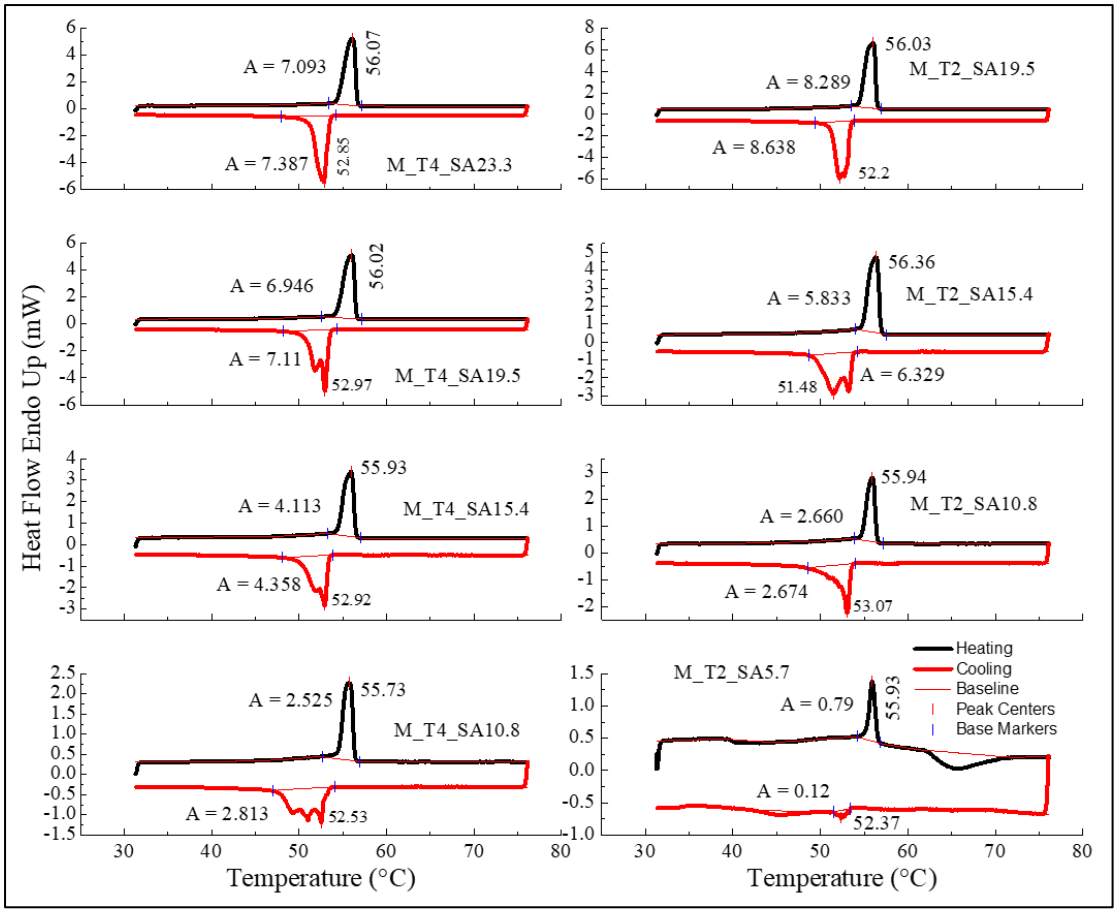

Figure 6.5: DSC thermograms of the prepared composite membranes.

The analysis reveals that the phase transition temperatures of stearic acid remain largely unaffected by encapsulation within PDMS, with melting occurring at ~56 °C and crystallization at ~52–53 °C. The observed supercooling (~3–4 °C) and consistent enthalpy values confirm the thermal reliability of the composite membranes.

The peak areas obtained from various curves were used to compute the melting and cooling enthalpies per weight of loaded sample (δH) and per weight of SA fraction (δH wt%), represented in Figure 6.6. A consistent increase in the enthalpy of melting was observed with increasing SA content for both T2 and T4 samples, indicating enhanced thermal energy storage capacity due to the higher availability of the latent heat-storing phase change material (PCM). Among the two formulations, the T4 membranes exhibited a significantly higher enthalpy compared to T2 at all SA loadings, suggesting that increased solvent volume facilitates better dispersion and distribution of stearic acid within the PDMS matrix.

The enthalpy of fusion increases with increasing stearic acid loading for both T2 and T4 membranes, as expected due to the higher fraction of active phase change material. However, enthalpy analysis reveals that the efficiency of latent heat utilization does not

increase proportionally and reaches a maximum around ~19–20 wt%. Beyond this composition, only marginal gains in total enthalpy are observed, indicating the onset of confinement-limited crystallization. The T4 membranes consistently exhibit higher enthalpy values than T2, confirming that increased solvent volume enhances PCM dispersion and improves thermal performance. The slight deviation observed at intermediate loading (~15 wt%) suggests a transitional regime associated with redistribution and partial confinement of PCM within the PDMS matrix.

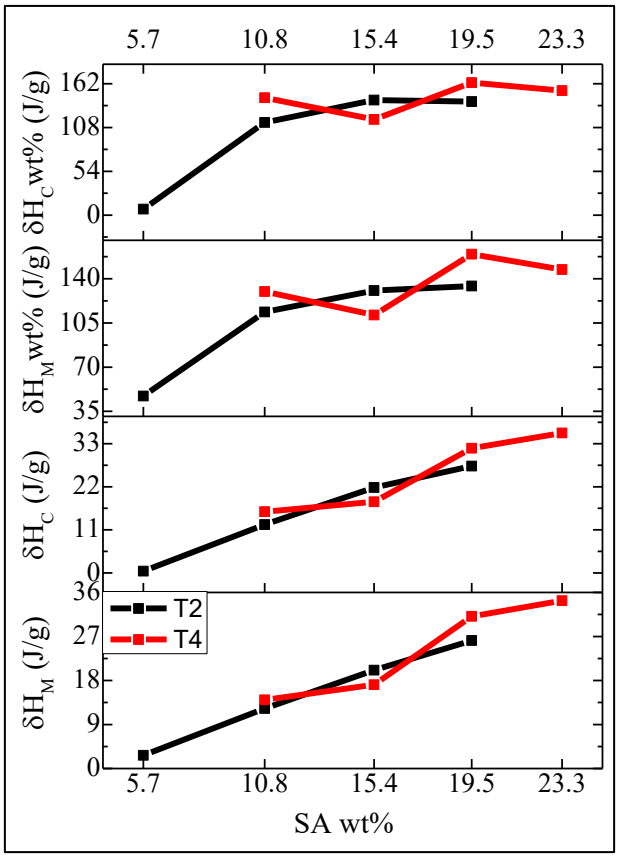

Figure 6.6: Cooling and melting enthalpy results of PDMS membranes fabricated with various stearic acid contents at 2 and 4 ml of THF.

Overall, the DSC results confirm that the enthalpy of fusion is strongly dependent on SA loading and is significantly influenced by the amount of THF used during membrane fabrication. The higher solvent volume (T4) not only supports more uniform distribution of the PCM but may also allow for better penetration and entrapment within the PDMS network, thereby improving latent heat retention. These findings highlight the importance of solvent-mediated processing in tailoring the thermal performance of PCM-impregnated polymeric membranes. The preserved melting behavior and enhanced enthalpy make these composite membranes promising candidates for latent heat-based thermal energy storage applications, particularly when fabricated under optimized solvent conditions.

6.5.3 Latent heat utilization efficiency

The latent heat utilization efficiency (η) of the composite membranes was evaluated to quantify the effectiveness of stearic acid (SA) in contributing to thermal energy storage. The efficiency was calculated as the ratio of experimentally measured enthalpy to the theoretical enthalpy based on SA content:

$$\eta = \frac{\Delta H_{composite}}{w \times \Delta H_{SA,\ pure}} \times 100 \qquad (6.1)$$

where w is the weight fraction of SA and $\Delta H_{SA,\ pure} \sim 200$ J g^{-1} is the latent heat of pure SA.

The efficiency (η) computed using the melting enthalpy (ΔH_m) values derived from DSC thermogram, plotted as a function of stearic acid loading are shown in Table 6.1.

Table 6.1: Latent heat utilization efficiency of PDMS–SA composite membranes for (ΔH_m) values.

SA (wt%)	ΔH_m (T2) (J g^{-1})	η (T2) (%)	ΔH_m (T4) (J g^{-1})	η (T4) (%)
5.7	2.7	**24**	–	–
10.8	12.3	**57**	14.0	**65**
15.4	20.1	**65**	17.1	**56**
19.5	26.2	**67**	31.1	**80**
23.3	–	–	34.3	**74**

The calculated efficiencies range from ~24% at low SA loading (5.7 wt%) to a maximum of ~80% at 19.5 wt% for the T4 series. A consistent increase in efficiency is observed with increasing SA content up to ~19–20 wt%, indicating improved crystallization and effective participation of PCM in latent heat storage. Beyond this composition, a slight decline in efficiency is observed (e.g., ~74% at 23.3 wt%), suggesting the onset of confinement-limited crystallization within the PDMS matrix. The T4 membranes exhibit consistently higher efficiency compared to T2 across comparable compositions, confirming that increased solvent volume enhances PCM dispersion and reduces molecular aggregation. At lower SA loadings, reduced efficiency is attributed to insufficient nucleation and isolated PCM domains, while at higher loadings, reduced molecular mobility and spatial confinement hinder complete crystallization.

These results demonstrate that latent heat utilization is governed by a balance between PCM loading and available free volume within the polymer matrix, with an optimal composition around ~19.5 wt% that maximizes thermal energy storage efficiency.

6.5.4 SA content–dependent enthalpy saturation in PDMS

The molecular-volume occupancy of stearic acid (SA) in PDMS was quantified for SA concentrations ranging from 5.7 to 23.3 wt%. The intrinsic pervaded volume of a single SA molecule was calculated from its molecular diameter (2.4–2.7 nm) using the relation, $V=4/3\ \pi r^3$, yielding 7.24×10^{-21} to 1.03×10^{-20} cm³ per molecule. This intrinsic value remains constant across all compositions. Using the number of SA molecules determined from the mass-to-molar-mass ratio, the total molecular occupancy increased proportionally with SA loading (from ~3×10^{-6} to ~2×10^{-5} cm³), as shown in the Table 6.2.

Table 6.2: Calculated intrinsic SA molecular volume and corresponding number of molecules at each SA wt%, used to evaluate cumulative molecular occupancy in PDMS and its link to enthalpy saturation near ~20 wt%.

SA (wt%)	No. of SA molecules (N)	Total intrinsic occupancy (cm³)	PDMS volume available per SA molecule (cm³)
5.7	4.23×10^{20}	$3.06\times10^{-6} – 4.36\times10^{-6}$	8.08×10^{-21}
10.8	8.46×10^{20}	$6.12\times10^{-6} – 8.72\times10^{-6}$	4.04×10^{-21}
15.4	1.27×10^{21}	$9.00\times10^{-6} – 1.31\times10^{-5}$	2.69×10^{-21}
19.5	1.69×10^{21}	$1.22\times10^{-5} – 1.74\times10^{-5}$	2.03×10^{-21}
23.3	2.12×10^{21}	$1.54\times10^{-5} – 2.18\times10^{-5}$	1.61×10^{-21}

To evaluate how these molecules are accommodated within the polymer matrix, the total PDMS volume (~3.42 cm³) was divided by the number of SA molecules to determine the PDMS free volume available per SA molecule. This available volume decreases from 8.08×10^{-21} cm³ at 5.7 wt% to 1.61×10^{-21} cm³ at 23.3 wt%, indicating progressively tighter spatial confinement at higher SA loadings. Despite this decrease, even at the highest SA loading the total occupancy remains only a small fraction of the overall PDMS matrix volume, showing that SA molecules remain well-dispersed and not densely packed. This spatial accommodation explains the DSC trend: at low concentrations, the relatively large free volume permits local molecular mobility, enabling small ordered domains, being represented in schematic diagram, in Figure 6.7. As loading approaches ~20 wt%, the

reduced free volume constrains molecular rearrangement, limiting the growth of crystalline regions and causing the enthalpy per wt% SA to plateau. Pure SA exhibits far higher enthalpy because it crystallizes without confinement.

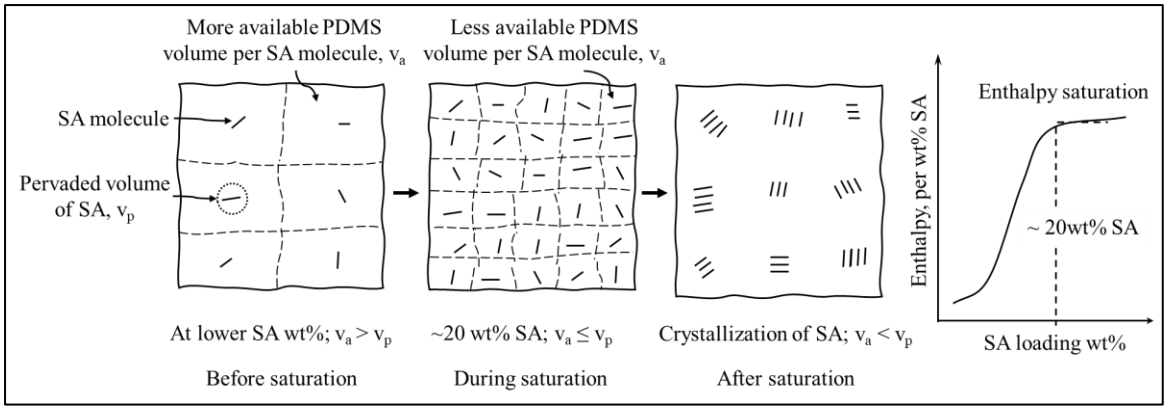

Figure 6.7: schematic representation showing PDMS free volume, SA molecular occupancy, and the transition to the constrained regime around 20 wt%

6.5.5 Transient cooling analysis

A pictorial representation of the experimental arrangement for analyzing the cooling characteristics of the samples is shown in Figure 6.8, as implemented with a related previous experimental setup[264]. A composite membrane was wrapped around a glass vial (external diameter: 24 mm), which was filled with hot silicone oil at a temperature ensuring complete melting of the SA within the membrane. For comparison, a predetermined amount of pure SA sealed in a polypropylene pouch was wrapped around the same vial setup.

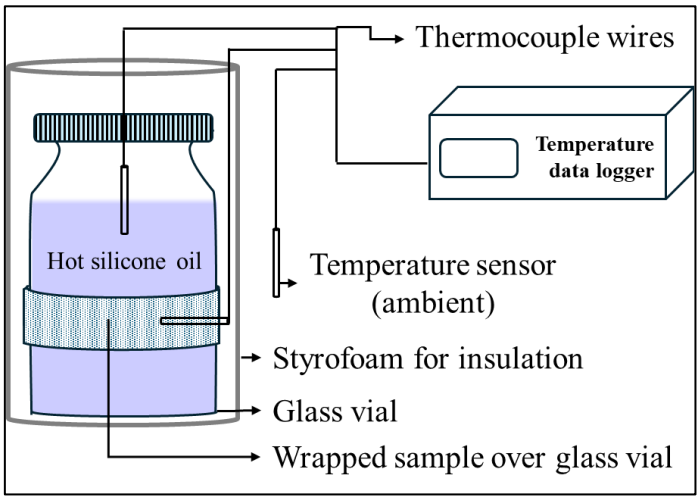

Figure 6.8: A pictorial arrangement for measuring time vs temperature variation between pure stearic acid and PDMS-SA composite membrane with insulation.

Thermal analyses of both configurations were conducted under insulated and non-insulated conditions, and the resulting temperature–time profiles were recorded during the cooling

cycle to evaluate and compare the thermal storage and heat release behavior (Figure 6.9). When comparing the thermal response of M_T4_SA23.3 with pure SA, a distinct difference in cooling behavior is observed. The membrane exhibits a noticeably slower cooling rate than pure SA, as evident from the broader temperature drop curve. This indicates the influence of PDMS, which acts as a thermal insulator, reducing the rate of heat dissipation and allowing the membrane to retain thermal energy for a longer duration. While pure SA shows a sharper decline in temperature, the composite matrix effectively delays heat transfer, a desirable characteristic in thermal energy storage applications where controlled heat release is crucial.

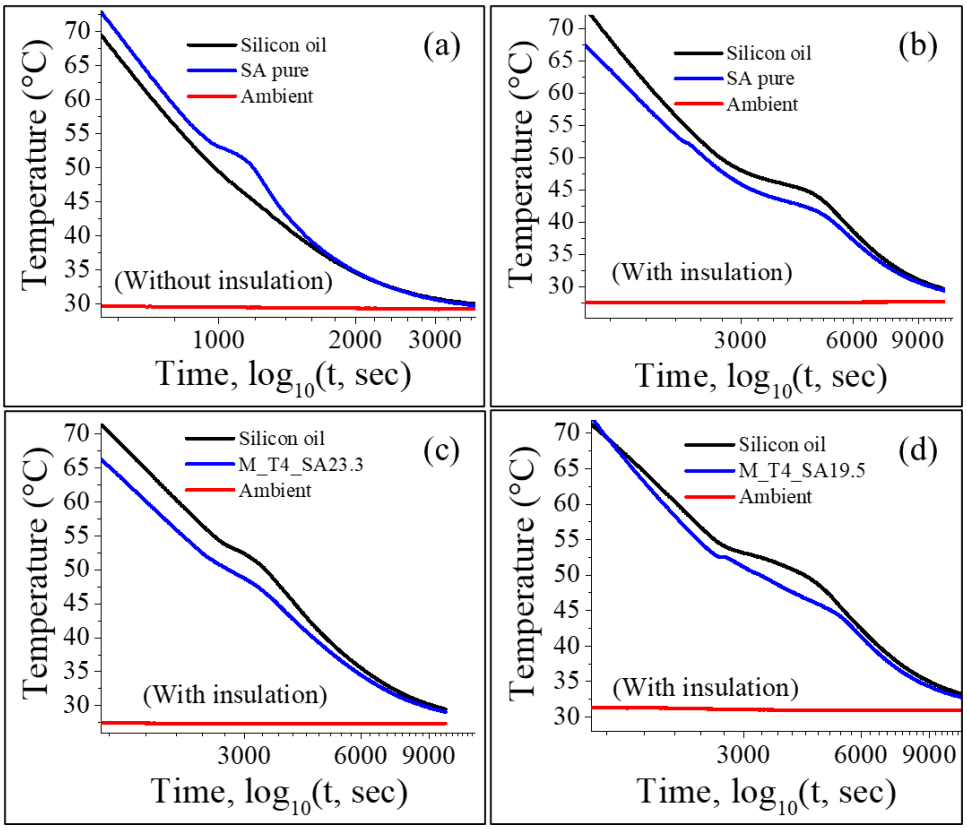

Figure 6.9: Temperature–time profiles comparing the cooling behavior of pure SA reference (a) without insulation, (b) with insulation and the SA-loaded composite PDMS membranes (c) 23.3wt% and (d) 19.5wt% under insulated condition.

Furthermore, the phase change duration, identified by the plateau region in the temperature-time curves, is broader for pure SA than for the composite membrane. This difference reflects the reduced quantity of active phase change material in the composite, which results in a shorter latent heat storage window. Additionally, the PDMS matrix may physically constrain the crystallization of stearic acid to some extent, further contributing to the narrower phase change range. Despite this, the thermal inertia introduced by PDMS

compensates by extending the overall cooling duration. The membrane containing 23.3 wt% SA showed noticeably slower cooling and maintained elevated temperatures for a longer duration compared to the membrane with 19.5 wt% SA.

The cooling rate was calculated from the slope of the temperature–time curve between ~70 °C and ambient temperature using, Cooling rate $= \frac{dT}{dt} \approx \frac{T_2 - T_1}{t_2 - t_1}$. The thermal time constant (τ) was determined using the 63% temperature drop criterion, i.e., the time required for the temperature to reach $T = T_\infty + 0.37(T_0 - T_\infty)$, based on initial ($T_0$), ambient ($T_\infty$), and corresponding time values from the transient cooling curve. The cooling rate decreased significantly from ~2.0 °C/min for uninsulated pure stearic acid to ~0.6 °C/min under insulated conditions, and further to ~0.29 °C/min for the PDMS–SA composite (23.3 wt%). This represents an overall reduction of nearly sevenfold, demonstrating the combined effect of external insulation and intrinsic thermal resistance of the polymer matrix in suppressing heat loss and enhancing thermal retention.

The thermal time constant (τ), estimated from the cooling profiles, increases significantly from ~1000 s for uninsulated pure stearic acid to ~6300 s for the PDMS–SA composite (23.3 wt%) under insulated conditions, indicating a substantial enhancement in thermal inertia. This increase reflects a progressive reduction in effective heat transfer rates due to both external insulation and the intrinsic low thermal conductivity of the PDMS matrix.

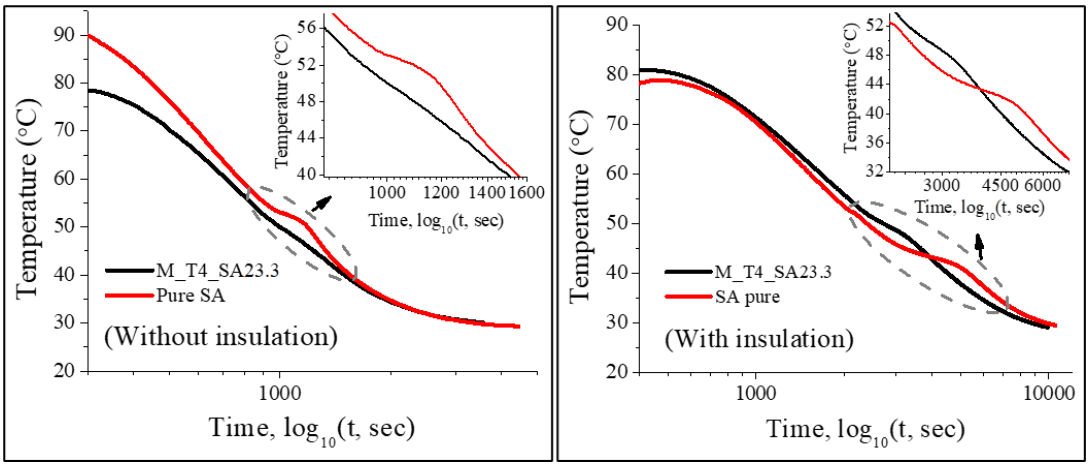

Figure 6.10: Temperature versus time analysis with and without insulation for pure stearic acid and membrane with 23.3wt% SA.

In Figure 6.10, comparisons between insulated and non-insulated conditions for both pure SA and the membrane reveal that insulation significantly slows down the cooling rate. This effect is more prominent in the membrane samples, where the internal insulation provided by PDMS is further enhanced by the external barrier. Such dual insulation mechanisms

demonstrate the potential of the membrane for applications requiring thermal regulation and storage, especially where insulation and material properties synergistically influence performance. Lastly, when insulation is removed, as shown in the non-insulated comparisons, both pure SA and the composite exhibit steeper cooling curves. However, the composite still cools more gradually than pure SA, reinforcing the inherent thermal buffering provided by the PDMS network. This behavior underlines the membrane's capacity to moderate thermal fluctuations even in uninsulated environments.

6.6 Challenges encountered and resolutions implemented

The preparation and thermal evaluation of stearic acid embedded PDMS membranes presented specific challenges related to membrane formation, PCM incorporation, and thermal performance. The major challenges and the corresponding resolution attempts are summarized below.

- **Challenge:** Ensuring uniform SA dispersion in PDMS at higher loading to avoid SA agglomeration and uneven thermal domains.
  Resolution: Controlled heating, optimized mixing, and doctor-blading enabled uniform SA distribution up to ~23 wt%.
- **Challenge:** Preventing PCM leakage during melting.
  Resolution: The cross-linked PDMS matrix physically entrapped SA while maintaining structural integrity.
- **Challenge:** Balancing latent heat storage with membrane flexibility.
  Resolution: A suitable SA loading range (5–23 wt%) was identified to retain flexibility and TES performance.
- **Challenge:** Reduced crystallization efficiency at high SA loading due to confinement within the polymer matrix.
  Resolution: An intermediate SA loading (~19.5 wt%) was identified to maximize latent heat utilization efficiency.
- **Challenge:** Rapid cooling and poor thermal retention of pure stearic acid.
  Resolution: Incorporation of the insulating PDMS matrix significantly reduced cooling rate and enhanced thermal inertia.
- **Challenge:** Solvent effects during membrane fabrication.
  Resolution: Experimental results confirmed negligible influence of THF volume

on membrane performance.

- **Challenge:** Evaluating thermal response under realistic heat-loss conditions.
  Resolution: Cooling analysis was conducted under both insulated and non-insulated conditions.

The issues that remain unresolved after the implemented resolution attempts have been briefly indicated in the Summary section and further included in Chapter 7 as part of the future research scope.

6.7 Literature comparison with the present work

The thermal energy storage performance of the present SA–PDMS membranes is compared with relevant polymer-supported PCM systems in Table 6.3.

Table 6.3: Literature comparison of matrix–PCM composite systems for thermal energy storage.

Matrix / PCM system	Key outcome	Relevance	Ref
PCM heat-transfer review	Materials, heat-transfer, applications reviewed	TES performance framework	[265]
PCM systems review	Leakage and low thermal conductivity identified	General TES design benchmark	[266]
PDMS / paraffin composites	Flexible PCM composite; 30 wt% paraffin feasible	PDMS-based flexible PCM benchmark	[267]
Expanded graphite / paraffin	Form-stable PCM; improved thermal conductivity and latent heat storage	Conductive-filler PCM benchmark	[268]
Expanded graphite / paraffin / silicone rubber	Shape-stable; improved thermal conductivity	Silicone-rubber PCM benchmark	[269]
SA / SiO_2 shell	SA microencapsulation improved thermal stability; enthalpy remained stable after 30 cycles.	SA benchmark for encapsulation stability and cycling.	[270]
Stearic acid PCM	Radial-direction stability and ~50.3% average heat-storage efficiency.	Foundational SA-TES study.	[271]
SA / TiO_2 nanofluids	TiO_2 addition reduced melting/solidification times and improved thermal stability.	Filler-assisted thermal-response enhancement in SA-based PCMs.	[272]

SA-embedded PDMS membranes	Efficiency increased from ~24% to ~80% at ~19.5 wt% SA; cooling rate reduced to ~0.29 °C min^{-1}	Flexible PDMS-SA TES membrane	This work

6.8 Summary

This study explores the development of PDMS-based composite membranes incorporating stearic acid (SA) as a phase change material for thermal energy storage applications. The membranes were fabricated using a controlled doctor-blading approach, where both SA loading and solvent content were systematically varied to tailor the internal structure and thermal response of the composite system. Performance is governed primarily by SA concentration within the polymer matrix. Increasing SA loading leads to a progressive enhancement in latent heat storage capacity, reflecting improved energy storage potential. However, this increase is not linearly translated into usable performance. Instead, an optimal composition is observed, beyond which further addition of SA results in reduced efficiency due to restricted crystallization within the confined polymer network.Thermal characterization indicates that the PDMS matrix plays a dual role: while it limits complete crystallization of the phase change material at higher loadings, it also significantly improves thermal stability by slowing heat dissipation. This is evidenced by a substantial reduction in cooling rate and a marked increase in the thermal time constant compared to pure stearic acid. As a result, the composite system exhibits enhanced thermal inertia, enabling more controlled heat storage and release. The study exhibits a link between processing parameters, material structure, and thermal performance. It identifies an intermediate SA loading (~19.5 wt%) as optimal for balancing energy storage capacity and utilization efficiency. These findings highlight the importance of compositional tuning in polymer–PCM composites, while long-term cycling stability, leakage resistance, and heat-transfer enhancement remain important aspects for future investigation.

Chapter 7: Conclusions and Future Scope

This chapter presents the overall outcomes of the thesis based on the development and evaluation of PDMS-based composite structures for continuous photocatalysis, membrane-based separation, liquid–liquid extraction, and thermal energy storage. The content is organized chapter-wise to clearly present the subjective conclusions, objective conclusions, unresolved issues, and future work associated with each experimental study. The subjective conclusions summarize the qualitative understanding and significance of the developed systems, while the objective conclusions highlight the major quantitative findings and best observed results. The unresolved issues and future work are also presented chapter-wise to indicate the remaining limitations and possible directions for further research.

7.1 Chapter 3

7.1.1 Conclusions

Subjective / Qualitative conclusions

- A novel method was successfully developed for immobilizing plasma-treated $ZnTiO_3$ particles inside a PDMS-lined coiled flow inverter (CFI) reactor.
- The swelling–deswelling assisted impregnation technique enabled effective incorporation and partial exposure of $ZnTiO_3$ particles within the PDMS lining.
- Plasma treatment improved particle dispersibility and surface characteristics, facilitating better immobilization inside the CFI.
- Characterization confirmed successful PDMS lining formation and $ZnTiO_3$ distribution along the inner channel surface.
- The $ZnTiO_3$-impregnated CFI exhibited superior photocatalytic performance compared to the straight tube under visible-light illumination.
- The CFI configuration enhanced photocatalytic kinetics while enabling compact continuous-flow operation.
- Low dark adsorption confirmed that MB removal predominantly occurred through photocatalytic degradation.

Objective / Quantitative conclusions

- Plasma-treated $ZnTiO_3$ particles exhibited a reduced optical band gap of 2.77 eV, supporting visible-light photocatalytic activity.
- $ZnTiO_3$ particles were immobilized inside the PDMS-lined CFI with an estimated particle area fraction of 0.105.
- The estimated exposed $ZnTiO_3$ particle area inside the CFI was 10.34 cm^2.
- Photocatalytic experiments were conducted using 10 ppm MB solution at flow rates 0.72, 0.96, 1.2, 1.44, 1.68 and 1.92 mL/min under a 25 W white-LED source.
- Dark adsorption remained low at approximately 4.5%.
- Pseudo-first-order rate constants ($k \pm$ 95% CI half-width) were:
    - $3.69 \pm 2.00 \times 10^{-3}$ min^{-1} for dark CFI operation,
    - $10.60 \pm 3.28 \times 10^{-3}$ min^{-1} for the illuminated straight tube,
    - $24.66 \pm 6.28 \times 10^{-3}$ min^{-1} for the illuminated CFI.
- The illuminated CFI achieved more than 2-fold higher photocatalytic activity than the illuminated straight tube and over 5-fold enhancement relative to dark operation.

7.1.2 Unresolved issues and future scope

- Improvement in the uniformity and thickness control of the PDMS lining inside the tubular reactor is still required for better reproducibility and particle distribution.
- Optimization of important operational parameters, such as, catalyst loading, flow rate, light intensity, residence time, and solution pH is necessary to maximize photocatalytic performance.
- Long-term stability, reusability, and possible particle leaching from the $ZnTiO_3$-impregnated CFI need to be systematically evaluated.
- The present study was limited to methylene blue model dye solution under laboratory conditions; therefore, validation using real industrial wastewater is required.
- The influence of higher dye concentration, elevated TDS, and alkaline conditions on reactor performance remains to be investigated.

- Scale-up studies are needed to assess the practical applicability of the $ZnTiO_3$-impregnated CFI system for continuous wastewater treatment and compact reactor design applications.

7.2 Chapter 4

7.2.1 Conclusions

Subjective conclusions (Qualitative insights):

- A novel low-temperature route was developed for preparing porous SiOC particles from PDMS.
- One-sided SiOC infusion created localized inorganic domains and asymmetric membrane properties.
- SiOC incorporation increased surface hydrophilicity and altered pore-size distribution.
- The modification introduces hydrophilic functional groups and creates localized water-affinitive domains, altering the interfacial transport mechanism.
- Enhanced ethanol transport occurred through a mixed solid–liquid interfacial diffusion pathway.
- Surface-localized SiOC modification improved separation performance without modifying the full membrane bulk.

Objective conclusions (Quantitative results):

- High surface-area SiOC particles (192 $m^2\ g^{-1}$) were synthesized from PDMS at 550 °C.
- One-sided infusion produced an asymmetric PDMS membrane with ~100 μm SiOC penetration depth.
- Pervaporation of a 50:50 ethanol–water mixture was conducted at 298 K with permeate conditions of 21 kPa and 3 °C.
- The membrane exhibited an overall flux of ~331 mL $m^{-2}\ h^{-1}$ during a 12 h operation.
- The modified membrane demonstrated an increase of approximately 150% in ethanol–water selectivity compared to the native membrane.

- Enhanced ethanol permeability was observed for a 50:50 ethanol–water mixture, while maintaining relatively low overall flux.

7.2.2 Unresolved challenges and future scope

- Further optimization of particle loading, infusion depth, and membrane thickness is required.
- Long-term membrane stability and possible SiOC leaching need investigation.
- Exploration of membrane performance with varying feed compositions and operating temperatures.
- Effects of feed composition, temperature, and vacuum conditions on transport behaviour remain unresolved.
- Scale-up of the membrane fabrication technique for potential industrial applications.
- Extension of this approach to other separation systems involving organic–aqueous mixtures.
- Development of predictive transport models incorporating coupled diffusion and interfacial phenomena for better process design.

7.3 Chapter 5

7.3.1 Conclusions

Subjective conclusions (Qualitative insights):

- A soft, transparent PDMS-CFI has been successfully fabricated using a removable helical PVA filament, enabling the creation of a continuous coiled microchannel.
- The coiled geometry significantly enhances phase interaction, mixing, and interfacial contact between immiscible liquids.
- The device demonstrates effective continuous liquid–liquid extraction capability in a compact millifluidic configuration.
- Flow dynamics play a critical role in governing mass transfer performance, with phase flow rates influencing the extent of mixing and separation efficiency.

- The system highlights the potential of PDMS-based millifluidic reactors for process intensification and scalable separation applications.

Objective conclusions (Quantitative results):

- The system was evaluated for extraction of acetic acid from a 10% (v/v) acetic acid–toluene mixture using water as the extracting phase.
- Tripling the organic phase flow rate (from 1 to 3 mL/min) at constant aqueous flow resulted in approximately a twofold increase in extraction efficiency.
- Doubling the aqueous phase flow rate (from 0.5 to 1 mL/min) at constant organic flow led to nearly a threefold enhancement in extraction efficiency.
- The aqueous phase flow rate exhibited a more pronounced effect on mass transfer compared to the organic phase.
- The maximum overall volumetric mass transfer coefficient ($k_{ov}a$) achieved was 0.007145 s^{-1} under the highest aqueous flow condition.

7.3.2 Unresolved issues and future scope

- Extended operation with toluene-rich streams may influence mechanical stability and requires endurance testing.
- Detailed evaluation of internal flow structure (e.g., interfacial deformation, recirculation patterns) has not yet been quantitatively examined.
- The current study evaluated extraction at fixed temperatures; thermal effects on mass transfer remain uninvestigated.
- Changes in PDMS surface hydrophobicity during repeated solvent exposure may alter reactor performance
- Investigation of a wider range of flow rate ratios and phase properties to further optimize mass transfer performance.
- Exploration of different solvent systems and solutes to extend applicability of the CFI reactor.
- Study of scale-up strategies and parallelization of CFI units for industrial implementation.
- Integration of in-line monitoring techniques for real-time analysis of extraction

efficiency.

- Evaluation of long-term operational stability and material compatibility under continuous processing conditions.

7.4 Chapter 6

7.4.1 Conclusions

Subjective conclusions (Qualitative insights):

- Flexible PDMS-based composite membranes incorporating stearic acid (SA) were successfully developed for thermal energy storage applications.
- The doctor-blade fabrication technique enabled uniform PCM distribution while maintaining membrane integrity.
- FTIR confirmed physical incorporation of SA within the PDMS matrix with negligible residual solvent.
- Membrane morphology and SA loading strongly influenced thermal behavior, whereas THF variation had minimal effect.
- The composite membranes exhibited enhanced thermal inertia and controlled heat-release characteristics compared to pure SA.
- The study established a clear processing–structure–property relationship between SA loading, membrane structure, and TES performance.
- The PDMS matrix exhibited a dual role by restricting complete crystallization at high SA loading while simultaneously enhancing thermal retention.
- An intermediate SA loading provided the best balance between latent heat storage and utilization efficiency rather than the highest SA loading.
- The developed composites show strong potential for thermal management and controlled thermal-response applications.

Objective conclusions (Quantitative results):

- SA loading in the membranes was varied from 5.7 wt% to 23.3 wt%.
- DSC analysis showed melting temperatures near 56 °C and crystallization temperatures around 52–53 °C.

- Latent heat increased from ~ 2.7 to 34.3 J g^{-1} with increasing SA loading.
- Latent heat utilization efficiency increased from ~ 24% to nearly 80% at around 19.5 wt% SA, followed by a slight decline at higher loading.
- Cooling rate decreased from ~ 2.0 °C min^{-1} for pure SA to nearly 0.29 °C min^{-1} for the composite membranes.
- The thermal time constant increased from ~ 1000 s for pure SA to nearly 6300 s for the composite system.
- The composition containing ~ 19.5 wt% SA was identified as the optimum formulation for maximizing thermal storage efficiency.

7.4.2 Unresolved issues and future scope

- Enhancement of heat transfer rates through incorporation of thermally conductive fillers (e.g., graphite, BN, metal particles).
- Optimization of PCM loading beyond 23 wt% while preventing phase separation or mechanical.
- Long-term thermal cycling studies to evaluate durability, leakage resistance, and mechanical durability.
- Scale-up of the doctor-blade fabrication method for large-area membrane production.
- Optimization of membrane thickness for balancing heat-transfer rate and thermal storage capacity.
- Integration of these composites into practical systems, such as, smart textiles, portable thermal management, and electronic cooling modules.
- Investigation of alternative phase change materials with higher latent heat or different transition temperatures.

References

[1] M.K. Thakur, V.K. Thakur, eds., Handbook of polymers for pharmaceutical technologies: Volume 1: Structure and chemistry, Scrivener Publishing LLC, Salem, Massachusetts, 2015. https://doi.org/10.1002/9781119041375.

[2] R. Ariati, F. Sales, A. Souza, R.A. Lima, J. Ribeiro, Polydimethylsiloxane Composites Characterization and Its Applications: A Review, Polymers 13 (2021) 4258. https://doi.org/10.3390/polym13234258.

[3] J.E. Mark, Some Interesting Things about Polysiloxanes, Acc. Chem. Res. 37 (2004) 946–953. https://doi.org/10.1021/ar030279z.

[4] I. Blanco, Polysiloxanes in Theranostics and Drug Delivery: A Review, Polymers 10 (2018) 755. https://doi.org/10.3390/polym10070755.

[5] S. Li, J. Zhang, J. He, W. Liu, Y. Wang, Z. Huang, H. Pang, Y. Chen, Functional PDMS Elastomers: Bulk Composites, Surface Engineering, and Precision Fabrication, Advanced Science 10 (2023). https://doi.org/10.1002/advs.202304506.

[6] N. Tucher, Analysis of photonic structures for silicon solar cells, 2016.

[7] F.B. Madsen, A.E. Daugaard, C. Fleury, S. Hvilsted, A.L. Skov, Visualisation and characterisation of heterogeneous bimodal PDMS networks, RSC Adv. 4 (2014) 6939–6945. https://doi.org/10.1039/C3RA47522K.

[8] I.D. Johnston, D.K. McCluskey, C.K.L. Tan, M.C. Tracey, Mechanical characterization of bulk Sylgard 184 for microfluidics and microengineering, J. Micromech. Microeng. 24 (2014) 035017. https://doi.org/10.1088/0960-1317/24/3/035017.

[9] Z. Wang, A.A. Volinsky, N.D. Gallant, Crosslinking effect on polydimethylsiloxane elastic modulus measured by custom-built compression instrument, J of Applied Polymer Sci 131 (2014). https://doi.org/10.1002/app.41050.

[10] K. Karimi Nikoo, P.R. Dvornic, J.L. Self, T.E. Long, Siloxane-containing polymers: from synthesis and characterization to advanced applications and sustainability, Polymer International 74 (2025) 633–650. https://doi.org/10.1002/pi.6764.

[11] N.R. Thomas, Frederic Stanley Kipping—Pioneer in Silicon Chemistry: His Life & Legacy, Silicon 2 (2010) 187–193. https://doi.org/10.1007/s12633-010-9051-x.

[12] J. Guo, Y. Yu, L. Cai, Y. Wang, K. Shi, L. Shang, J. Pan, Y. Zhao, Microfluidics for flexible electronics, Materials Today 44 (2021) 105–135. https://doi.org/10.1016/j.mattod.2020.08.017.

[13] G.M. Whitesides, The origins and the future of microfluidics, Nature 442 (2006) 368–373. https://doi.org/10.1038/nature05058.

[14] J. Chen, J. Zheng, Q. Gao, J. Zhang, J. Zhang, O.M. Omisore, L. Wang, H. Li, Polydimethylsiloxane (PDMS)-Based Flexible Resistive Strain Sensors for Wearable Applications, Applied Sciences 8 (2018) 345. https://doi.org/10.3390/app8030345.

[15] Electronic Applications of Polydimethylsiloxane and Its Composites, in: Springer Series on Polymer and Composite Materials, Springer International Publishing, Cham, 2016: pp. 199–228. https://doi.org/10.1007/978-3-319-23663-6_7.

[16] I. Miranda, A. Souza, P. Sousa, J. Ribeiro, E. Castanheira, R. Lima, G. Minas, Properties and Applications of PDMS for Biomedical Engineering: A Review, Journal of Functional Biomaterials 13 (2021) 2. https://doi.org/10.3390/jfb13010002.

[17] J.N. Lee, C. Park, G.M. Whitesides, Solvent Compatibility of Poly(dimethylsiloxane)-Based Microfluidic Devices, Anal. Chem. 75 (2003) 6544–6554. https://doi.org/10.1021/ac0346712.

[18] N. Rungruangkitkrai, P. Phromphen, N. Chartvivatpornchai, A. Srisa, Y. Laorenza, P. Wongphan, N. Harnkarnsujarit, Water Repellent Coating in Textile, Paper and Bioplastic Polymers: A Comprehensive Review, Polymers 16 (2024) 2790. https://doi.org/10.3390/polym16192790.

[19] L. Hauer, A. Naga, R.G.M. Badr, J.T. Pham, W.S.Y. Wong, D. Vollmer, Wetting on silicone surfaces, Soft Matter 20 (2024) 5273–5295. https://doi.org/10.1039/D4SM00346B.

[20] W.S.Y. Wong, L. Hauer, A. Naga, A. Kaltbeitzel, P. Baumli, R. Berger, M. D'Acunzi, D. Vollmer, H.-J. Butt, Adaptive Wetting of Polydimethylsiloxane, Langmuir 36 (2020) 7236–7245. https://doi.org/10.1021/acs.langmuir.0c00538.

[21] H.T. Kim, O.C. Jeong, PDMS surface modification using atmospheric pressure plasma, Microelectronic Engineering 88 (2011) 2281–2285. https://doi.org/10.1016/j.mee.2011.02.084.

[22] T.C. Merkel, V.I. Bondar, K. Nagai, B.D. Freeman, I. Pinnau, Gas sorption, diffusion, and permeation in poly(dimethylsiloxane), Journal of Polymer Science Part B: Polymer Physics 38 (2000) 415–434. https://doi.org/10.1002/(SICI)1099-0488(20000201)38:3%3C415::AID-POLB8%3E3.0.CO;2-Z.

[23] A.C. Kuo, Poly (dimethylsiloxane), Polymer Data Handbook 1999 (1999) 411–435.

[24] M. Liu, J. Sun, Q. Chen, Influences of heating temperature on mechanical properties of polydimethylsiloxane, Sensors and Actuators A: Physical 151 (2009) 42–45. https://doi.org/10.1016/j.sna.2009.02.016.

[25] G. Ducom, B. Laubie, A. Ohannessian, C. Chottier, P. Germain, V. Chatain, Hydrolysis of polydimethylsiloxane fluids in controlled aqueous solutions, Water Sci Technol 68 (2013) 813–820. https://doi.org/10.2166/wst.2013.308.

[26] M.W. Toepke, D.J. Beebe, PDMS absorption of small molecules and consequences in microfluidic applications, Lab Chip 6 (2006) 1484–1486. https://doi.org/10.1039/B612140C.

[27] A.H. Mostafavi, A.K. Mishra, F. Gallucci, J.H. Kim, M. Ulbricht, A.M. Coclite, S.S. Hosseini, Advances in surface modification and functionalization for tailoring the characteristics of thin films and membranes via chemical vapor deposition techniques, Journal of Applied Polymer Science 140 (2023) e53720. https://doi.org/10.1002/app.53720.

[28] P. Colombo, G. Mera, R. Riedel, G.D. Sorarù, Polymer-Derived Ceramics: 40 Years of Research and Innovation in Advanced Ceramics, in: Ceramics Science and Technology, John Wiley & Sons, Ltd, 2013: pp. 245–320. https://doi.org/10.1002/9783527631940.ch57.

[29] E. Ionescu, Polymer-Derived Ceramics, in: Ceramics Science and Technology, John Wiley & Sons, Ltd, 2013: pp. 457–500. https://doi.org/10.1002/9783527631940.ch49.

[30] J. Ding, W. Li, J. Ding, W. Li, Polymer-Derived Advanced Engineering Ceramics, in: Advanced Ceramic Materials - Emerging Technologies, IntechOpen, 2024. https://doi.org/10.5772/intechopen.1007167.

[31] P.A. Loughney, S.B. Mujib, T.L. Pruyn, G. Singh, K. Lu, V. Doan-Nguyen, Enhancing organosilicon polymer-derived ceramic properties, Journal of Applied Physics 132 (2022) 070901. https://doi.org/10.1063/5.0085844.

[32] B. Viswanathan, V. Suryakumar, B. Venugopal, S.H. Roshna, N. Hariprasad, Perovskite materials an introduction, Chennai, Jun (2019). http://catalysis.eprints.iitm.ac.in/3485/1/Perovskite%20Materials%20An%20Introduction.pdf (accessed August 2, 2025).

[33] L. Ortega-San-Martin, Introduction to Perovskites: A Historical Perspective, in: N.S. Arul, V.D. Nithya (Eds.), Revolution of Perovskite, Springer Singapore, Singapore, 2020: pp. 1–41. https://doi.org/10.1007/978-981-15-1267-4_1.

[34] S.J.J. Kay, A. Thirumurugan, S. Gobalakrishnan, N. Chidhambaram, Evolving landscape of perovskite nanomaterials: a comprehensive review of past, present, and future trends, Coordination Chemistry Reviews 545 (2025) 217020. https://doi.org/10.1016/j.ccr.2025.217020.

[35] W.-Y. Chen, C.-P. Wang, P.-C. Chen, K.-Y.A. Lin, S. Ghosh, C.-W. Huang, V.-H. Nguyen, Perovskite Zinc Titanate Photocatalysts Synthesized by the Sol–Gel Method and Their Application in the Photocatalytic Degradation of Emerging Contaminants, Catalysts 11 (2021) 854. https://doi.org/10.3390/catal11070854.

[36] M. Tang, S. Lu, L. He, X. Zhu, W. Feng, W. Zhang, Preparation, Characterization of ZnTiO3/ZnO Composite Materials and Their Photocatalytic Performance, Nanomaterials (Basel) 12 (2022) 1345. https://doi.org/10.3390/nano12081345.

[37] M. Helal Miah, M. Uddin Khandaker, M. Bulu Rahman, M. Nur-E-Alam, M. Aminul Islam, Band gap tuning of perovskite solar cells for enhancing the efficiency and stability: issues and prospects, RSC Advances 14 (2024) 15876–15906. https://doi.org/10.1039/D4RA01640H.

[38] P. Thakur, N. Sharma, D. Pathak, P. Sharma, K. Kishore, S. Dhar, M. Lal, State-of-art review on smart perovskites materials: properties and applications, Emergent Mater. 7 (2024) 667–694. https://doi.org/10.1007/s42247-024-00645-w.

[39] M. Noman, Z. Khan, S. Tariq Jan, A comprehensive review on the advancements and challenges in perovskite solar cell technology, RSC Advances 14 (2024) 5085–5131. https://doi.org/10.1039/D3RA07518D.

[40] Y. Choi, S. Han, B.-I. Park, Z. Xu, Q. Huang, S. Bae, J.S. Kim, S.O. Kim, Y. Meng, S. Kim, J. Moon, I. Roh, J.-W. Park, S. Bae, Perovskite nanocomposites: synthesis, properties, and applications from renewable energy to optoelectronics, Nano Convergence 11 (2024) 36. https://doi.org/10.1186/s40580-024-00440-7.

[41] J.A. McLeod, A. Moewes, D.A. Zatsepin, E.Z. Kurmaev, A. Wypych, I. Bobowska, A. Opasinska, S.O. Cholakh, Predicting the band gap of ternary oxides containing 3${d}^{10}$ and 3${d}^{0}$ metals, Phys. Rev. B 86 (2012) 195207. https://doi.org/10.1103/PhysRevB.86.195207.

[42] L. BUDIGI, M.R. NASINA, K. SHAIK, S. AMARAVADI, Structural and optical properties of zinc titanates synthesized by precipitation method, J Chem Sci 127 (2015) 509–518. https://doi.org/10.1007/s12039-015-0802-5.

[43] K. Kalantari, E. Asgari, Photocatalytic degradation of Direct Red 80 using ZnO/ZnTiO3/Zn2Ti3O8 ternary nanocomposite, Desalination and Water Treatment 284 (2023) 240–250. https://doi.org/10.5004/dwt.2023.29234.

[44] S. Lei, H. Fan, X. Ren, J. Fang, L. Ma, Z. Liu, Novel sintering and band gap engineering of ZnTiO3 ceramics with excellent microwave dielectric properties, J. Mater. Chem. C 5 (2017) 4040–4047. https://doi.org/10.1039/C7TC00815E.

[45] S. Paul, S. Barman, A. Datta, Zn-based oxide perovskite nanocomposites for energy and sensing applications, J Mater Sci 59 (2024) 17968–17990. https://doi.org/10.1007/s10853-024-09765-4.

[46] M. Mohamed, Y.B. Saddeek, A. Sedky, A.S. Alshammari, Z.R. Khan, K. Aly, M. Bouzidi, A.B. Saddek, ZnTiO3-nanoparticles effect on the structure, FTIR, and optical properties of SiO2 – B2O3 – Al2O3 glasses, Ceramics International 50 (2024) 46484–46495. https://doi.org/10.1016/j.ceramint.2024.08.493.

[47] Md.M. Islam, A.R. Aidid, J.N. Mohshin, H. Mondal, S. Ganguli, A.K. Chakraborty, A critical review on textile dye-containing wastewater: Ecotoxicity, health risks, and remediation strategies for environmental safety, Cleaner Chemical Engineering 11 (2025) 100165. https://doi.org/10.1016/j.clce.2025.100165.

[48] T.E. Oladimeji, M. Oyedemi, M.E. Emetere, O. Agboola, J.B. Adeoye, O.A. Odunlami, Review on the impact of heavy metals from industrial wastewater effluent and removal technologies, Heliyon 10 (2024) e40370. https://doi.org/10.1016/j.heliyon.2024.e40370.

[49] P.O. Oladoye, T.O. Ajiboye, E.O. Omotola, O.J. Oyewola, Methylene blue dye: Toxicity and potential elimination technology from wastewater, Results in Engineering 16 (2022) 100678. https://doi.org/10.1016/j.rineng.2022.100678.

[50] S.C. Pillai, N.B. McGuinness, C. Byrne, C. Han, J. Lalley, M. Nadagouda, P. Falaras, A.G. Kontos, M.A. Gracia-Pinilla, K. O'Shea, Photocatalysis as an effective advanced oxidation process, Advanced Oxidation Processes for Water Treatment: Fundamentals and Applications (2017) 333–381.

[51] S. Khan, T. Noor, N. Iqbal, L. Yaqoob, Photocatalytic Dye Degradation from Textile Wastewater: A Review, ACS Omega 9 (2024) 21751–21767. https://doi.org/10.1021/acsomega.4c00887.

[52] P. Liang, W. Yang, H. Peng, S. Zhao, Efficient Degradation of Methylene Blue in Industrial Wastewater and High Cycling Stability of Nano ZnO, Molecules 29 (2024) 5584. https://doi.org/10.3390/molecules29235584.

[53] L. Amiri, H. Ermagan, J.C. Kurnia, F. Hassani, A.P. Sasmito, Progress on rock thermal energy storage (RTES): A state of the art review, Energy Science & Engineering 12 (2024) 410–437. https://doi.org/10.1002/ese3.1478.

[54] V. Badescu, ed., Power engineering: advances and challenges: part A: thermal, hydro and nuclear power, CRC Press, Boca Raton, FL London New York, 2018.

[55] A.J. Carrillo, J. González-Aguilar, M. Romero, J.M. Coronado, Solar Energy on Demand: A Review on High Temperature Thermochemical Heat Storage Systems and Materials, Chem. Rev. 119 (2019) 4777–4816. https://doi.org/10.1021/acs.chemrev.8b00315.

[56] Y. Zhao, C.Y. Zhao, C.N. Markides, H. Wang, W. Li, Medium- and high-temperature latent and thermochemical heat storage using metals and metallic compounds as heat storage media: A technical review, Applied Energy 280 (2020) 115950. https://doi.org/10.1016/j.apenergy.2020.115950.

[57] I. Sarbu, C. Sebarchievici, A Comprehensive Review of Thermal Energy Storage, Sustainability 10 (2018) 191. https://doi.org/10.3390/su10010191.

[58] I. Sarbu, A. Dorca, Review on heat transfer analysis in thermal energy storage using latent heat storage systems and phase change materials, International Journal of Energy Research 43 (2019) 29–64. https://doi.org/10.1002/er.4196.

[59] G. Peng, G. Dou, Y. Hu, Y. Sun, Z. Chen, Phase Change Material (PCM) Microcapsules for Thermal Energy Storage, Advances in Polymer Technology 2020 (2020) 9490873. https://doi.org/10.1155/2020/9490873.

[60] M. Kenisarin, K. Mahkamov, Solar energy storage using phase change materials, Renewable and Sustainable Energy Reviews 11 (2007) 1913–1965. https://doi.org/10.1016/j.rser.2006.05.005.

[61] A.S. Fleischer, Thermal energy storage using phase change materials: Fundamentals and applications, in: SpringerBriefs in Applied Sciences and Technology, Springer Verlag, 2015. https://doi.org/10.1007/978-3-319-20922-7.

[62] B. Kanimozhi, K. Harish, B.S. Tarun, P.S. Sainath Reddy, P.S. Sujeeth, Charging and Discharging Processes of Thermal Energy Storage System Using Phase change materials, IOP Conf. Ser.: Mater. Sci. Eng. 197 (2017) 012040. https://doi.org/10.1088/1757-899X/197/1/012040.

[63] D.S. Sholl, R.P. Lively, Seven chemical separations to change the world, Nature 532 (2016) 435–437. https://doi.org/10.1038/532435a.

[64] R. Vooradi, S.B. Anne, A.K. Tula, M.R. Eden, R. Gani, Energy and CO2 management for chemical and related industries: issues, opportunities and challenges, BMC Chemical Engineering 1 (2019) 7. https://doi.org/10.1186/s42480-019-0008-6.

[65] N.R. Council, D. on Engineering, P. Sciences, N.M.A. Board, C. on Engineering, T. Systems, C. on I.T. Assessments, P. on S.T. for I. Reuse, Recycling, Separation Technologies for the Industries of the Future, National Academies Press, 1999. https://books.google.com/books?hl=en&lr=&id=U2KdAgAAQBAJ&oi=fnd&pg=PR12&dq=Separation+Technologies+for+the+Industries+of+the+Future&ots=ydcTUC2Smf&sig=Q3TY9FWKhru4fBNprildDU_LOp4 (accessed August 8, 2025).

[66] Y.A. Bhadange, J. Carpenter, V.K. Saharan, A Comprehensive Review on Advanced Extraction Techniques for Retrieving Bioactive Components from Natural Sources, ACS Omega 9 (2024) 31274–31297. https://doi.org/10.1021/acsomega.4c02718.

[67] B.K. Dutta, Principles of mass transfer and seperation processes, PHI Learning Pvt. Ltd., 2007. https://books.google.com/books?hl=en&lr=&id=a6uMtgoxjyIC&oi=fnd&pg=PP1&dq=principles+of+mass+transfer+and+separation+processes&ots=rbhY1ydK09&sig=UrmUHKm95PJ5ipQlEPZBJKVVD8o (accessed August 8, 2025).

[68] M. Skiborowski, A. Górak, Hybrid separation processes, Process Intensification by Reactive and Membrane-Assisted Separations (2022). https://books.google.com/books?hl=en&lr=&id=AEV3EAAAQBAJ&oi=fnd&pg=PA49&dq=%22hybrid+separation+processes%22,+combine+liquid-

liquid+extraction+with+membrane+separation+(e.g.,+pervaporation)+&ots=G-KNJIKpvT&sig=vMJQ5SHRGO2FZKABGRGPrLl4LBE (accessed August 8, 2025).

[69] W. Marquardt, S. Kossack, K. Kraemer, A Framework for the Systematic Design of Hybrid Separation Processes*, Chinese Journal of Chemical Engineering 16 (2008) 333–342. https://doi.org/10.1016/S1004-9541(08)60084-1.

[70] A.I. Osman, Z. Chen, A.M. Elgarahy, M. Farghali, I.M.A. Mohamed, A. k. Priya, H.B. Hawash, P.-S. Yap, Membrane Technology for Energy Saving: Principles, Techniques, Applications, Challenges, and Prospects, Advanced Energy and Sustainability Research 5 (2024) 2400011. https://doi.org/10.1002/aesr.202400011.

[71] X. Cao, K. Wang, X. Feng, Mass transfer fundamentals in pervaporation, perstraction and sorption: A unified approach, Chemical Engineering Research and Design 204 (2024) 282–291. https://doi.org/10.1016/j.cherd.2024.02.045.

[72] W. Li, J. Estager, J.-C.M. Monbaliu, D.P. Debecker, P. Luis, Separation of bio-based chemicals using pervaporation, Journal of Chemical Technology & Biotechnology 95 (2020) 2311–2334. https://doi.org/10.1002/jctb.6434.

[73] T. Mahdi, A. Ahmad, M.M. Nasef, A. Ripin, State-of-the-Art Technologies for Separation of Azeotropic Mixtures, Separation & Purification Reviews 44 (2015) 308–330. https://doi.org/10.1080/15422119.2014.963607.

[74] J. Zhang, B. Hu, Liquid-Liquid Extraction (LLE), in: Separation and Purification Technologies in Biorefineries, John Wiley & Sons, Ltd, 2013: pp. 61–78. https://doi.org/10.1002/9781118493441.ch3.

[75] F.M. Antony, D. Pal, K. Wasewar, Separation of bio-products by liquid–liquid extraction, Physical Sciences Reviews 6 (2021) 20180065. https://doi.org/10.1515/psr-2018-0065.

[76] S. Tripathy, Top-down and Bottom-up Approaches for Synthesis of Nanoparticles, in: J.N. Cruz (Ed.), Materials Research Foundations, 1st ed., Materials Research Forum LLC, 2023: pp. 92–130. https://doi.org/10.21741/9781644902370-4.

[77] A.M. El-Khawaga, A. Zidan, A.I.A.A. El-Mageed, Preparation methods of different nanomaterials for various potential applications: A review, Journal of Molecular Structure 1281 (2023) 135148. https://doi.org/10.1016/j.molstruc.2023.135148.

[78] K.A. Altammar, A review on nanoparticles: characteristics, synthesis, applications, and challenges, Front. Microbiol. 14 (2023). https://doi.org/10.3389/fmicb.2023.1155622.

[79] C.J. Brinker, G.W. Scherer, Sol-gel science: the physics and chemistry of sol-gel processing, Gulf Professional Publishing, 1990. https://books.google.com/books?hl=en&lr=&id=V2vRvsTaCwMC&oi=fnd&pg=PR11&dq=The+Physics+and+Chemistry+of+Sol-Gel+Processing&ots=WQFVjW5jDO&sig=I4bUrs5SxMl7nEx8-9OC1pRSDIk (accessed August 10, 2025).

[80] S. Esposito, “Traditional” Sol-Gel Chemistry as a Powerful Tool for the Preparation of Supported Metal and Metal Oxide Catalysts, Materials 12 (2019) 668. https://doi.org/10.3390/ma12040668.

[81] G.J. Owens, R.K. Singh, F. Foroutan, M. Alqaysi, C.-M. Han, C. Mahapatra, H.-W. Kim, J.C. Knowles, Sol–gel based materials for biomedical applications, Progress in Materials Science 77 (2016) 1–79. https://doi.org/10.1016/j.pmatsci.2015.12.001.

[82] V. Kumar, M. Mridha, A.K. Gupta, K.D.P. Nigam, Coiled flow inverter as a heat exchanger, Chemical Engineering Science 62 (2007) 2386–2396. https://doi.org/10.1016/j.ces.2007.01.032.

[83] D. Rossi, L. Gargiulo, G. Valitov, A. Gavriilidis, L. Mazzei, Experimental characterization of axial dispersion in coiled flow inverters, Chemical Engineering Research and Design 120 (2017) 159–170. https://doi.org/10.1016/j.cherd.2017.02.011.

[84] A.S.M. Raja, A. Arputharaj, S. Saxena, P.G. Patil, 9 - Water requirement and sustainability of textile processing industries, in: S.S. Muthu (Ed.), Water in Textiles and Fashion, Woodhead Publishing, 2019: pp. 155–173. https://doi.org/10.1016/B978-0-08-102633-5.00009-9.

[85] R. Kishor, D. Purchase, G.D. Saratale, R.G. Saratale, L.F.R. Ferreira, M. Bilal, R. Chandra, R.N. Bharagava, Ecotoxicological and health concerns of persistent coloring pollutants of textile industry wastewater and treatment approaches for environmental safety, Journal of Environmental Chemical Engineering 9 (2021) 105012. https://doi.org/10.1016/j.jece.2020.105012.

[86] Z. Li, P.-H. Chang, W.-T. Jiang, J.-S. Jean, H. Hong, Mechanism of methylene blue removal from water by swelling clays, Chemical Engineering Journal 168 (2011) 1193–1200. https://doi.org/10.1016/j.cej.2011.02.009.

[87] N. Hemashenpagam, S. Selvajeyanthi, Textile Dyes and Their Effect on Human Beings | SpringerLink, (2024). https://link.springer.com/chapter/10.1007/978-981-99-3901-5_3 (accessed May 6, 2024).

[88] J. Sharma, S. Sharma, V. Soni, Classification and impact of synthetic textile dyes on Aquatic Flora: A review, Regional Studies in Marine Science 45 (2021) 101802. https://doi.org/10.1016/j.rsma.2021.101802.

[89] A.M. Awad, R. Jalab, A. Benamor, M.S. Nasser, M.M. Ba-Abbad, M. El-Naas, A.W. Mohammad, Adsorption of organic pollutants by nanomaterial-based adsorbents: An overview, Journal of Molecular Liquids 301 (2020) 112335. https://doi.org/10.1016/j.molliq.2019.112335.

[90] A. Pariatamby, Y.L. Kee, Persistent Organic Pollutants Management and Remediation, Procedia Environmental Sciences 31 (2016) 842–848. https://doi.org/10.1016/j.proenv.2016.02.093.

[91] P. Kumari, N. Bahadur, L.F. Dumée, Photo-catalytic membrane reactors for the remediation of persistent organic pollutants – A review, Separation and Purification Technology 230 (2020) 115878. https://doi.org/10.1016/j.seppur.2019.115878.

[92] B. Song, G. Zeng, J. Gong, J. Liang, P. Xu, Z. Liu, Y. Zhang, C. Zhang, M. Cheng, Y. Liu, S. Ye, H. Yi, X. Ren, Evaluation methods for assessing effectiveness of in situ remediation of soil and sediment contaminated with organic pollutants and heavy metals, Environment International 105 (2017) 43–55. https://doi.org/10.1016/j.envint.2017.05.001.

[93] D. S., R.J. Tayade, Low temperature energy- efficient synthesis methods for bismuth-based nanostructured photocatalysts for environmental remediation application: A

review, Chemosphere 304 (2022) 135300. https://doi.org/10.1016/j.chemosphere.2022.135300.

[94] C.P. Tiwari, F. Delgado-Licona, M. Valencia-Llompart, S. Nuñez-Correa, K.D.P. Nigam, A. Montesinos-Castellanos, E.A. López-Guajardo, A. Aguirre-Soto, Shining Light on the Coiled-Flow Inverter—Continuous-Flow Photochemistry in a Static Mixer, Ind. Eng. Chem. Res. 59 (2020) 3865–3872. https://doi.org/10.1021/acs.iecr.9b05008.

[95] S. Soni, L. Sharma, P. Meena, S. Roy, K.D.P. Nigam, Compact coiled flow inverter for process intensification, Chemical Engineering Science 193 (2019) 312–324. https://doi.org/10.1016/j.ces.2018.09.008.

[96] S. Vashisth, K.D.P. Nigam, Experimental Investigation of Pressure Drop during Two-Phase Flow in a Coiled Flow Inverter, Ind. Eng. Chem. Res. 46 (2007) 5043–5050. https://doi.org/10.1021/ie061490s.

[97] S. Vashisth, K.D.P. Nigam, Liquid-Phase Residence Time Distribution for Two-Phase Flow in Coiled Flow Inverter, Industrial & Engineering Chemistry Research - IND ENG CHEM RES 47 (2008) 3630–3638. https://doi.org/10.1021/ie070447h.

[98] M.M. Mandal, P. Aggarwal, K.D.P. Nigam, Liquid–Liquid Mixing in Coiled Flow Inverter, Ind. Eng. Chem. Res. 50 (2011) 13230–13235. https://doi.org/10.1021/ie2002473.

[99] S.N. Chanquia, A. Valotta, H. Gruber-Woelfler, S. Kara, Photobiocatalysis in Continuous Flow, Front. Catal. 1 (2022). https://doi.org/10.3389/fctls.2021.816538.

[100] S.S. Tomar, N. Verma, K.D.P. Nigam, Process Intensification for Enhanced Photocatalytic Degradation of Aqueous Paracetamol Using a Coiled Flow Inverter, Ind. Eng. Chem. Res. 64 (2025) 2036–2048. https://doi.org/10.1021/acs.iecr.4c03547.

[101] G.K. Agrahari, M.S. Vignesh, K.D.P. Nigam, Novel devices for the extraction and recovery of rare-earth metals through recycling of waste, J Mater Cycles Waste Manag 26 (2024) 109–137. https://doi.org/10.1007/s10163-023-01862-x.

[102] H. Zhu, K.-J. Wu, C.-H. He, Ultrasound-assisted synthesis of visible-light-driven Ag/g-C3N4 catalysts in a continuous flow reactor, Chemical Engineering Journal 429 (2022) 132412. https://doi.org/10.1016/j.cej.2021.132412.

[103] S.S. Tomar, N. Verma, K.D.P. Nigam, Biogenic Synthesis of the Mixed-Valence Fexoy/G-Cn Electrocatalyst Using Coiled Flow Inverter for Green Hydrogen Evolution, (2025). https://doi.org/10.2139/ssrn.5277403.

[104] D. Cambié, C. Bottecchia, N.J.W. Straathof, V. Hessel, T. Noël, Applications of Continuous-Flow Photochemistry in Organic Synthesis, Material Science, and Water Treatment, Chem. Rev. 116 (2016) 10276–10341. https://doi.org/10.1021/acs.chemrev.5b00707.

[105] S. Perween, A. Ranjan, Improved visible-light photocatalytic activity in ZnTiO3 nanopowder prepared by sol-electrospinning, Solar Energy Materials and Solar Cells 163 (2017) 148–156. https://doi.org/10.1016/j.solmat.2017.01.020.

[106] F. Takele Geldasa, M. Abayneh Kebede, M. Wodajo Shura, F. Gashaw Hone, Experimental and computational study of metal oxide nanoparticles for the photocatalytic degradation of organic pollutants: a review, RSC Advances 13 (2023) 18404–18442. https://doi.org/10.1039/D3RA01505J.

[107] N.Y.Y. Lim, S.L. Chiam, C.P. Leo, C.K. Chang, Recent modification, mechanisms, and performance of zinc oxide-based photocatalysts for sustainable dye degradation, Hybrid Advances 7 (2024) 100318. https://doi.org/10.1016/j.hybadv.2024.100318.

[108] H. Kumari, Sonia, Suman, R. Ranga, S. Chahal, S. Devi, S. Sharma, S. Kumar, P. Kumar, S. Kumar, A. Kumar, R. Parmar, A Review on Photocatalysis Used For Wastewater Treatment: Dye Degradation, Water Air Soil Pollut 234 (2023) 349. https://doi.org/10.1007/s11270-023-06359-9.

[109] S. Patil, A. Ranjan, T. Maitra, A. Sharma, One-Step Fabrication of Microchannels Lined with a Metal Oxide Coating, ACS Appl. Mater. Interfaces 8 (2016) 10494–10498. https://doi.org/10.1021/acsami.6b00413.

[110] K. Shukla, S. Agarwalla, S. Duraiswamy, R.K. Gupta, Recent advances in heterogeneous micro-photoreactors for wastewater treatment application, Chemical Engineering Science 235 (2021) 116511. https://doi.org/10.1016/j.ces.2021.116511.

[111] S. Sohrabi, M.K. Moraveji, D. Iranshahi, A review on the design and development of photocatalyst synthesis and application in microfluidic reactors: challenges and opportunities, Reviews in Chemical Engineering 36 (2020) 687–722. https://doi.org/10.1515/revce-2018-0013.

[112] R. Ameta, M.S. Solanki, S. Benjamin, S.C. Ameta, Photocatalysis, in: Advanced Oxidation Processes for Waste Water Treatment, Elsevier, 2018: pp. 135–175. https://doi.org/10.1016/B978-0-12-810499-6.00006-1.

[113] D. Malwal, P. Gopinath, Fabrication and applications of ceramic nanofibers in water remediation: A review, Critical Reviews in Environmental Science and Technology (2016). https://www.tandfonline.com/doi/abs/10.1080/10643389.2015.1109913 (accessed May 28, 2024).

[114] M.J. Silva, P. Alves, J. Gomes, R.C. Martins, P. Ferreira, Optimization of P25/PDMS supported catalysts preparation for the photocatalytic oxidation of parabens, Journal of Environmental Chemical Engineering 11 (2023) 110610. https://doi.org/10.1016/j.jece.2023.110610.

[115] C. Esen, B. Kumru, Photocatalyst-Incorporated Cross-Linked Porous Polymer Networks, Ind. Eng. Chem. Res. 61 (2022) 10616–10630. https://doi.org/10.1021/acs.iecr.2c01658.

[116] I.M. Sosnin, S. Vlassov, L.M. Dorogin, Application of polydimethylsiloxane in photocatalyst composite materials: A review, Reactive and Functional Polymers 158 (2021) 104781. https://doi.org/10.1016/j.reactfunctpolym.2020.104781.

[117] J.M.K. Ng, I. Gitlin, A.D. Stroock, G.M. Whitesides, Components for integrated poly(dimethylsiloxane) microfluidic systems, Electrophoresis 23 (2002) 3461–3473. https://doi.org/10.1002/1522-2683(200210)23:20%3C3461::AID-ELPS3461%3E3.0.CO;2-8.

[118] G. Pirgholi-Givi, Y. Azizian-Kalandaragh, J. Farazin, Comparison of the photocatalytic activity of perovskite structures: Bismuth, barium, and zinc titanate nanostructures for photodegradation of methylene blue from water, Journal of Photochemistry and Photobiology A: Chemistry 408 (2021) 113104. https://doi.org/10.1016/j.jphotochem.2020.113104.

[119] L. Paramanik, S. Subudhi, K.M. Parida, Visible light active titanate perovskites: An overview on its synthesis, characterization and photocatalytic applications, Materials

Research Bulletin 155 (2022) 111965.
https://doi.org/10.1016/j.materresbull.2022.111965.

[120] R. Kajala, S.S. Tomar, N. Verma, K.D.P. Nigam, Catalytic reduction of in-flow aqueous Cr(VI) using a slurry of activated carbon fiber-supported Ni nanoparticles in a coiled flow inverter, React. Chem. Eng. 7 (2022) 2508–2517.
https://doi.org/10.1039/D2RE00226D.

[121] S. Singh Tomar, N. Verma, K.D.P. Nigam, Adsorptive desulfurization of thiophene using Cu-CNF slurry in a coiled flow inverter with recycling, Chemical Engineering Science 281 (2023) 119172. https://doi.org/10.1016/j.ces.2023.119172.

[122] Y. Kumar, P. Jaiswal, D. Panda, K.D.P. Nigam, K.G. Biswas, A critical review on nanoparticle-assisted mass transfer and kinetic study of biphasic systems in millimeter-sized conduits, Chemical Engineering and Processing - Process Intensification 170 (2022) 108675. https://doi.org/10.1016/j.cep.2021.108675.

[123] S. Singh, S. Perween, A. Ranjan, Enhancing the visible light induced photocatalytic activity in sol-electrospun zinc titanate nanopowders by nitrogen doping, Journal of Physics and Chemistry of Solids 158 (2021) 110221.
https://doi.org/10.1016/j.jpcs.2021.110221.

[124] Y. Yadawa, A. Verma, S.K. Pandey, A. Ranjan, PVP assisted sol-electrospraying, unlike sol electrospinning, yields highly pure rhombohedral zinc titanate particles that reduce 4-nitrophenol under visible light, Journal of Alloys and Compounds 981 (2024) 173618. https://doi.org/10.1016/j.jallcom.2024.173618.

[125] C. Zuo, X. Wang, X. Ding, Z. Zhong, W. Jin, W. Xing, Combining dip-coating and rotate-drying to preparation of PDMS on SiC tubular support with macropore for high pervaporation performance, Journal of Membrane Science 705 (2024) 122908.
https://doi.org/10.1016/j.memsci.2024.122908.

[126] L.S. Wang, M.W. Xiao, X.J. Huang, Y.D. Wu, Synthesis, characterization, and photocatalytic activities of titanate nanotubes surface-decorated by zinc oxide nanoparticles, Journal of Hazardous Materials 161 (2009) 49–54.
https://doi.org/10.1016/j.jhazmat.2008.03.080.

[127] G. Şahin, S. Goktas, Synthesis, characterization, and enhanced photocatalytic activity of chemically derived ZrO2 nanoparticles by operational parameters, Materials Chemistry and Physics 344 (2025) 131185.
https://doi.org/10.1016/j.matchemphys.2025.131185.

[128] E. Aslan, Ö. Emir, F. Arslan, A. Goktas, A. Tumbul, M. Durgun, A. Kilic, M.A. Aktacir, F. Aslan, Improving the optical properties of CuCoMnOx spinel absorber using ZnO nanorod arrays for thermal collector and photocatalytic applications, Ceramics International 50 (2024) 9169–9176.
https://doi.org/10.1016/j.ceramint.2023.12.233.

[129] A. Göktaş, M. Yesilçimen, A. Kilic, S. Göktaş, A. Tumbul, Synergistic Co–Cu dual doping in ZnS thin Films: Unlocking high room-temperature ferromagnetism and UV-activated photocatalytic efficiency for multifunctional applications, Materials Chemistry and Physics 346 (2025) 131399.
https://doi.org/10.1016/j.matchemphys.2025.131399.

[130] A. Goktas, High-quality solution-based Co and Cu co-doped ZnO nanocrystalline thin films: Comparison of the effects of air and argon annealing environments, Journal of

Alloys and Compounds 735 (2018) 2038–2045. https://doi.org/10.1016/j.jallcom.2017.11.391.

[131] G. Sahin, A. Goktas, E. Aslan, A new way to tune photocatalytic activity, surface morphology, and structural/optical parameters of ZrO2 thin films using different Zr sources along with annealing temperature and film thickness, J Sol-Gel Sci Technol 112 (2024) 425–443. https://doi.org/10.1007/s10971-024-06534-2.

[132] A. Tumbul, E. Aslan, A. Göktaş, I.H. Mutlu, F. Arslan, F. Aslan, Chemically derived quinary Cu2Co1–xNaxSnS4 photon absorber material and its photocatalytic application, Appl. Phys. A 130 (2024) 225. https://doi.org/10.1007/s00339-024-07374-1.

[133] R. Abirami, T.S. Senthil, SP. Keerthana, R. Yuvakkumar, G. Ravi, M. Pannipara, A.G. Al-Sehemi, An approach to enhance the photocatalytic activity of ZnTiO3, Ceramics International 47 (2021) 18122–18131. https://doi.org/10.1016/j.ceramint.2021.03.130.

[134] D.C. Montgomery, G.C. Runger, Applied statistics and probability for engineers, 6. ed, Wiley, Hoboken, NJ, 2014.

[135] M.-L. Hsieh, L.-S. Chen, S.-M. Wang, C.-H. Sun, M.-H. Weng, M.-P. Houng, S.-L. Fu, Low-Temperature Sintering of Microwave Dielectrics (Zn,Mg)TiO3, Japanese Journal of Applied Physics 44 (2005) 5045. https://doi.org/10.1143/JJAP.44.5045.

[136] Q. Du, L. Jiang, L. Ma, J. Duan, Z. Zhou, H. Li, Lattice evolution, order transformation, and microwave dielectric properties of the $Zn_{1-x}Li_{2x}TiO_3$ ($0 \leq x \leq 1$) system ceramics, Journal of Advanced Ceramics 13 (2024) 1178–1188. https://doi.org/10.26599/JAC.2024.9220927.

[137] R.S. Dariani, A. Esmaeili, A. Mortezaali, S. Dehghanpour, Photocatalytic reaction and degradation of methylene blue on TiO2 nano-sized particles, Optik 127 (2016) 7143–7154. https://doi.org/10.1016/j.ijleo.2016.04.026.

[138] S. Venkatesan, S. Suresh, J. Arumugam, P. Ramu, N. Pugazhenthiran, R. Jothilakshmi, K.M. Prabu, Sunlight assisted degradation of methylene blue dye by zinc oxide nanoparticles green synthesized using *Vitex negundo* plant leaf extract, Results in Chemistry 7 (2024) 101315. https://doi.org/10.1016/j.rechem.2024.101315.

[139] I. Ali, J.-O. Kim, Continuous-Flow Photocatalytic Degradation of Organics Using Modified TiO2 Nanocomposites, Catalysts 8 (2018) 43. https://doi.org/10.3390/catal8020043.

[140] D. Rattan Paul, R. Sharma, S. P. Nehra, A. Sharma, Effect of calcination temperature, pH and catalyst loading on photodegradation efficiency of urea derived graphitic carbon nitride towards methylene blue dye solution, RSC Advances 9 (2019) 15381–15391. https://doi.org/10.1039/C9RA02201E.

[141] X. Jaramillo-Fierro, S. Gaona, J. Ramón, E. Valarezo, Porous Geopolymer/ZnTiO3/TiO2 Composite for Adsorption and Photocatalytic Degradation of Methylene Blue Dye, Polymers 15 (2023) 2697. https://doi.org/10.3390/polym15122697.

[142] C. Sahoo, B.B. Panda, A.K. Gupta, Design Aspects of a Continuous Flow Photocatalytic Reactor and its Application to Degrade Methylene Blue and Textile Wastewater, ChemistrySelect 7 (2022) e202201179. https://doi.org/10.1002/slct.202201179.

[143] X. Li, J. Xiong, J. Huang, Z. Feng, J. Luo, Novel g-C3N4/h′ZnTiO3-a′TiO2 direct Z-scheme heterojunction with significantly enhanced visible-light photocatalytic activity, Journal of Alloys and Compounds 774 (2019) 768–778. https://doi.org/10.1016/j.jallcom.2018.10.034.

[144] K.M. Reza, A. Kurny, F. Gulshan, Parameters affecting the photocatalytic degradation of dyes using TiO2: a review, Appl Water Sci 7 (2017) 1569–1578. https://doi.org/10.1007/s13201-015-0367-y.

[145] X. Jaramillo-Fierro, G. Cuenca, Enhancing Methylene Blue Removal through Adsorption and Photocatalysis—A Study on the GO/ZnTiO3/TiO2 Composite, International Journal of Molecular Sciences 25 (2024) 4367. https://doi.org/10.3390/ijms25084367.

[146] Q. Wen, Z. Yu, R. Riedel, The fate and role of *in situ* formed carbon in polymer-derived ceramics, Progress in Materials Science 109 (2020) 100623. https://doi.org/10.1016/j.pmatsci.2019.100623.

[147] J. Liu, C. Tian, T. Jiang, E.I. Ricohermoso, Z. Yu, E. Ionescu, L. Molina-Luna, J.P. Hofmann, R. Riedel, Polymer-derived SiOC ceramics: A potential catalyst support controlled by the sintering temperature and carbon content, Journal of the European Ceramic Society 43 (2023) 3191–3200. https://doi.org/10.1016/j.jeurceramsoc.2023.02.045.

[148] D. Erb, K. Lu, Synthesis of SiOC using solvent-modified polymer precursors, Materials Chemistry and Physics 237 (2019) 121844. https://doi.org/10.1016/j.matchemphys.2019.121844.

[149] K. Lu, D. Erb, Polymer derived silicon oxycarbide-based coatings, International Materials Reviews 63 (2018) 139–161. https://doi.org/10.1080/09506608.2017.1322247.

[150] M.B. Ma, H.J. Wang, J.B. Wen, M. Niu, X.Y. Fan, L. Su, Preparation of Amorphous SiOC Ceramic Powders through Precursor Polymer Pyrolysis, Key Engineering Materials 697 (2016) 27–32. https://doi.org/10.4028/www.scientific.net/KEM.697.27.

[151] G.D. Sorarù, L. Kundanati, B. Santhosh, N. Pugno, Influence of free carbon on the Young's modulus and hardness of polymer-derived silicon oxycarbide glasses, J Am Ceram Soc 102 (2019) 907–913. https://doi.org/10.1111/jace.16131.

[152] W. Szymanski, S. Lipa, W. Fortuniak, J. Chojnowski, P. Pospiech, U. Mizerska, S. Slomkowski, A. Nyczyk-Malinowska, M. Hasik, Silicon oxycarbide (SiOC) ceramic microspheres – Structure and mechanical properties by nanoindentation studies, Ceramics International 45 (2019) 11946–11954. https://doi.org/10.1016/j.ceramint.2019.03.085.

[153] K. Wang, M. Günthner, G. Motz, R.K. Bordia, High performance environmental barrier coatings, Part II: Active filler loaded SiOC system for superalloys, Journal of the European Ceramic Society 31 (2011) 3011–3020. https://doi.org/10.1016/j.jeurceramsoc.2011.05.047.

[154] F. Guo, D. Su, Y. Liu, J. Wang, X. Yan, J. Chen, S. Chen, High acid resistant SiOC ceramic membranes for wastewater treatment, Ceramics International 44 (2018) 13444–13448. https://doi.org/10.1016/j.ceramint.2018.04.149.

[155] S. Mukherjee, Z. Ren, G. Singh, Molecular polymer-derived ceramics for applications in electrochemical energy storage devices, J. Phys. D: Appl. Phys. 51 (2018) 463001. https://doi.org/10.1088/1361-6463/aadb18.

[156] E. Szoldatits, J. Essmeister, L. Schachtner, T. Konegger, K. Föttinger, Polymer-derived SiOC as support material for Ni-based catalysts: CO2 methanation performance and effect of support modification with La2O3, Front. Chem. 11 (2023). https://doi.org/10.3389/fchem.2023.1163503.

[157] B. Araldi Silva, L.F. Belchior Ribeiro, S.Y. Gómez González, D. Hotza, R. de Fátima Peralta Muniz Moreira, A. De Noni Junior, SiOC and SiCN-based ceramic supports for catalysts and photocatalysts, Microporous and Mesoporous Materials 327 (2021) 111435. https://doi.org/10.1016/j.micromeso.2021.111435.

[158] M. Hojamberdiev, R.M. Prasad, K. Morita, M.A. Schiavon, R. Riedel, Polymer-derived mesoporous SiOC/ZnO nanocomposite for the purification of water contaminated with organic dyes, Microporous and Mesoporous Materials 151 (2012) 330–338. https://doi.org/10.1016/j.micromeso.2011.10.015.

[159] J. Pan, W. Shen, Y. Zhao, H. Sun, T. Guo, Y. Cheng, N. Zhao, H. Tang, X. Yan, Difunctional hierarchical porous SiOC composites from silicone resin and rice husk for efficient adsorption and as a catalyst support, Colloids and Surfaces A: Physicochemical and Engineering Aspects 584 (2020) 124041. https://doi.org/10.1016/j.colsurfa.2019.124041.

[160] H. Inde, M. Kanezashi, H. Nagasawa, T. Nakaya, T. Tsuru, Tailoring a Thermally Stable Amorphous SiOC Structure for the Separation of Large Molecules: The Effect of Calcination Temperature on SiOC Structures and Gas Permeation Properties, ACS Omega 3 (2018) 6369–6377. https://doi.org/10.1021/acsomega.8b00632.

[161] A. Tamayo, M.A. Mazo, R. Ruiz-Caro, A. Martín-Illana, L.M. Bedoya, M.D. Veiga-Ochoa, J. Rubio, Mesoporous silicon oxycarbide materials for controlled drug delivery systems, Chemical Engineering Journal 280 (2015) 165–174. https://doi.org/10.1016/j.cej.2015.05.111.

[162] A. Khalid, M. Aslam, M.A. Qyyum, A. Faisal, A.L. Khan, F. Ahmed, M. Lee, J. Kim, N. Jang, I.S. Chang, A.A. Bazmi, M. Yasin, Membrane separation processes for dehydration of bioethanol from fermentation broths: Recent developments, challenges, and prospects, Renewable and Sustainable Energy Reviews 105 (2019) 427–443. https://doi.org/10.1016/j.rser.2019.02.002.

[163] H. Zeng, S. He, S.S. Hosseini, B. Zhu, L. Shao, Emerging nanomaterial incorporated membranes for gas separation and pervaporation towards energetic-efficient applications, Advanced Membranes 2 (2022) 100015–100015. https://doi.org/10.1016/J.ADVMEM.2021.100015.

[164] A.E. Farrell, R.J. Plevin, B.T. Turner, A.D. Jones, M. O'Hare, D.M. Kammen, Ethanol can contribute to energy and environmental goals, Science 311 (2006) 506–508. https://doi.org/10.1126/science.1121416.

[165] J. Baeyens, Q. Kang, L. Appels, R. Dewil, Y. Lv, T. Tan, Challenges and opportunities in improving the production of bio-ethanol, Progress in Energy and Combustion Science 47 (2015) 60–88. https://doi.org/10.1016/j.pecs.2014.10.003.

[166] X. He, T. Wang, J. Huang, J. Chen, J. Li, Fabrication and characterization of superhydrophobic PDMS composite membranes for efficient ethanol recovery via

pervaporation, Separation and Purification Technology 241 (2020). https://doi.org/10.1016/j.seppur.2020.116675.

[167] T. Mohammadi, A. Aroujalian, A. Bakhshi, Pervaporation of dilute alcoholic mixtures using PDMS membrane, Chemical Engineering Science 60 (2005) 1875–1880. https://doi.org/10.1016/J.CES.2004.11.039.

[168] X. Fenjuan, C. Yiwei, J. Wanqin, X. Nanping, Polydimethylsiloxane (PDMS)/ceramic composite membrane with high flux for pervaporation of ethanol-water mixtures, Industrial and Engineering Chemistry Research 46 (2007) 2224–2230. https://doi.org/10.1021/IE0610290/ASSET/IMAGES/LARGE/IE0610290F00006.JPEG.

[169] S. Takegami, H. Yamada, S. Tsujii, Pervaporation of ethanol/water mixtures using novel hydrophobic membranes containing polydimethylsiloxane☆, Journal of Membrane Science 75 (1992) 93–105. https://doi.org/10.1016/0376-7388(92)80009-9.

[170] X. Han, L. Wang, J. Li, X. Zhan, J. Chen, J. Yang, Separation of ethanol from ethanol/water mixtures by pervaporation with silicone rubber membranes: Effect of silicone rubbers, Journal of Applied Polymer Science 119 (2011) 3413–3421. https://doi.org/10.1002/app.32991.

[171] H. Zhou, R. Shi, W. Jin, Novel organic–inorganic pervaporation membrane with a superhydrophobic surface for the separation of ethanol from an aqueous solution, Separation and Purification Technology 127 (2014) 61–69. https://doi.org/10.1016/j.seppur.2014.02.032.

[172] S. Manshad, M. Ghazali, M. Nawawi, M.R. Sazegar, H.B. Hassan, A.M. Alamaria, Membranes with Favorable Chemical Materials for Pervaporation Process: A Review, (2016). https://doi.org/10.4172/2155-9589.1000164.

[173] P. Peng, Y. Lan, L. Liang, K. Jia, Membranes for bioethanol production by pervaporation, Biotechnology for Biofuels 2021 14:1 14 (2021) 1–33. https://doi.org/10.1186/S13068-020-01857-Y.

[174] S. Perween, A. Ranjan, Altered phase behavior of the lauric acid–stearic acid binary mixtures in electrospun PVA–PDMS mats, Mater. Adv. 3 (2022) 2737–2748. https://doi.org/10.1039/D1MA01164B.

[175] S. Perween, Z. Khan, S. Singh, A. Ranjan, PVA-PDMS-Stearic acid composite nanofibrous mats with improved mechanical behavior for selective filtering applications, Scientific Reports 8 (2018) 1–14. https://doi.org/10.1038/s41598-018-34440-5.

[176] L. Ji, B. Shi, L. Wang, Pervaporation separation of ethanol/water mixture using modified zeolite filled PDMS membranes, Journal of Applied Polymer Science 132 (2015). https://doi.org/10.1002/APP.41897.

[177] G. Liu, F. Xiangli, W. Wei, S. Liu, W. Jin, Improved performance of PDMS/ceramic composite pervaporation membranes by ZSM-5 homogeneously dispersed in PDMS via a surface graft/coating approach, Chemical Engineering Journal 174 (2011) 495–503. https://doi.org/10.1016/J.CEJ.2011.06.004.

[178] P.-Y. Zheng, X.-Q. Li, J.-K. Wu, N.-X. Wang, J. Li, Q.-F. An, Enhanced butanol selectivity of pervaporation membrane with fluorinated monolayer on

polydimethylsiloxane surface, Journal of Membrane Science 548 (2018) 215–222. https://doi.org/10.1016/j.memsci.2017.11.015.

[179] P. Peng, Y. Lan, A. Xu, M. Liu, Enhanced ethanol pervaporative selectivity of polydimethylsiloxane membranes by incorporating with graphene oxide@silica core-shell structure, Journal of Applied Polymer Science 140 (2023). https://doi.org/10.1002/app.53449.

[180] Y. Lan, N. Yan, W. Wang, Application of PDMS pervaporation membranes filled with tree bark biochar for ethanol/water separation, RSC Advances 6 (2016) 47637–47645. https://doi.org/10.1039/C6RA06794H.

[181] S. Shi, Z. Du, H. Ye, C. Zhang, H. Li, A Novel Carbon Black/Polydimethylsiloxane Composite Membrane with High Flux for the Separation of Ethanol from Water by Pervaporation, Polymer Journal 38 (2006) 949–955. https://doi.org/10.1295/polymj.PJ2005238.

[182] R. Man, X. Deng, Influence of nanoscaled SiO2 particles on the pervaporation performance of PDMS membranes, in: 2012: pp. 916–920. https://doi.org/10.4028/www.scientific.net/AMM.174-177.916.

[183] N.K. Sethy, Z. Arif, P.K. Mishra, P. Kumar, Synthesis of SiO2 nanoparticle from bamboo leaf and its incorporation in PDMS membrane to enhance its separation properties, Journal of Polymer Engineering 39 (2019) 679–687. https://doi.org/10.1515/POLYENG-2019-0120/MACHINEREADABLECITATION/RIS.

[184] S. Patil, A. Ranjan, T. Maitra, A. Sharma, One-Step Fabrication of Microchannels Lined with a Metal Oxide Coating, ACS Applied Materials and Interfaces 8 (2016) 10494–10498. https://doi.org/10.1021/ACSAMI.6B00413/ASSET/IMAGES/LARGE/AM-2016-00413Q_0006.JPEG.

[185] F. Czerwinski, Thermal Stability of Aluminum Alloys, Materials 13 (2020) 3441. https://doi.org/10.3390/ma13153441.

[186] N.E. Grant, S.L. Pain, E. Khorani, R. Jefferies, A. Wratten, S. McNab, D. Walker, Y. Han, R. Beanland, R.S. Bonilla, J.D. Murphy, Activation of Al2O3 surface passivation of silicon: Separating bulk and surface effects, Applied Surface Science 645 (2024) 158786. https://doi.org/10.1016/j.apsusc.2023.158786.

[187] B. Bettens, S. Dekeyzer, B. Van Der Bruggen, J. Degrè, C. Vandecasteele, Transport of Pure Components in Pervaporation through a Microporous Silica Membrane, (2005). https://doi.org/10.1021/jp044515e.

[188] M. Franken, V. Mulder, C.A. Smolders, PERVAPORATION PROCESS USING A THERMAL GRADIENT AS THE DRIVING FORCE*, Journal of Membrane Sctence 53 (1990) 127–141.

[189] Q. Guo, D. Huang, X. Kou, W. Cao, L. Li, L. Ge, J. Li, Synthesis of disperse amorphous SiO2 nanoparticles via sol–gel process, Ceramics International 43 (2017) 192–196. https://doi.org/10.1016/j.ceramint.2016.09.133.

[190] K. Lu, Porous and high surface area silicon oxycarbide-based materials—A review, Materials Science and Engineering: R: Reports 97 (2015) 23–49. https://doi.org/10.1016/J.MSER.2015.09.001.

[191] J. Guo, K. Song, B. Wu, X. Zhu, B. Zhang, Y. Shi, Atomically thin SiC nanoparticles obtained via ultrasonic treatment to realize enhanced catalytic activity for the oxygen reduction reaction in both alkaline and acidic media, RSC Advances 7 (2017) 22875–22881. https://doi.org/10.1039/C7RA01701D.

[192] W. Duan, X. Yin, F. Ye, Q. Li, M. Han, X. Liu, Y. Cai, Synthesis and EMW absorbing properties of nano SiC modified PDC–SiOC, J. Mater. Chem. C 4 (2016) 5962–5969. https://doi.org/10.1039/C6TC01142J.

[193] G.M. Renlund, S. Prochazka, R.H. Doremus, Silicon oxycarbide glasses: Part II. Structure and properties, Journal of Materials Research 6 (1991) 2723–2734. https://doi.org/10.1557/JMR.1991.2723.

[194] D. Li, M.W. Frey, Y.L. Joo, Characterization of nanofibrous membranes with capillary flow porometry, Journal of Membrane Science 286 (2006) 104–114. https://doi.org/10.1016/J.MEMSCI.2006.09.020.

[195] D.K. Mishra, T.T. Saravanan, G.P. Khanra, S. Girikumar, S.C. Sharma, K. Sreekumar, P.P. Sinha, Studies on the processing of nickel base porous wicks for capillary pumped loop for thermal management of spacecrafts, Advanced Powder Technology 21 (2010) 658–662. https://doi.org/10.1016/j.apt.2010.07.011.

[196] A. Jena, K. Gupta, Pore Volume of Nanofiber Nonwovens, International Nonwovens Journal os-14 (2005) 1558925005os–1400204. https://doi.org/10.1177/1558925005os-1400204.

[197] M. Rallini, J.M. Kenny, Nanofillers in Polymers, in: Modification of Polymer Properties, Elsevier Inc., 2017: pp. 47–86. https://doi.org/10.1016/B978-0-323-44353-1.00003-8.

[198] A. Grisolia, G. Dell'Olio, A. Spadafora, M. De Santo, C. Morelli, A. Leggio, L. Pasqua, Hybrid Polymer-Silica Nanostructured Materials for Environmental Remediation, Molecules 28 (2023). https://doi.org/10.3390/MOLECULES28135105.

[199] K. Guerfi, S. Lagerge, M.J. Meziani, Y. Nedellec, G. Chauveteau, Influence of the oxidation on the surface properties of silicon carbide, Thermochimica Acta 434 (2005) 140–149. https://doi.org/10.1016/j.tca.2005.01.038.

[200] H. Zhang, H. Ni, X. Wang, X. Wang, W. Zhang, Effect of chemical groups of polystyrene membrane surface on its pervaporation performance, Journal of Membrane Science 281 (2006) 626–635. https://doi.org/10.1016/j.memsci.2006.04.034.

[201] N. Giovambattista, P.J. Rossky, P.G. Debenedetti, Effect of Temperature on the Structure and Phase Behavior of Water Confined by Hydrophobic, Hydrophilic, and Heterogeneous Surfaces, J. Phys. Chem. B 113 (2009) 13723–13734. https://doi.org/10.1021/jp9018266.

[202] D. Bonn, J. Eggers, J. Indekeu, J. Meunier, E. Rolley, Wetting and spreading, Rev. Mod. Phys. 81 (2009) 739–805. https://doi.org/10.1103/RevModPhys.81.739.

[203] C. Xiao, P. Shi, W. Yan, L. Chen, L. Qian, S.H. Kim, Thickness and Structure of Adsorbed Water Layer and Effects on Adhesion and Friction at Nanoasperity Contact, Colloids and Interfaces 3 (2019) 55. https://doi.org/10.3390/colloids3030055.

[204] O. Icin, D. Zeydanlı, M. Biesuz, G.D. Sorarù, C. Vakifahmetoglu, Porous polymer-derived ceramics for environmental applications: Sorption, filtration, and catalysis, Open Ceramics 23 (2025) 100803. https://doi.org/10.1016/j.oceram.2025.100803.

[205] J. Hietaharju, J. Kangas, J. Tanskanen, Analysis of the permeation behavior of ethanol/water mixtures through a polydimethylsiloxane (PDMS) membrane in pervaporation and vapor permeation conditions, Separation and Purification Technology 227 (2019) 115738. https://doi.org/10.1016/j.seppur.2019.115738.

[206] L.M. Vane, V.V. Namboodiri, T.C. Bowen, Hydrophobic zeolite–silicone rubber mixed matrix membranes for ethanol–water separation: Effect of zeolite and silicone component selection on pervaporation performance, Journal of Membrane Science 308 (2008) 230–241. https://doi.org/10.1016/j.memsci.2007.10.003.

[207] L.M. Vane, V.V. Namboodiri, R.G. Meier, Factors affecting alcohol–water pervaporation performance of hydrophobic zeolite–silicone rubber mixed matrix membranes, Journal of Membrane Science 364 (2010) 102–110. https://doi.org/10.1016/j.memsci.2010.08.006.

[208] P.V. Naik, P.L.H. Verlooy, S. Smet, J.A. Martens, I.F.J. Vankelecom, PDMS mixed matrix membranes filled with novel PSS-2 nanoparticles for ethanol/water separation by pervaporation, RSC Adv. 6 (2016) 78648–78651. https://doi.org/10.1039/C6RA15231G.

[209] Y. Lan, N. Yan, W. Wang, Polydimethylsiloxane (PDMS) Membrane Filled with Biochar Core-shell Particles for Removing Ethanol from Water, BioResources 12 (2017) 6591–6606. https://doi.org/10.15376/biores.12.3.6591-6606.

[210] C. Van Goethem, P.V. Naik, M. Van de Velde, J. Van Durme, A. Verplaetse, I.F.J. Vankelecom, Stability of Filled PDMS Pervaporation Membranes in Bio-Ethanol Recovery from a Real Fermentation Broth, Membranes (Basel) 13 (2023) 863. https://doi.org/10.3390/membranes13110863.

[211] A. Bokhary, M. Leitch, B.Q. Liao, Liquid–liquid extraction technology for resource recovery: Applications, potential, and perspectives, Journal of Water Process Engineering 40 (2021) 101762. https://doi.org/10.1016/j.jwpe.2020.101762.

[212] A. Schmidt, J. Strube, Application and Fundamentals of Liquid–Liquid Extraction Processes: Purification of Biologicals, Botanicals, and Strategic Metals, in: Kirk-Othmer Encyclopedia of Chemical Technology, John Wiley & Sons, Ltd, 2018: pp. 1–52. https://doi.org/10.1002/0471238961.koe00041.

[213] P. Kalaichelvi, M. Perumalsamy, A. Arunagiri, K. Sofiya, Synergistic extraction of acetic acid from its aqueous solution, Journal of the University of Chemical Technology and Metallurgy 42 (2007) 291–294.

[214] I. Vural Gürsel, S.K. Kurt, J. Aalders, Q. Wang, T. Noël, K.D.P. Nigam, N. Kockmann, V. Hessel, Utilization of milli-scale coiled flow inverter in combination with phase separator for continuous flow liquid–liquid extraction processes, Chemical Engineering Journal 283 (2016) 855–868. https://doi.org/10.1016/j.cej.2015.08.028.

[215] J. Bobers, J. Grühn, S. Höving, T. Pyka, N. Kockmann, Two-Phase Flow in a Coiled Flow Inverter: Process Development from Batch to Continuous Flow, Org. Process Res. Dev. 24 (2020) 2094–2104. https://doi.org/10.1021/acs.oprd.0c00152.

[216] O. Abushammala, R. Hreiz, C. Lemaître, É. Favre, Heat and/or mass transfer intensification in helical pipes: Optimal helix geometries and comparison with

alternative enhancement techniques, Chemical Engineering Science 234 (2021) 116452. https://doi.org/10.1016/j.ces.2021.116452.

[217] J. Singh, V. Srivastava, K.D.P. Nigam, Novel Membrane Module for Permeate Flux Augmentation and Process Intensification, Ind. Eng. Chem. Res. 55 (2016) 3861–3870. https://doi.org/10.1021/acs.iecr.5b04865.

[218] S. Vashisth, V. Kumar, K.D.P. Nigam, A Review on the Potential Applications of Curved Geometries in Process Industry, Ind. Eng. Chem. Res. 47 (2008) 3291–3337. https://doi.org/10.1021/ie701760h.

[219] M.R. Gaddem, S. Ookawara, K.D.P. Nigam, S. Yoshikawa, H. Matsumoto, Numerical modeling of segmented flow in coiled flow inverter: Hydrodynamics and mass transfer studies, Chemical Engineering Science 234 (2021) 116400. https://doi.org/10.1016/j.ces.2020.116400.

[220] M. Mridha, K.D.P. Nigam, Coiled flow inverter as an inline mixer, Chemical Engineering Science 63 (2008) 1724–1732. https://doi.org/10.1016/j.ces.2007.10.028.

[221] F. Jiang, K.S. Drese, S. Hardt, M. Küpper, F. Schönfeld, Helical flows and chaotic mixing in curved micro channels, AIChE Journal 50 (2004) 2297–2305. https://doi.org/10.1002/aic.10188.

[222] A. P. Sudarsan, V. M. Ugaz, Fluid mixing in planar spiral microchannels, Lab on a Chip 6 (2006) 74–82. https://doi.org/10.1039/B511524H.

[223] F. Schönfeld, S. Hardt, Simulation of helical flows in microchannels, AIChE Journal 50 (2004) 771–778. https://doi.org/10.1002/aic.10071.

[224] J.G. Kralj, H.R. Sahoo, K.F. Jensen, Integrated continuous microfluidic liquid–liquid extraction, Lab Chip 7 (2007) 256–263. https://doi.org/10.1039/B610888A.

[225] K.G. Biswas, G. Das, S. Ray, J.K. Basu, Mass transfer characteristics of liquid-liquid flow in small diameter conduits, Chemical Engineering Science 122 (2015) 652–661. https://doi.org/10.1016/j.ces.2014.07.029.

[226] M.N. Kashid, D.W. Agar, S. Turek, CFD modelling of mass transfer with and without chemical reaction in the liquid–liquid slug flow microreactor, Chemical Engineering Science 62 (2007) 5102–5109. https://doi.org/10.1016/j.ces.2007.01.068.

[227] Liquid/Liquid Slug Flow Capillary Microreactor - Ufer - 2011 - Chemical Engineering & Technology - Wiley Online Library, (n.d.). https://onlinelibrary.wiley.com/doi/abs/10.1002/ceat.201000334 (accessed September 11, 2025).

[228] P. Mondal, S. Ghosh, G. Das, S. Ray, Phase inversion and mass transfer during liquid–liquid dispersed flow through mini-channel, Chemical Engineering and Processing: Process Intensification 49 (2010) 1051–1057. https://doi.org/10.1016/j.cep.2010.08.006.

[229] K.G. Biswas, G. Das, S. Ray, J.K. Basu, The use of bends for enhanced mass transfer during liquid–liquid flow through milli channels, International Journal of Heat and Mass Transfer 84 (2015) 876–892. https://doi.org/10.1016/j.ijheatmasstransfer.2015.01.085.

[230] J. Saien, M. Mozafarvandi, S. Daliri, M. Norouzi, (Liquid + liquid) equilibria for the ternary (water + acetic acid + toluene) system at different temperatures:

Experimental data and correlation, The Journal of Chemical Thermodynamics 57 (2013) 76–81. https://doi.org/10.1016/j.jct.2012.08.017.

[231] D. Tsaoulidis, P. Angeli, Effect of channel size on mass transfer during liquid–liquid plug flow in small scale extractors, Chemical Engineering Journal 262 (2015) 785–793. https://doi.org/10.1016/j.cej.2014.10.012.

[232] M.N. Kashid, A. Renken, L. Kiwi-Minsker, Gas–liquid and liquid–liquid mass transfer in microstructured reactors, Chemical Engineering Science 66 (2011) 3876–3897. https://doi.org/10.1016/j.ces.2011.05.015.

[233] I. Vural Gürsel, S.K. Kurt, J. Aalders, Q. Wang, T. Noël, K.D.P. Nigam, N. Kockmann, V. Hessel, Utilization of milli-scale coiled flow inverter in combination with phase separator for continuous flow liquid–liquid extraction processes, Chemical Engineering Journal 283 (2016) 855–868. https://doi.org/10.1016/j.cej.2015.08.028.

[234] U. Kumar, D. Panda, K.G. Biswas, Augmented mass transfer in liquid-liquid flow through microchannels of different geometries, Chemical Engineering and Processing - Process Intensification 137 (2019) 72–79. https://doi.org/10.1016/j.cep.2019.02.005.

[235] L. Li, J. Zhang, C. Du, G. Luo, Determination of the Liquid/Liquid Mass Transfer Coefficient for Each Phase in Microchannels, Ind. Eng. Chem. Res. 57 (2018) 9028–9036. https://doi.org/10.1021/acs.iecr.8b01976.

[236] L. Vallese, H. Javadi, B. Badenes, J.F. Urchueguia, G. Lombardo, D. Menegazzo, Z. Ure, S. Cesari, M. Bottarelli, E. Baccega, M. De Carli, A. Lopez, B. Sánchez, L. Mabe, A.A. Aydın, S. Bobbo, L. Fedele, A comprehensive review of thermal energy storage technologies and their applications: Creation of a database, Renewable and Sustainable Energy Reviews 225 (2026) 116133. https://doi.org/10.1016/j.rser.2025.116133.

[237] Q. Du, C. Li, J. Sun, H. Zhang, X. Zhang, C. Liu, D. Wu, J. He, Z. Guo, Efficient preparation of polydimethylsiloxane-based phase change composites by forced network assembly with outstanding thermal management capability, J Polym Res 30 (2023) 158. https://doi.org/10.1007/s10965-023-03553-5.

[238] S. Chavan, R. Rudrapati, S. Manickam, A comprehensive review on current advances of thermal energy storage and its applications, Alexandria Engineering Journal 61 (2022) 5455–5463. https://doi.org/10.1016/j.aej.2021.11.003.

[239] S. Mao, Y. Liu, X. Wu, L. Zhang, J. Chen, T. Zhou, Thermal energy storage performance, application and challenge of phase change materials: a review, Energy Storage and Saving (2025). https://doi.org/10.1016/j.enss.2025.03.001.

[240] Z. Said, A.K. Pandey, A.K. Tiwari, B. Kalidasan, F. Jamil, A.K. Thakur, V.V. Tyagi, A. Sarı, H.M. Ali, Nano-enhanced phase change materials: Fundamentals and applications, Progress in Energy and Combustion Science 104 (2024) 101162. https://doi.org/10.1016/j.pecs.2024.101162.

[241] Z. Zhang, Y. Yuan, N. Zhang, X. Cao, Thermophysical Properties of Some Fatty Acids/Surfactants as Phase Change Slurries for Thermal Energy Storage, J. Chem. Eng. Data 60 (2015) 2495–2501. https://doi.org/10.1021/acs.jced.5b00371.

[242] A. Sarı, Thermal reliability test of some fatty acids as PCMs used for solar thermal latent heat storage applications, Energy Conversion and Management 44 (2003) 2277–2287. https://doi.org/10.1016/S0196-8904(02)00251-0.

[243] M.M. Kenisarin, Thermophysical properties of some organic phase change materials for latent heat storage. A review, Solar Energy 107 (2014) 553–575. https://doi.org/10.1016/j.solener.2014.05.001.

[244] X. Zhang, Q. Lin, H. Luo, S. Luo, Three-dimensional graphitic hierarchical porous carbon/stearic acid composite as shape-stabilized phase change material for thermal energy storage, Applied Energy 260 (2020) 114278. https://doi.org/10.1016/j.apenergy.2019.114278.

[245] S. Lerdkanchanaporn, D. Dollimore, An investigation of the evaporation of stearic acid using a simultaneous TG-DTA unit, Thermochimica Acta 324 (1998) 15–23. https://doi.org/10.1016/S0040-6031(98)00519-X.

[246] A. Das, M.M.H. Apu, A. Akter, M.M.A. Reza, R. Mia, An overview of phase change materials, their production, and applications in textiles, Results in Engineering 25 (2025) 103603. https://doi.org/10.1016/j.rineng.2024.103603.

[247] L. Singh, S. Balakrishnan, J. Johnson William, S. Parveen, P.A. Periasamy, R. Kumar, A. Srivastava, S. Kumar, A.K. Shringi, D. Kumari, A. Singh, F. Yan, Mechanistic Insights in Surface Engineering of Micro-/Nanocomposite Phase Change Materials for Thermal Energy Storage: A Review, Advanced Energy and Sustainability Research n/a (2025) 2500067. https://doi.org/10.1002/aesr.202500067.

[248] T.R. Kar, A.K. Samanta, H.D. Sinnur, M. Kumar, Studies on Effect of Application of Capric Acid and Stearic Acid based Reactive Phase Change Materials (rPCM) with PHAMS Binder on Thermal Comfort of Cotton Khadi Fabric as Thermo-tropic Smart Textiles, Journal of Natural Fibers 19 (2022) 5504–5523. https://doi.org/10.1080/15440478.2021.1880517.

[249] Q. Ye, Y. Han, J. Zhang, W. Zhang, C. Xia, J. Li, Bio-based films with improved water resistance derived from soy protein isolate and stearic acid *via* bioconjugation, Journal of Cleaner Production 214 (2019) 125–131. https://doi.org/10.1016/j.jclepro.2018.12.277.

[250] A. Sari, M. Akcay, M. Soylak, A. Onal, Polymer-stearic acid blends as form-stable phase change material for thermal energy storage, Journal of Scientific and Industrial Research 64 (2005) 991.

[251] R. Wang, Y. Kang, T. Lei, S. Li, Z. Zhou, Y. Xiao, Microcapsules composed of stearic acid core and polyethylene glycol-based shell as a microcapsule phase change material, International Journal of Energy Research 45 (2021) 9677–9684. https://doi.org/10.1002/er.6431.

[252] N.P. Wijanarko, S. Daniarta, P. Kolasiński, A Systematic Review of Biopolymer Phase Change Materials for Thermal Energy Storage: Challenges, Opportunities, and Future Direction, Energies 18 (2025) 4262. https://doi.org/10.3390/en18164262.

[253] S. Wu, T. Yan, Z. Kuai, W. Pan, Thermal conductivity enhancement on phase change materials for thermal energy storage: A review, Energy Storage Materials 25 (2020) 251–295. https://doi.org/10.1016/j.ensm.2019.10.010.

[254] A. Yadav, A. Pandey, M. Samykano, B. Kalidasan, Z. Said, A review of organic phase change materials and their adaptation for thermal energy storage, International Materials Reviews 69 (2024) 380–446. https://doi.org/10.1177/09506608241292406.

[255] Y. Liu, R. Zheng, J. Li, High latent heat phase change materials (PCMs) with low melting temperature for thermal management and storage of electronic devices and

power batteries: Critical review, Renewable and Sustainable Energy Reviews 168 (2022) 112783. https://doi.org/10.1016/j.rser.2022.112783.

[256] R. Bidiyasar, R. Kumar, N. Jakhar, State-of-the-art review of mitigation techniques and performance enhancement methods of phase change materials for thermal energy storage technology, Environ Sci Pollut Res (2025). https://doi.org/10.1007/s11356-025-36189-7.

[257] J. Pereira, R. Souza, J. Oliveira, A. Moita, Phase Change Materials in Residential Buildings: Challenges, Opportunities, and Performance, Materials 18 (2025) 2063. https://doi.org/10.3390/ma18092063.

[258] J. Liu, X. Zhu, J. Dai, K. Yang, S. Wang, X. Liu, Integration of sustainable polymers with phase change materials, Progress in Materials Science 151 (2025) 101447. https://doi.org/10.1016/j.pmatsci.2025.101447.

[259] M. Shekari, G. Naderi, H.A. Khonakdar, Flexible Polymer Foams in Thermal Management Technologies: Recent Advances and Applications, Polymer Engineering & Science n/a (n.d.). https://doi.org/10.1002/pen.70049.

[260] N. Yu, X. Xiao, G. Pan, A stearic acidified-ZnO/methyl polysiloxane/PDMS superhydrophobic coating with good mechanical durability and physical repairability, Journal of Dispersion Science and Technology 40 (2019) 1548–1558. https://doi.org/10.1080/01932691.2018.1484294.

[261] P. Cheng, Z. Tang, Y. Gao, P. Liu, C. Liu, X. Chen, Flexible engineering of advanced phase change materials, iScience 25 (2022). https://doi.org/10.1016/j.isci.2022.104226.

[262] C. Wang, Z. Dai, J. Yang, B. Liu, Y. Gao, D. Wu, Y. Xia, J. Yu, W. Yan, X. Zhang, Development and thermal performance of porous PDMS composites with microencapsulated phase change materials for enhanced thermal insulation, J. Mater. Res. 40 (2025) 1335–1345. https://doi.org/10.1557/s43578-025-01582-y.

[263] R.F.A. Teixeira, O. van den Berg, L.-T.T. Nguyen, K. Fehér, F.E. Du Prez, Microencapsulation of Active Ingredients Using PDMS as Shell Material, Macromolecules 47 (2014) 8231–8237. https://doi.org/10.1021/ma501897j.

[264] R. Gupta, S. Kedia, N. Saurakhiya, A. Sharma, A. Ranjan, Composite nanofibrous sheets of fatty acids and polymers as thermo-regulating enclosures, Solar Energy Materials and Solar Cells 157 (2016) 676–685. https://doi.org/10.1016/j.solmat.2016.07.033.

[265] B. Zalba, J.M. Marín, L.F. Cabeza, H. Mehling, Review on thermal energy storage with phase change: materials, heat transfer analysis and applications, Applied Thermal Engineering 23 (2003) 251–283. https://doi.org/10.1016/S1359-4311(02)00192-8.

[266] A. Sharma, V.V. Tyagi, C.R. Chen, D. Buddhi, Review on thermal energy storage with phase change materials and applications, Renewable and Sustainable Energy Reviews 13 (2009) 318–345. https://doi.org/10.1016/j.rser.2007.10.005.

[267] Y. Shi, M. Hu, Y. Xing, Y. Li, Temperature-dependent thermal and mechanical properties of flexible functional PDMS/paraffin composites, Materials and Design 185 (2020). https://doi.org/10.1016/j.matdes.2019.108219.

[268] A. Sarı, A. Karaipekli, Thermal conductivity and latent heat thermal energy storage characteristics of paraffin/expanded graphite composite as phase change material, Applied Thermal Engineering 27 (2007) 1271–1277. https://doi.org/10.1016/j.applthermaleng.2006.11.004.

[269] Y. Zhang, W. Li, J. Huang, M. Cao, G. Du, Expanded Graphite/Paraffin/Silicone Rubber as High Temperature Form-stabilized Phase Change Materials for Thermal Energy Storage and Thermal Interface Materials, Materials 13 (2020) 894. https://doi.org/10.3390/ma13040894.

[270] S. Ishak, S. Mandal, H.-S. Lee, J.K. Singh, Microencapsulation of stearic acid with SiO2 shell as phase change material for potential energy storage, Sci Rep 10 (2020) 15023. https://doi.org/10.1038/s41598-020-71940-9.

[271] A. Sari, K. Kaygusuz, Thermal energy storage system using stearic acid as a phase change material, Solar Energy 71 (2001) 365–376. https://doi.org/10.1016/S0038-092X(01)00075-5.

[272] S. Harikrishnan, S. Magesh, S. Kalaiselvam, Preparation and thermal energy storage behaviour of stearic acid–TiO2 nanofluids as a phase change material for solar heating systems, Thermochimica Acta 565 (2013) 137–145. https://doi.org/10.1016/j.tca.2013.05.001.

Thesis Outcome and List of Publications

This thesis is based on the following publications and manuscripts:

1. A. Verma, S.K. Pandey, K.D.P. Nigam, A. Ranjan, A transparent silicone tube coiled flow inverter impregnated with plasma treated zinc titanate particles on its inner surface as a novel continuous photocatalytic reactor, Materials Science and Engineering: B 324 (2026) 119031. https://doi.org/10.1016/j.mseb.2025.119031.
   (IF 4.6)

2. A. Verma, Y. Yadawa, G.K. Agrahari, K. Malik, A. Ranjan, Enhanced extraction of ethanol from ethanol-water mixture by pervaporation using PDMS membranes impregnated with the PDMS-derived silicon oxy-carbide particles, Chem Eng Commun (2026) 1–15. https://doi.org/10.1080/00986445.2025.2611392.
   (IF 2.0)

3. Phase change materials incorporated PDMS membrane for thermal energy storage application, Anil Verma and Amit Ranjan. **(To be submitted to journal)**

4. Design and characterization of a PDMS-Based CFI reactor for efficient extraction of acetic acid from ternary mixtures, Anil Verma and Amit Ranjan. **(To be submitted to conference)**

Other publication

Y. Yadawa, **A. Verma**, S.K. Pandey, A. Ranjan, PVP assisted sol-electrospraying, unlike sol electrospinning, yields highly pure rhombohedral zinc titanate particles that reduce 4-nitrophenol under visible light, Journal of Alloys and Compounds 981 (2024) 173618. https://doi.org/10.1016/j.jallcom.2024.173618.
(IF 6.3)

List of Attended International Conferences/Workshops

Conferences

(1) ICSEE-2024

Title of Paper: Enhanced liquid-liquid extraction and mass transfer using a monolithic PDMS Coiled Flow Inverter (CFI) and its impregnation with plasma treated photoactive nanoparticles to assist in dye mitigation out of water

Place: MANIT Bhopal, India

Duration: 23rd to 25th February 2024

(2) CHEMCON-2022

Title of Paper: A Novel Method for Surface Impregnation of PDMS Membrane with SiO_2 Nanoparticles

Place: HBTU, Kanpur, India

Duration: 27th to 30th December 2022

Workshops

1. Participated in the NeW IPR 2021 e-Workshop organized by Innovative Technology Enabling Centre (InTEC), CSIR-IMMT, Bhubaneswar during June 14-19, 2021.

2. Participated in international workshop on Electro-Spinning/Spraying-2021" during April 23-24, 2021, organized by Department of Analytical Chemistry, University of Madras-Guindy Chennai, Department of Nano Science & Technology, Bharathiar University Coimbatore, Division of Tissue Culture, Department of Applied Biology, Sree Chitra Tirunal Institute for Medical Sciences & Technology Thiruvananthapuram, The National Academy of Sciences, India-Kerala Chapter, The Society for Biomaterials & Artificial Organs India-Chennai Chapter, Indian Society of Analytical Scientists-Tamil Nadu Chapter, Society for Tissue Engineering and Regenerative Medicine-Chennai Chapter. Abinnovus Consulting Pvt. Ltd-India, and Palms Connect LLC-USA.

Materials Science and Engineering B 324 (2026) 119031

Contents lists available at ScienceDirect

Materials Science & Engineering B

journal homepage: www.elsevier.com/locate/mseb

A transparent silicone tube coiled flow inverter impregnated with plasma treated zinc titanate particles on its inner surface as a novel continuous photocatalytic reactor

Anil Verma [a], Sujeet Kumar Pandey [a], K.D.P. Nigam [a,b,c], Amit Ranjan [a,*]

[a] Department of Mechanical Engineering, Rajiv Gandhi Institute of Petroleum Technology Jais, 229305, India
[b] Department of Chemical Engineering, Indian Institute of Technology Delhi, Hauz Khan, New Delhi, 110016, India
[c] School of Chemical Engineering, University of Adelaide, North Terrace, South Australia 5005, Australia

ARTICLE INFO

Keywords:
Water treatment
Visible light photocatalysis
Polydimethylsiloxane (PDMS)
Coiled flow inverter (CFI)
Surface impregnation
Plasma treatment

ABSTRACT

This study reports (i) fabrication of a transparent CFI reactor with its inner walls infused with the zinc titanate particles, and (ii) kinetics of continuous photocatalytic degradation of methylene blue (MB) dye in water in this reactor. A silicone tube is folded in the form of coiled flow inverter (CFI), lined with PDMS, and subsequently the PDMS lining is impregnated with the photocatalytic rhombohedral zinc titanate ($ZnTiO_3$) by first swelling the film and then exposing it to the aqueous dispersion of the zinc titanate particles. The dispersion of ZTO particles, which is otherwise not easily dispersible in water, is facilitated by a pre-treatment inside a custom designed plasma chamber. The plasma pre-treatment significantly improves particle dispersion as confirmed by the rheological and DLS/zeta potential measurements, and thereby the incorporation of the particles by the swollen PDMS lining of the CFI. Under visible light illumination, $ZnTiO_3$ nanoparticles immobilized on the inner surface of the CFI catalyze the degradation of MB dye molecules through the generation of reactive oxygen species, leading to the transformation of the dye into non-toxic byproducts. The intricate flow patterns within the CFI facilitate efficient mixing, ensuring enhanced contact between the photocatalyst and the dye molecules. Transparency of the structure helps in achieving the higher degradation rate constant under visible light illumination as compared to dark. Under illumination the rate constant observed in CFI (24.67×10^{-3} min^{-1}) is more than twice of that observed in the straight tube configuration.

1. Introduction

Industrial dyes currently in widespread use are typically non-biodegradable and highly toxic, with the textile sector being a major global water consumer [1] and a significant source of organic and chemical contaminants in wastewater including methylene blue (MB), a low molecular weight cationic aromatic dye [2,3]. Although these compounds play a vital role in various human activities, their presence in the environment poses significant ecological risks. These aromatic dyes' inherent breakdown substances have a tendency to accumulate in living organisms, resulting in harmful health consequences for humans [4]. Wastewater discharged from industries such as textiles, pesticides, pharmaceuticals, food processing, and leather manufacturing often contains high concentrations of dyes, contributing to the contamination of water bodies and leading to adverse environmental consequences, including the suppression of photosynthesis and the contamination of aquatic organisms [5]. The resulting turbidity from these dyes obstructs sunlight penetration, which in turn impairs the photosynthetic processes essential for sustaining aquatic life. Consequently, the removal of dyes from industrial effluents prior to their release into natural water sources is of critical importance. Numerous treatment technologies have been explored for this purpose, including membrane filtration, coagulation-flocculation, ozonation, ion exchange, photocatalysis, biological and chemical oxidation, and adsorption. Adsorption, coagulation, membrane filtration, and sedimentation are common methods for remediating organic pollutants like MB and its breakdown products [6–9]. Although these methods have demonstrated efficiency, they all have a drawback in that they shift the target pollutant from one medium to another without necessarily eliminating it. Visible light induced photocatalysis is particularly regarded as a highly efficient and

* Corresponding author.
E-mail address: aranjan@rgipt.ac.in (A. Ranjan).

https://doi.org/10.1016/j.mseb.2025.119031
Received 14 September 2025; Received in revised form 25 October 2025; Accepted 12 November 2025
Available online 24 November 2025

CHEMICAL ENGINEERING COMMUNICATIONS
https://doi.org/10.1080/00986445.2025.2611392

Taylor & Francis
Taylor & Francis Group

RESEARCH ARTICLE

Enhanced extraction of ethanol from ethanol-water mixture by pervaporation using PDMS membranes impregnated with the PDMS-derived silicon oxy-carbide particles

Anil Verma, Yogendra Yadawa, Gunjan Kumar Agrahari, Karan Malik, and Amit Ranjan

Department of Chemical and Biochemical Engineering, Rajiv Gandhi Institute of Petroleum Technology Jais, Uttar Pradesh, India

ABSTRACT

In this work, we report that extraction of ethanol from the ethanol-water mixture using polydimethylsiloxane (PDMS) membranes is enhanced when the membrane is impregnated by the SiOC particles close to one side. SiOC particles with a high surface area ($192\ m^2g^{-1}$) are prepared by a novel route in which a sponge of PDMS is wrapped inside an aluminum foil and subjected to a heat treatment at 550 °C. A 10% cross-linked and cured PDMS membrane is infused with these particles on one side up to a depth of 100 μm by exposing that side to a suspension of SiOC particles in di-iso-propylamine. Infusion leads to increased surface hydrophilicity on that side and a significantly altered pore size distribution in the membrane. We observed enhanced transport of ethanol as compared to water when infused membranes were used for pervaporation of a fifty-fifty mixture of ethanol water. We propose an explanation that the impregnated particles adsorb water molecules forming a water-rich region inside the membrane, which thereby affords a liquid phase diffusion of ethanol and enhances its transport as compared to neat membranes which offer only solid phase diffusion. SiOC modification increased ethanol–water selectivity by ~150% compared to native PDMS.

KEYWORDS

Composite membrane; interfacial phenomena; PDMS; pervaporation; polymer-derived ceramics (PDC); silicon oxycarbide

Introduction

Polymer-derived ceramics (PDC) is an area that has attracted a surge in research activity over the past 10–15 years (Wen et al. 2020). PDC offers a versatile route for manufacturing ceramic-based components. Silicon-based ceramics are particularly convenient to produce using silicon-based polymers. One such important ceramic product is silicon oxycarbide (SiOC) (Liu et al. 2023; Erb and Lu 2019). SiOC particles are derived from the pyrolysis of polymeric precursors that contain silicon, oxygen, and carbons (Lu and Erb 2018; Ma et al. 2016). This process results in a network structure characterized by Si-O-C bonds, where carbon atoms are incorporated into the silicon dioxide (SiO_2) matrix. One of the distinguishing features of these materials is the presence of carbon in both hetero-bonded form with Si (carbide) and segregated graphitic form with carbon atoms joined by sp^2 bonding. The nanocrystalline graphitic domains are included inside the amorphous Si-O-C matrix. These graphitic carbon domains are believed to improve many properties of the material. The mechanical strength of SiOC is enhanced by the presence of carbon within the SiO_2 matrix, providing a balance between rigidity and toughness that is desirable in many structural applications (Sorarù et al. 2019; Szymanski et al. 2019). Chemical resistance is another notable property of SiOC particles. They exhibit excellent resistance to oxidation and corrosion, which extends their usability in harsh chemical environments (Wang et al. 2011; Guo et al. 2018). This chemical inertness, combined with their thermal stability, makes SiOC materials ideal for use in industries such as catalysis and energy storage (Mukherjee et al. 2018). The high specific surface area of SiOC particles, which can reach several hundred square meters per gram, is particularly beneficial in these fields. Since in

CONTACT Amit Ranjan aranjan@rgipt.ac.in Department of Chemical and Biochemical Engineering, Rajiv Gandhi Institute of Petroleum Technology Jais, Uttar Pradesh 229305, India.